

---

# Practical Scaling Laws: Converting Compute into Performance in a Data-Constrained World

---

Christopher M. Bryant  
Arena Physica  
chris@arenaphysica.com

Hao Liu  
Arena Physica  
hao@arenaphysica.com

## Abstract

The scaling laws guiding modern model training were calibrated for a single regime: data-rich, single-epoch pretraining. The dominant such scaling law form, Chinchilla’s  $L = E + A/N^\alpha + B/D^\beta$ , has three structural limitations outside that regime: it diverges as unique data shrinks instead of saturating at the uninformed baseline; it cannot represent overfitting when capacity exceeds the data; and it conflates total examples seen with unique examples available. We propose a closed-form extension,  $L(N, D, T) = E + (L_0 - E)h/(1 + h)$  with  $h = a/N^\alpha + b/T^\beta + cN^\gamma/D^\delta$ , that decomposes loss into undercapacity, undertraining, and overfitting terms. It saturates between the irreducible loss  $E$  and an uninformed baseline  $L_0$  fixed by the loss type, and reduces to Chinchilla in the data-rich, single-epoch limit. We validate it on four multi-epoch experiments spanning four architecture families (MLPs, ResNets, Fourier neural operators, and transformers) across vision, scientific ML, and language domains, and refit it to five published LLM scaling-law grids. Extrapolating to higher compute and larger unique data than seen at fit time, our form achieves state-of-the-art RMSE on every published LLM grid we evaluate and on most cells of our constructed experiments. Once calibrated, the form admits a cost-aware allocation that recovers Chinchilla’s optimum when data is free and shifts toward smaller corpora and more epochs as data grows expensive.

## 1 Introduction

For most modern ML, training data is expensive. Physics surrogates require running an expensive PDE solver to generate each example [4]; medical-imaging foundation models require expert-labeled data [40]; reinforcement-learning agents pay for every transition [39]; LLM finetuning operates at fractions of pretraining data budgets [49]. Even frontier LLM pretraining, where data has historically been the cheap input relative to compute, is starting to revisit tokens as scraped text runs out [47, 36]. In all of these settings, the practitioner faces the same tradeoff: spend dollars to acquire more unique data, or spend compute to revisit the data already in hand. Reasoning about that tradeoff is what scaling laws are for, but the dominant scaling law was calibrated in a regime where the tradeoff didn’t exist.

Scaling laws fit a parametric model of the loss surface from cheap small-scale runs and use it to predict loss at scales practitioners cannot afford to run. The most-cited instance is the Chinchilla form [26]:

$$L(N, D) = E + \frac{A}{N^\alpha} + \frac{B}{D^\beta}. \quad (1)$$

Variants of this power-law-plus-constant template recur across language modeling [27], vision [1], transfer learning [23], downstream tasks [12, 16], and theoretical models [5, 34, 10], and inherit its structural commitments.

**Three structural failures.** Though Equation (1) and its close relatives have been used to fit training runs across many orders of magnitude in the data-rich, single-epoch regime, these forms lack three crucial properties that prevent them from generalizing beyond this regime:

- **No baseline saturation.** The loss should be bounded above by  $L_0$ , the loss of a model that has not learned anything. Chinchilla has  $L \rightarrow \infty$  as  $D \rightarrow 0$  instead of saturating at  $L_0$ .
- **Overfitting unreachable.** At fixed  $D$ , the form is strictly decreasing in  $N$ , but neural networks with  $N \gg D$  overfit [24, 36]: validation loss can rise with capacity past a point.
- **No compute axis independent of  $(N, D)$ .** The form cannot distinguish between total examples seen  $T$  and unique examples  $D$ , precluding the analysis of multi-epoch training runs.

The paper’s contributions are:

- A single parametric form for  $L(N, D, T)$  on  $\mathbb{R}_{>0}^3$  that addresses these failures by decomposing loss into undercapacity, undertraining, and overfitting terms wrapped in a saturating bound between the irreducible loss  $E$  and an uninformed baseline  $L_0$  (Section 2).
- A set of scaling experiments testing the form across four architecture-domain pairs that span vision, scientific machine learning, and language.
- An empirical demonstration of state-of-the-art extrapolation capabilities across prior published LLM scaling-law datasets.
- A strategy that chooses  $(N^*, D^*, T^*)$  to minimize loss given a budget constraint, while optimally allocating that budget between data acquisition and training compute.

## 2 The extended scaling law

Motivated by the boundary failures of Equation (1), we enumerate a list of limiting behaviors (Table 1) that any form in  $(N, D, T)$  should exhibit when  $N$ ,  $D$ , or  $T$  go to either 0 or  $\infty$ . Rows 1–5 require  $L \rightarrow L_0$  when training collapses and row 6 characterizes optimal behavior.

**Proposed form.** We seek a simple closed-form extension of the Chinchilla functional form that obeys the desired limiting behaviors, decomposes into terms with clear physical meaning, and reduces to Equation (1) in the small- $h$  single-epoch limit. Working from those constraints, we arrive at the following form (full derivations are in Appendix B):

$$L(N, D, T) = E + (L_0 - E) \cdot \frac{h(N, D, T)}{1 + h(N, D, T)}, \quad h = \frac{a}{N^\alpha} + \frac{b}{T^\beta} + c \frac{N^\gamma}{D^\delta}. \quad (2)$$

**Notation.**  $N$  is parameters,  $D$  unique training examples,  $T$  total training examples seen (counted with repetition). The three terms in  $h$  represent *undercapacity* ( $a/N^\alpha$ ), *undertraining* ( $b/T^\beta$ ), and *overfitting* ( $cN^\gamma/D^\delta$ ); the saturating wrapper  $h/(1 + h)$  bounds  $L$  in  $[E, L_0]$ , where  $E$  is the irreducible loss and  $L_0$  is the uninformed baseline loss. When necessary for analysis, compute  $C$  is approximated as  $C \approx kNT$  with architecture-dependent constant  $k$  (though the form makes no assumption about the functional relationship between  $C$ ,  $N$ , and  $T$ ), and  $T/D$  is the number of training epochs. The eight free parameters are  $(E, a, b, c, \alpha, \beta, \gamma, \delta)$ .

**What  $L$  represents.** Throughout,  $L(N, D, T)$  is the *lowest validation loss seen during training*: the minimum over checkpoints, not the final-checkpoint value. The convention matters in the overfitting regime ( $N \gg D$ ), where validation loss can rise as the model memorizes; we fit to the achievable minimum, which is what a real deployment would early-stop at.

**Scope of a fit.** A single fit of  $L$  is conditional on a fixed architecture family, training-set distribution, and training recipe (optimizer, LR schedule, regularization, batch size, hyperparameter-selection protocol). These choices reshape the loss surface and are absorbed into the fitted constants.

Table 1: Target limiting behaviors for a parametric loss  $L(N, D, T)$ . Rows where Chinchilla (Eq. (1)) fails are marked; our form (Eq. (2)) satisfies all rows.

#	Limit	Expected $L$	Reason	Chinchilla
1	$N \rightarrow 0$ ; $D$ and $T$ finite	$L_0$	No capacity to represent any distribution	<b>fails</b> ( $L \rightarrow \infty$ )
2	$D \rightarrow 0$ ; $N$ and $T$ finite	$L_0$	No training data	<b>fails</b> ( $L \rightarrow \infty$ )
3	$T \rightarrow 0$ ; $N$ and $D$ finite	$L_0$	No training, random initialization	<b>fails</b> ( $T = D$ , so $L \rightarrow \infty$ as $D \rightarrow 0$ )
4	$N \rightarrow \infty$ ; $T$ and $D$ finite	$L_0$	Infinite-capacity model, finite training	<b>fails</b> ( $L \rightarrow E + B/D^\beta$ )
5	$N, T \rightarrow \infty$ ; $D$ finite	$L_0$	Complete overfitting	<b>fails</b> (unreachable, since $T = D$ )
6	$N, D, T \rightarrow \infty$ jointly	$E$	Irreducible loss reachable when no resource bottlenecks	pass

## 2.1 Three decomposed terms

The difficulty  $h$  is a sum of power laws that represent three distinct underperformance phenomena:

$$h(N, D, T) = \underbrace{\frac{a}{N^\alpha}}_{\text{undercapacity}} + \underbrace{\frac{b}{T^\beta}}_{\text{undertraining}} + \underbrace{c \frac{N^\gamma}{D^\delta}}_{\text{overfitting}}. \quad (3)$$

*Undercapacity*  $a/N^\alpha$  is the only term that does not vanish as  $D$  and  $T$  grow without bound. It captures the residual cost of a model with finite capacity, and its exponent  $\alpha$  is the standard Chinchilla capacity exponent. The precise way that  $N$  maps to capacity depends on the model architecture, but within a given architecture, capacity increases monotonically with  $N$ .

*Undertraining*  $b/T^\beta$  decays with the total examples seen  $T$ . In practice,  $T$  is often taken as  $\approx C/(kN)$  with  $k$  architecture-dependent, but the form does not require any strict relationship between  $C$  and  $T$ . Per Chinchilla single-epoch fits,  $\beta$  is the data-axis exponent: at  $T = D$ ,  $b/T^\beta$  collapses to  $b/D^\beta$  and recovers the Chinchilla data term. Outside the single-epoch grid the two mechanisms separate: undertraining decays in  $T$  regardless of whether each gradient step sees a fresh example or a repeat.

*Overfitting*  $cN^\gamma/D^\delta$  depends only on capacity  $N$  and unique-data count  $D$ , not on training duration. The two-exponent shape is more flexible than the symmetric ratio  $(N/D)^\gamma$ : it allows  $D$ -scaling and  $N$ -scaling to be calibrated independently, since they enter generalization through different mechanisms (sample-size variance of the empirical-risk minimizer in  $D$ , and capacity-driven excess representation in  $N$ ), each with its own scaling rate.

At fixed  $D$ , the interplay between the overfitting term  $cN^\gamma/D^\delta$  and undercapacity term  $a/N^\alpha$  produces an interior minimum in  $L(N)$  in the limit as  $T \rightarrow \infty$  (Appendix J), which implies that for a finite data size, there is a model size beyond which the best achievable performance not only saturates, but *degrades*. This U-shape behavior is a structural feature absent from the other parametric forms surveyed in Section 5. We provide additional remarks on the relationship between ‘‘undercapacity’’ and ‘‘overfitting’’ in Appendix E.

## 2.2 The saturating wrapper

The wrapper  $h/(1+h)$  is a monotone bijection from  $[0, \infty)$  to  $[0, 1)$  with two properties we want:

1. *Small- $h$  linearity.* For  $h \ll 1$ ,  $h/(1+h) = h - h^2 + h^3 - \dots$ , so Equation (2) reduces at leading order to  $L \approx E + (L_0 - E)h$ . This is the regime in which Chinchilla was fit, and our form becomes Chinchilla-like there: the  $(L_0 - E)$  prefactor is absorbed into the fitted coefficients of the power-law terms in  $h$ .
2. *Large- $h$  saturation.* For  $h \rightarrow \infty$ ,  $h/(1+h) \rightarrow 1$  and  $L \rightarrow L_0$ . The form cannot exceed the baseline.

Other wrappers satisfy the same endpoints; we compare against the natural alternative  $1 - e^{-h}$  in Appendix D.

## 2.3 The baseline loss $L_0$

$L_0$  is the loss of an *uninformed baseline*: a model that extracts no information from the data. It is determined by the loss type and the output normalization, not fitted to the loss surface. For cross-entropy over  $K$  possible outcomes,  $L_0 = \ln K$  (Appendix A):  $K = V$  for next-token prediction over

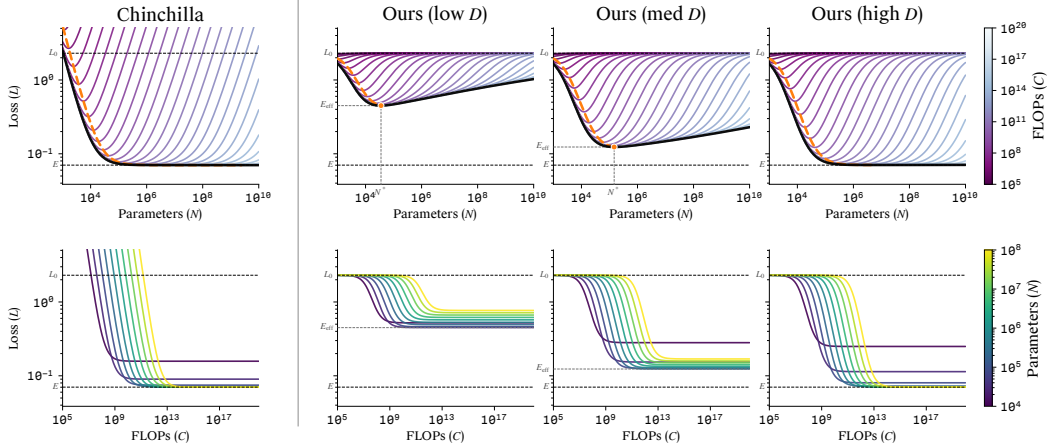


Figure 1: Qualitative shape of our form (right three columns) compared to Chinchilla (left). *Top*: loss vs  $N$  at fixed- $C$  iso-curves; the black curve is the infinite-compute envelope (the  $C \rightarrow \infty$  limit isoFLOP), and the orange dashed curve is the compute-optimal envelope (the locus of isoFLOP minima). *Bottom*: loss vs  $C$  at fixed  $N$ . Chinchilla is unbounded above and admits no overfitting behavior. Our form saturates at the uninformed baseline  $L_0$ , has an interior minimum at  $N^*$  where overfitting meets undercapacity (the floor  $E_{\text{eff}} > E$ ), and recovers Chinchilla’s compute-optimal envelope as  $D$  grows; the floor  $E_{\text{eff}}$  walks toward  $E$  as  $D$  increases.

a vocabulary of size  $V$ , and  $K$  is the number of classes for classification. For relative- $L_2$  regression on  $z$ -normalized targets,  $L_0 = 1$  exactly, since zero predictions give  $\|0 - u\|_2 / \|u\|_2 = 1$ . For other bounded losses,  $L_0$  is the corresponding uninformed-baseline limit. We use  $L_0$  as a structural upper bound on the loss surface; per-dataset values are listed in Section 3.1.

## 2.4 Qualitative behavior

To gain intuition for the form, in Figure 1, we contrast our loss surface with Chinchilla’s. At a low, medium, and high value of  $D$ , we plot two complementary views: isoFLOP curves  $L(N | C)$  at fixed compute, and training trajectories  $L(C | N)$  at fixed model size.

*IsoFLOP curves  $L(N | C)$ .* Chinchilla’s isoFLOPs are U-shaped: they diverge to infinity on both tails and bottom out at a single minimum that defines the compute-optimal model size for that budget. As  $C$  grows, this minimum shifts rightward toward larger model sizes and its loss approaches the irreducible floor  $E$ . Our form’s isoFLOPs share that U-shape near the optimum, but differ at both extremes. The tails of our isoFLOPs saturate above at  $L_0$  and for any finite  $D$ , they approach a different minimum loss value  $E_{\text{eff}} > E$  at a critical model size  $N^*$ . Beyond that model size, the best achievable loss increases, even with infinite compute. As  $D$  grows,  $N^*$  shifts rightward and  $E_{\text{eff}}$  descends toward  $E$ . In the infinite-data-and-compute limit away from  $L_0$ , the envelope of our isoFLOPs coincides with Chinchilla’s.

*Training trajectories  $L(C | N)$ .* By holding  $N$  fixed instead, we can watch the loss evolve as compute increases. Chinchilla’s trajectories begin at infinity and decay monotonically: smaller models drop faster early on but settle at higher plateaus than larger ones. Ours instead begin at the finite ceiling  $L_0$  and likewise decay to an asymptote, but as  $N$  grows, that asymptote first falls, reaching its minimum  $E_{\text{eff}}$  at  $N = N^*$ , then rises again.

## 3 Experiments

We empirically validate our proposed form by comparing it to prior forms across a variety of different calibration sets of  $(N, D, T)$  points. We evaluate extrapolation performance on held-out high- $C$  or high- $D$  runs since extrapolation to these unseen regimes is the primary practical use of a scaling law. Our validation consists of two distinct sets of experiments:

**Multi-domain, multi-epoch experiments (Appendix H).** First, we train four different families of model architectures in four different domains and control the full  $(N, D, T)$  sweep, spanning a regime and design space largely unexplored by prior scaling-law work: *MLPs on MNIST* (10-way image classification: a toy problem where every limiting behavior is cheap to access; Figure 2), *PreActResNets [20] on CIFAR-100* (100-way image classification), *Fourier Neural Operators on PDEBench 2D Darcy flow [31, 45]* (physical PDE simulation), and *decoder-only transformers on TinyStories [15]* (next-token prediction). In each of these domains, we fit our proposed form to the loss surface to evaluate the quality of the fit and the extrapolation error of the form, demonstrating its broad applicability. Full experimental details are in Appendix H.

**Refits to prior LLM scaling studies (Appendix I).** Second, since the majority of prior scaling-law work focuses on language modeling with transformer architectures [27, 26, 36, 16, 29], we refit our form to five published LLM scaling-law grids, each chosen to probe a qualitatively different regime: *Chinchilla [26]* as the canonical compute-optimal reference; *Muennighoff [36]* for multi-epoch repetition (the only public grid with  $T > D$ ); *Gadre [16]* for the over-trained regime ( $D/N$  up to  $\sim 500$ ); *Porian [41]* as a Kaplan stand-in (Kaplan’s raw data is not public; Porian re-runs Chinchilla-style training under a Kaplan-style LR schedule on RefinedWeb); and *Farseer [29]* as the largest open single-recipe grid at modern scale. Dataset and grid descriptions are in Appendix I.

### 3.1 Setup

**Forms compared.** On each dataset, we evaluate our proposed form (Equation (2)) against five refitted parametric scaling law baselines: *Chinchilla [26]* (the canonical additive  $E + A/N^\alpha + B/D^\beta$  form), *Muennighoff [36]* (extends Chinchilla to multi-epoch via an exponentially-saturating effective-data substitution  $D \rightarrow D'$ ), *M4 [1]* (single-axis implicit form bounding  $L$  in  $[E, L_0]$ ; closest structural analog of our wrapper), *BNSL [12]* ( $4+3k$ -parameter smoothly-broken power-law in a composite scalar; the only baseline able to fit non-monotone  $L(N)$ , via  $k$  empirical breakpoints), and *Farseer [29]* ( $L(N, D)$  form with  $N$ -dependent exponents; reports SOTA extrapolation on  $\sim 1000$ -model grids). Appendix G lists each form’s equation, motivation, and free parameters. We also evaluate four ablations of our form: dropping the saturating wrapper, dropping the overfitting term, swapping  $h/(1+h)$  for  $1-e^{-h}$ , and replacing the two-exponent overfitting term  $cN^\gamma/D^\delta$  with a single-exponent ratio  $c(N/D)^\gamma$ .

**Baseline loss values.** Following the loss-type rule of Section 2, we fix  $L_0$  per dataset:  $\ln 10 \approx 2.30$  for MNIST and  $\ln 100 \approx 4.61$  for CIFAR-100 (classification),  $L_0 = 1$  for Darcy (relative- $L_2$  on  $z$ -normalized targets),  $\ln 2000 \approx 7.60$  for TinyStories (our custom 2K BPE tokenizer trained on the TinyStories corpus), and for the public LLM grids  $\ln 32,000 \approx 10.37$  (Chinchilla, Porian; SentencePiece),  $\ln 50,257 \approx 10.82$  (Muennighoff, Gadre; GPT-NeoX/GPT-2 vocabulary), and  $\ln 65,536 \approx 11.09$  (Farseer).

**Training recipe.** The form’s fitted constants are recipe-dependent (Section 2), so we assume a single training recipe within each experiment family and report exponents and coefficients conditional on that recipe. For three of our four training experiments, following Hägele et al. [17], we adopt a Warmup-Stable-Decay (WSD) schedule with brief cooldown forks at log-spaced compute targets, so a single stable run feeds multiple final-loss measurements at different total-compute budgets. We train our MNIST models with no LR schedule at all, so every step is a valid end state and no cooldown forks are needed. Per-family optimizer, LR, batch size, and warmup choices are in Appendix H. For the five published LLM grids we filter each source down to a single training recipe before fitting; per-grid filter rules are in Appendix I.

**Form fitting.** Each form’s free parameters are fit by minimizing Huber loss on log-residuals with BFGS, with  $L_0$  fixed by the loss type and multistart random initializations to mitigate local optima. 95% marginal CIs and standard deviations come from bootstrap resampling of the training set. Full details in Appendix F.

**Extrapolation protocols.** Both holdouts target  $\sim 10\%$  of rows, constructed *groupwise* on the relevant axis so no axis value is split across folds. *high- $C$  holdout* (predicting expensive runs from cheap ones): groupwise on  $C$ , effectively the largest- $C$  10% of rows since  $C$  is near-continuous. *high- $D$  holdout* (predicting large- $D$  performance from small- $D$  data): groupwise on  $D$ ; since  $D$  is

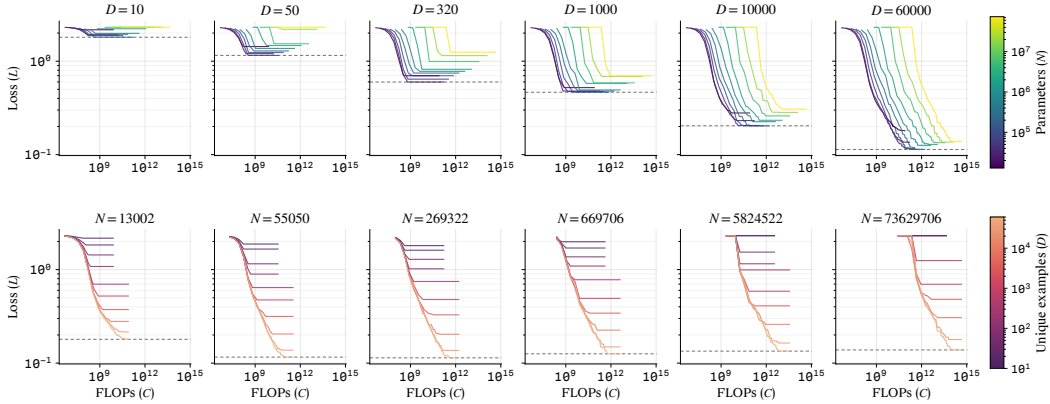


Figure 2: Empirical MNIST running-min validation-loss surface across a selection of  $(N, D, C)$  cells. *Top*: loss vs FLOPs at six fixed unique-data sizes  $D \in \{10, 50, 320, 1000, 10000, 60000\}$ , colored by  $N$ . *Bottom*: the same surface at six fixed  $N$ , colored by  $D$ . The loss floor descends with increasing  $D$  and models exhibit overfitting with increasing  $N$ . For  $D = 60k$ ,  $N^*$  appears around 250k.

highly discrete, the realized holdout is the top- $D$  group for all four of our experiments, often  $>10\%$  of rows.

### 3.2 Results

Figure 2 shows MNIST training run validation loss curves as a function of training FLOPs (averaged across 10 random seeds to reduce noise), split by  $N$  and  $D$ . These curves exhibit the qualitative behavior we anticipate in Section 2.4, consistent with the qualitative shape predicted by the proposed form. Table 2 reports held-out RMSE in log space across all forms under the high- $C$  and high- $D$  protocols defined above. For completeness, we provide an ablation of all parts of our form, as well as random 5-fold cross-validation metrics, in-sample metrics, and mean-bias-error (MBE) equivalents of all RMSE metrics (for systematic bias assessment) in Appendix O.

Table 2: **high- $C$  / high- $D$  extrapolation.** Held-out RMSE (log space) under the high- $C$  and high- $D$  holdout protocols (defined in §3.1). Lower is better. Per column within each pane, **best** and **second best** (point estimate) are highlighted. Error bars: bootstrap  $\pm$  std over 200 resamples.

high- $C$ holdout									
Form $\downarrow$	MNIST	CIFAR-100	Darcy	TinyStories	Chinchilla	Muennighoff	Gadre	Porian	Farseer
Chinchilla [26]	0.332 $\pm$ 0.001	0.156 $\pm$ 0.011	0.322 $\pm$ 0.027	0.173 $\pm$ 0.023	0.024 $\pm$ 0.003	0.092 $\pm$ 0.013	0.038 $\pm$ 0.012	0.100 $\pm$ 0.014	0.028 $\pm$ 0.002
Muennighoff [36]	0.333 $\pm$ 0.001	0.151 $\pm$ 0.008	0.181 $\pm$ 0.009	<b>0.095 <math>\pm</math> 0.012</b>	0.024 $\pm$ 0.003	0.087 $\pm$ 0.008	0.038 $\pm$ 0.012	0.100 $\pm$ 0.015	0.028 $\pm$ 0.001
M4 ( $D$ -axis) [1]	<b>0.295 <math>\pm</math> 0.003</b>	0.126 $\pm$ 0.022	0.404 $\pm$ 0.026	0.337 $\pm$ 0.030	0.067 $\pm$ 0.006	0.094 $\pm$ 0.013	0.119 $\pm$ 0.032	0.114 $\pm$ 0.014	0.111 $\pm$ 0.006
BNSL $k=2$ [12]	0.309 $\pm$ 0.002	<b>0.117 <math>\pm</math> 0.000</b>	0.404 $\pm$ 0.000	0.324 $\pm$ 0.024	0.067 $\pm$ 0.006	0.094 $\pm$ 0.012	0.105 $\pm$ 0.029	37.261 $\pm$ 1.265	0.111 $\pm$ 0.006
Farseer [29]	1.389 $\pm$ 0.010	0.607 $\pm$ 0.025	0.375 $\pm$ 0.071	0.119 $\pm$ 0.009	0.030 $\pm$ 0.002	0.108 $\pm$ 0.013	0.053 $\pm$ 0.009	<b>0.069 <math>\pm</math> 0.013</b>	<b>0.020 <math>\pm</math> 0.002</b>
<b>Ours (Eq. (2))</b>	<b>0.127 <math>\pm</math> 0.001</b>	<b>0.081 <math>\pm</math> 0.010</b>	<b>0.168 <math>\pm</math> 0.016</b>	0.184 $\pm$ 0.021	<b>0.007 <math>\pm</math> 0.004</b>	<b>0.059 <math>\pm</math> 0.011</b>	<b>0.014 <math>\pm</math> 0.011</b>	<b>0.063 <math>\pm</math> 0.012</b>	<b>0.008 <math>\pm</math> 0.001</b>

high- $D$ holdout									
Form $\downarrow$	MNIST	CIFAR-100	Darcy	TinyStories	Chinchilla	Muennighoff	Gadre	Porian	Farseer
Chinchilla [26]	0.123 $\pm$ 0.001	0.182 $\pm$ 0.019	0.388 $\pm$ 0.034	<b>0.057 <math>\pm</math> 0.015</b>	0.028 $\pm$ 0.004	0.112 $\pm$ 0.015	0.038 $\pm$ 0.012	0.115 $\pm$ 0.017	0.017 $\pm$ 0.001
Muennighoff [36]	<b>0.122 <math>\pm</math> 0.005</b>	0.171 $\pm$ 0.031	0.187 $\pm$ 0.013	0.095 $\pm$ 0.008	0.028 $\pm$ 0.004	0.079 $\pm$ 0.010	0.038 $\pm$ 0.012	0.115 $\pm$ 0.017	0.017 $\pm$ 0.001
M4 ( $D$ -axis) [1]	0.192 $\pm$ 0.003	0.265 $\pm$ 0.014	0.361 $\pm$ 0.019	0.223 $\pm$ 0.016	0.036 $\pm$ 0.005	0.101 $\pm$ 0.009	0.119 $\pm$ 0.032	0.079 $\pm$ 0.006	0.070 $\pm$ 0.005
BNSL $k=2$ [12]	0.169 $\pm$ 20.568	0.332 $\pm$ 25.942	66.018 $\pm$ 0.000	69.620 $\pm$ 0.000	0.036 $\pm$ 0.005	0.103 $\pm$ 0.009	0.105 $\pm$ 0.029	0.139 $\pm$ 32.354	0.070 $\pm$ 0.005
Farseer [29]	1.490 $\pm$ 0.016	0.899 $\pm$ 0.152	0.462 $\pm$ 0.054	0.060 $\pm$ 0.026	<b>0.012 <math>\pm</math> 0.002</b>	0.113 $\pm$ 0.023	0.053 $\pm$ 0.009	0.100 $\pm$ 0.011	0.041 $\pm$ 0.002
<b>Ours (Eq. (2))</b>	0.137 $\pm$ 0.004	<b>0.069 <math>\pm</math> 0.016</b>	<b>0.170 <math>\pm</math> 0.014</b>	<b>0.053 <math>\pm</math> 0.014</b>	<b>0.010 <math>\pm</math> 0.005</b>	<b>0.044 <math>\pm</math> 0.012</b>	<b>0.014 <math>\pm</math> 0.011</b>	<b>0.033 <math>\pm</math> 0.003</b>	<b>0.005 <math>\pm</math> 0.000</b>

**Headline.** Our form achieves state-of-the-art held-out RMSE on every published LLM scaling-law grid under both the high- $C$  and high- $D$  holdouts (10 of 10 external-grid columns), averaging 49% lower RMSE than the second-best approach across those entries. Under the same holdouts, our form wins on 6 of the 8 cells in our constructed experiments, underperforming on only high- $C$  TinyStories and high- $D$  MNIST. The TinyStories deficit is driven by an overly optimistic estimate of the irreducible  $E$  when no observations sit near the asymptote, and is remedied by a one-sided

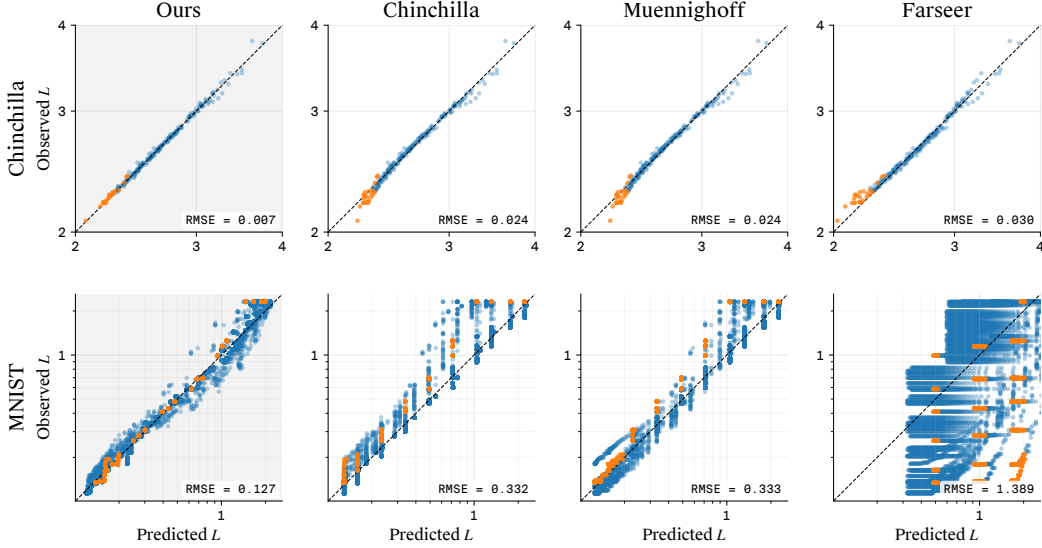


Figure 3: Observed vs. predicted loss for our form (leftmost column) and the three closest competitors, on the data-rich Chinchilla LLM grid (top) and the overfitting-dominated MNIST grid (bottom). Blue: training points; orange: high- $C$  holdout. Our form is tightest in both regimes (RMSE 0.007 vs 0.024 to 0.030 on Chinchilla; 0.127 vs 0.332 to 1.389 on MNIST).

log-space prior on  $E$  that cuts the held-out RMSE by  $4.4\times$  (Appendix L). The MNIST deficit is driven by the cross term  $cN^\gamma/D^\delta$  over-extrapolating from the small- $D$  extreme overfitting regime where it was calibrated into the held-out large- $D$  regime where overfitting is far less pronounced (Appendix M).

**Take-away.** The wins extend beyond the multi-epoch and data-constrained regimes the form was designed for: four of the five published LLM grids (Chinchilla, Gadre, Porian, Farseer) are single-epoch and effectively data-unconstrained, yet the form wins every column. Ablations decompose the gain into two complementary mechanisms (Appendix O); the structural extensions are a strict refinement of Chinchilla, not a tradeoff against fit quality.

### 3.3 Compute footprint

All training ran on AWS Batch with one NVIDIA A10G GPU per job (g5.2xlarge). The campaign consumed  $\sim 206$  GPU-hours total: MNIST  $\sim 46$ , CIFAR-100  $\sim 14$ , Darcy  $\sim 48$ , and TinyStories  $\sim 98$ . Aggregate measured training compute is  $\sim 6.0 \times 10^{18}$  FLOPs, dominated by TinyStories ( $4.8 \times 10^{18}$ ).

## 4 Cost-aware allocation

Beyond fitting held-out loss, a calibrated  $L(N, D, T)$  answers two reciprocal questions of training economics. At unit prices  $\rho_D$  per unique example and  $\rho_C$  per FLOP, with total spend  $\mathcal{B}(N, D, T) = \rho_D D + \rho_C kNT$ : what is the minimum cost required to reach a target loss  $L^*$ , and what is the minimum loss achievable within a fixed budget  $\mathcal{B}_{\max}$ ? Under our form, both  $h$  and  $\mathcal{B}$  are convex in  $(\log N, \log D, \log T)$  (each is a sum of exponentials of affine functions), so both are convex programs with a unique optimum on a single Pareto frontier  $\{(\mathcal{B}^*, L^*)\}$ . The Lagrange first-order condition for the budget-constrained problem is

$$\frac{\partial L / \partial N}{\rho_C k T} = \frac{\partial L / \partial D}{\rho_D} = \frac{\partial L / \partial T}{\rho_C k N}, \quad (4)$$

i.e., at the optimum the marginal loss reduction per dollar is equal across all three axes. The target-loss problem inverts these ratios and shares the same optimal allocation  $(N^*, D^*, T^*)$ . Appendix K gives the full derivation and a numerical recipe.

**Asymptotic regimes.** The dollar-cost ratio  $\eta = \rho_D/\rho_C$  traces a continuum between two limits. When data is free ( $\eta \rightarrow 0$ ), the overfitting term vanishes and  $(N^*, T^*)$  reduces to Chinchilla compute-optimal, with our  $T$ -axis playing the role of Chinchilla’s  $D$ -axis. When data is expensive (each example a simulator run, paid label, or licensed token), the overfitting term binds and the optimum walks toward smaller  $D$ , more epochs, and a smaller  $N^*$ . Prior cost-aware analyses [43, 4, 6] inherit a Chinchilla-style loss with no overfitting term, leaving this data-expensive corner unrepresented.

**Illustrative example.** At fixed total budget, we solve for the minimum-loss allocation on Chinchilla’s fitted exponents  $(\alpha, \beta) = (0.34, 0.28)$  [26] and illustrative overfitting constants  $(c, \gamma, \delta) = (2 \times 10^3, 0.5, 1.0)$  chosen so the overfitting term binds at LLM-scale  $(N, D)$  (Table 3). Increasing  $\eta$  by  $1000\times$  from web-token economics to expert-label economics shrinks  $D^*$  by two orders of magnitude, shrinks  $N^*$  by  $\sim 20\times$ , walks  $T^*/D^*$  from one to  $\sim 1,250$  epochs, and shifts the optimal data-budget share from 12% to 86%. The form converts a single price ratio into a concrete allocation.

Table 3: Cost-optimal allocation (illustrative) at fixed budget  $\mathcal{B}_{\max}$  as the data-to-compute price ratio  $\eta = \rho_D/\rho_C$  grows.

$\eta$	$N^*$	$D^*$	$T^*/D^*$	$L^*$	data \$ share
0 (Chinchilla CO)	$5.2 \times 10^9$	$3.2 \times 10^{11}$	1.0	2.14	0%
$10^{10}$ (web tokens)	$4.4 \times 10^9$	$1.2 \times 10^{11}$	2.7	2.14	12%
$10^{12}$ (licensed corpora)	$1.2 \times 10^9$	$6.3 \times 10^9$	80	2.30	63%
$10^{13}$ (expert / sim)	$2.1 \times 10^8$	$8.6 \times 10^8$	1,250	2.66	86%

## 5 Related work

**Parametric scaling laws and Chinchilla extensions.** Power-law generalization curves [25, 42, 22] were unified into a joint  $L(N, D)$  by Kaplan et al. [27], whose Equation 1.5 implies an overfitting ratio of  $N^{0.74}/D$  structurally close to our  $N^\gamma/D^\delta$  term, but bundled inside a non-separable power so the  $N$ - and  $D$ -axis exponents cannot be fit independently. Hoffmann et al. [26] simplified this to the additive Equation (1) we recover as a small- $h$  limit. Subsequent work refines the protocol around Chinchilla’s form without changing its structural commitments: Gadre et al. [16] reparameterize via the token multiplier  $M = D/N$  for over-trained models, Porian et al. [41] and Pearce and Song [38] re-examine fits under tighter optimization control, Besiroglu et al. [9] flag numerical issues in the original fits, Kumar et al. [28] layer a precision axis, Sardana et al. [43] add an inference-FLOPs term to the cost objective, and Hernandez et al. [23] introduce an effective-data notion under transfer. Li et al. [29] introduce *Farseer*, a 9-parameter  $L(N, D)$  form with  $N$ -dependent exponents reporting large extrapolation-error reductions on  $\sim 1000$  models. None of these forms includes an explicit baseline  $L_0$  or a training-duration axis independent of  $(N, D)$ .

**Saturating and non-monotone forms.** A line of work moves beyond the pure power-law-plus-constant template by introducing saturation. Muennighoff et al. [36] extend Chinchilla to multi-epoch training by replacing  $D$  with an effective-data quantity that saturates exponentially in repetitions (and analogously  $N$  with a saturating capacity quantity); Liew and Kato [32] document related saturation in continual pretraining. This treats  $T$  via a fixed exponential curve in the data axis rather than as an independent power-law axis with its own exponent. Alabdulmohsin et al. [1]’s M4 family instead saturates in the loss axis, bounding  $L$  between  $E$  and  $L_0$  as our wrapper does, but is single-axis (one scalar  $x$  rather than a joint  $h(N, D, T)$ ) and implicit (recovering  $L$  at a given  $x$  requires a nonlinear solve). Caballero et al. [12]’s Broken Neural Scaling Laws (BNSL), a  $4+3k$ -parameter smoothly-broken power-law, can express saturation, inflection, and double descent via empirical breakpoints; standard practice fits BNSL with a composite scalar  $x(N, D, C)$ , yielding a single curve in  $x$  rather than a  $(N, D, T)$  decomposition, and bounding  $L$  in  $[E, L_0]$  only approximately. To our knowledge, the  $N^\gamma/D^\delta$  term wrapped in  $h/(1+h)$  is the first explicit closed-form overfitting term in this literature. Surveys [30, 14] catalog further variants; Appendix G collects the equation, motivation, and parameter count of every form we compare against.

**Theory and other domains.** Theoretical analyses derive scaling exponents from first principles via random-feature, kernel, and dynamical models [34, 5, 10, 11]; these target the undercapacity

and undertraining exponents and predict no overfitting term of our form. Parametric scaling outside language [48, 44, 39, 40] typically reuses or lightly adapts the LLM template and inherits its structural limitations.

## 6 Limitations

**In-distribution validation loss only.** Our scaling law form predicts in-distribution validation loss (loss measured on held-out samples drawn from the same distribution as the training data). Downstream task performance scaling [16], task-level metrics, emergent capabilities, and out-of-distribution behavior are separate layers in the scaling-law stack and out of scope.

**Double descent.** Classical double descent [8, 37] studies what happens *at* the interpolation threshold  $N \approx D$  rather than asymptotically far from it: test error spikes at the threshold and falls again past it, and theoretical results in linear regression and random features [7, 18, 35] characterize when interpolation is benign. Our form is asymptotic and smooth, so it does not predict a peak at  $N \approx D$  and does not attempt to capture this structure. We also do not observe the phenomenon in our experiments, likely because tracking best-so-far validation loss suppresses the model-wise peak [21, 37] and the peak’s typically narrow  $N$  range falls between cells on our log-spaced grids.

**Universality of form, not of fits.** We claim generality of the functional form, not portability of the fitted constants  $(E, a, b, c, \alpha, \beta, \gamma, \delta)$ . Several choices made before fitting are absorbed into these constants and can shift values materially across settings: the parameter-counting convention for  $N$ , architecture family, and the training recipe (optimizer, schedule, regularization). A scaling law that unifies a fitted form across these choices is beyond the scope of this paper. Practitioners refitting our form should hold these choices fixed across the calibration grid and recalibrate per setting.

**Optimistic  $E$  in far compute extrapolation.** The saturating wrapper makes  $E$  identified by the data only when observations approach the asymptote, so far-extrapolation holdouts inherit a pull toward an over-low  $E$  and predictions undershoot. A one-sided log-space prior on  $E$  recovers state-of-the-art performance on the two protocols where this is measurable (Farseer far compute, TinyStories high- $C$ ) without harming fits where the prior isn’t needed (Appendix L); broader applicability across forms and datasets is future work.

**Modeling the low- $D$  regime.** On MNIST high- $D$  our form is the runner-up, behind Muennighoff by  $\sim 12\%$ : the cross term  $cN^\gamma/D^\delta$ , fitted on the heavy-overfitting cells the form was designed to capture, contributes a residual at every other  $D$  that biases extrapolated predictions upward (Appendix M). Practical use can exclude extreme small- $D$  cells from the training set; a structural fix keeping the term well-behaved across the full  $D$  range is future work.

## 7 Conclusion

We introduced a closed-form scaling law  $L(N, D, T) = E + (L_0 - E)h/(1 + h)$  that decomposes loss into undercapacity, undertraining, and overfitting terms, bounded between the irreducible loss  $E$  and an uninformed baseline  $L_0$  fixed by the loss type. The form satisfies six target limiting behaviors, five of which Chinchilla violates, reduces to Chinchilla in the data-rich single-epoch limit, and includes an explicit closed-form overfitting term  $cN^\gamma/D^\delta$  with no analog in prior parametric scaling laws. Across nine calibration grids spanning four architecture families and three domains, it wins 16 of 18 high- $C$  and high- $D$  extrapolation cells, with state-of-the-art held-out RMSE on every published LLM grid.

A calibrated  $L(N, D, T)$  converts a single price ratio  $\eta = \rho_D/\rho_C$  into a concrete cost-optimal allocation  $(N^*, D^*, T^*)$ : the data-free limit recovers Chinchilla compute-optimal, and as data grows expensive (a simulator run, an expert label, a licensed token), the allocation walks toward smaller corpora, more epochs, and smaller models, reaching budget shares prior cost-aware analyses (which inherit Chinchilla’s loss form) cannot describe.

We expect the structural ingredients introduced here (baseline saturation, an independent training-duration axis, and an explicit overfitting term) to inform new parametric scaling laws as practitioners move further into the compute-rich, data-constrained regime that motivates this work.

## References

- [1] Ibrahim M. Alabdulmohsin, Behnam Neyshabur, and Xiaohua Zhai. Revisiting neural scaling laws in language and vision. In *Advances in Neural Information Processing Systems (NeurIPS)*, 2022.
- [2] Anthropic. Claude Code: Anthropic’s agentic coding system. <https://www.anthropic.com/product/claude-code>, 2026.
- [3] Anthropic. Claude Opus 4.7 System Card. <https://www.anthropic.com/claude-opus-4-7-system-card>, April 2026.
- [4] Neil Ashton, Johannes Brandstetter, and Siddhartha Mishra. Fluid intelligence: A forward look on AI foundation models in computational fluid dynamics. *arXiv preprint arXiv:2511.20455*, 2025.
- [5] Yasaman Bahri, Ethan Dyer, Jared Kaplan, Jaehoon Lee, and Utkarsh Sharma. Explaining neural scaling laws. *Proceedings of the National Academy of Sciences*, 121(27), 2024. doi: 10.1073/pnas.2311878121.
- [6] Hritik Bansal, Arian Hosseini, Rishabh Agarwal, Vinh Q. Tran, and Mehran Kazemi. Smaller, weaker, yet better: Training LLM reasoners via compute-optimal sampling. *arXiv preprint arXiv:2408.16737*, 2024.
- [7] Peter L. Bartlett, Philip M. Long, Gábor Lugosi, and Alexander Tsigler. Benign overfitting in linear regression. *Proceedings of the National Academy of Sciences*, 117(48):30063–30070, 2020.
- [8] Mikhail Belkin, Daniel Hsu, Siyuan Ma, and Soumik Mandal. Reconciling modern machine-learning practice and the classical bias-variance trade-off. *Proceedings of the National Academy of Sciences*, 116(32):15849–15854, 2019. doi: 10.1073/pnas.1903070116.
- [9] Tamay Besiroglu, Ege Erdil, Matthew Barnett, and Josh You. Chinchilla scaling: A replication attempt. *arXiv preprint arXiv:2404.10102*, 2024.
- [10] Blake Bordelon, Alexander Atanasov, and Cengiz Pehlevan. A dynamical model of neural scaling laws. In *International Conference on Machine Learning (ICML)*, 2024.
- [11] Ari Brill. Neural scaling laws rooted in the data distribution. *arXiv preprint arXiv:2412.07942*, 2024.
- [12] Ethan Caballero, Kshitij Gupta, Irina Rish, and David Krueger. Broken neural scaling laws. In *International Conference on Learning Representations (ICLR)*, 2023.
- [13] Nicholas Carlini, Daphne Ippolito, Matthew Jagielski, Katherine Lee, Florian Tramèr, and Chiyuan Zhang. Quantifying memorization across neural language models. In *International Conference on Learning Representations (ICLR)*, 2023.
- [14] Leshem Choshen, Yang Zhang, and Jacob Andreas. A hitchhiker’s guide to scaling law estimation. In *International Conference on Machine Learning (ICML)*, 2025.
- [15] Ronen Eldan and Yuanzhi Li. TinyStories: How small can language models be and still speak coherent English? *arXiv preprint arXiv:2305.07759*, 2023.
- [16] Samir Yitzhak Gadre, Georgios Smyrnis, Vaishaal Shankar, Suchin Gururangan, Mitchell Wortsman, Rulin Shao, Jean Mercat, Alex Fang, Jeffrey Li, Sedrick Keh, Rui Xin, Marianna Nezhurina, Igor Vasiljevic, Jenia Jitsev, Luca Soldaini, Alexandros G. Dimakis, Gabriel Ilharco, Pang Wei Koh, Shuran Song, Thomas Kollar, Yair Carmon, Achal Dave, Reinhard Heckel, Niklas Muennighoff, and Ludwig Schmidt. Language models scale reliably with over-training and on downstream tasks. In *International Conference on Learning Representations (ICLR)*, 2025.
- [17] Alexander Hägele, Elie Bakouch, Atli Kosson, Loubna Ben Allal, Leandro Von Werra, and Martin Jaggi. Scaling laws and compute-optimal training beyond fixed training durations. In *Advances in Neural Information Processing Systems (NeurIPS)*, 2024.

- [18] Trevor Hastie, Andrea Montanari, Saharon Rosset, and Ryan J. Tibshirani. Surprises in high-dimensional ridgeless least squares interpolation. *Annals of Statistics*, 50(2):949–986, 2022.
- [19] Kaiming He, Xiangyu Zhang, Shaoqing Ren, and Jian Sun. Deep residual learning for image recognition. In *Conference on Computer Vision and Pattern Recognition (CVPR)*, pages 770–778, 2016.
- [20] Kaiming He, Xiangyu Zhang, Shaoqing Ren, and Jian Sun. Identity mappings in deep residual networks. In *European Conference on Computer Vision (ECCV)*, pages 630–645, 2016.
- [21] Reinhard Heckel and Fatih Furkan Yilmaz. Early stopping in deep networks: Double descent and how to eliminate it. In *International Conference on Learning Representations (ICLR)*, 2021.
- [22] Tom Henighan, Jared Kaplan, Mor Katz, Mark Chen, Christopher Hesse, Jacob Jackson, Heewoo Jun, Tom B. Brown, Prafulla Dhariwal, Scott Gray, Chris Hallacy, Benjamin Mann, Alec Radford, Aditya Ramesh, Nick Ryder, Daniel M. Ziegler, John Schulman, Dario Amodei, and Sam McCandlish. Scaling laws for autoregressive generative modeling. *arXiv preprint arXiv:2010.14701*, 2020.
- [23] Danny Hernandez, Jared Kaplan, Tom Henighan, and Sam McCandlish. Scaling laws for transfer. *arXiv preprint arXiv:2102.01293*, 2021.
- [24] Danny Hernandez, Tom B. Brown, Tom Conerly, Nova DasSarma, Dawn Drain, Sheer El-Showk, Nelson Elhage, Zac Hatfield-Dodds, Tom Henighan, Tristan Hume, Scott Johnston, Ben Mann, Chris Olah, Catherine Olsson, Dario Amodei, Nicholas Joseph, Jared Kaplan, and Sam McCandlish. Scaling laws and interpretability of learning from repeated data. *arXiv preprint arXiv:2205.10487*, 2022.
- [25] Joel Hestness, Sharan Narang, Newsha Ardalani, Gregory Diamos, Heewoo Jun, Hassan Kianinejad, Md. Mostofa Ali Patwary, Yang Yang, and Yanqi Zhou. Deep learning scaling is predictable, empirically. *arXiv preprint arXiv:1712.00409*, 2017.
- [26] Jordan Hoffmann, Sebastian Borgeaud, Arthur Mensch, Elena Buchatskaya, Trevor Cai, Eliza Rutherford, Diego de Las Casas, Lisa Anne Hendricks, Johannes Welbl, Aidan Clark, Tom Hennigan, Eric Noland, Katie Millican, George van den Driessche, Bogdan Damoc, Aurelia Guy, Simon Osindero, Karen Simonyan, Erich Elsen, Jack W. Rae, Oriol Vinyals, and Laurent Sifre. Training compute-optimal large language models. In *Advances in Neural Information Processing Systems (NeurIPS)*, 2022.
- [27] Jared Kaplan, Sam McCandlish, Tom Henighan, Tom B. Brown, Benjamin Chess, Rewon Child, Scott Gray, Alec Radford, Jeffrey Wu, and Dario Amodei. Scaling laws for neural language models. *arXiv preprint arXiv:2001.08361*, 2020.
- [28] Tanishq Kumar, Zachary Ankner, Benjamin F. Spector, Blake Bordelon, Niklas Muennighoff, Mansheej Paul, Cengiz Pehlevan, Christopher Ré, and Aditi Raghunathan. Scaling laws for precision. In *International Conference on Learning Representations (ICLR)*, 2025.
- [29] Houyi Li, Wenzhen Feng, Qiufeng Hu, Zili Zhou, Shuigeng Zhang, Haoyu Xu, Xiangyu Zhang, Jinyang Jiao, Peng Wang, Jing Liu, Xiaolong Jin, Zhi-Hua Ling, Yi Zhang, and Zhiyuan Fan. Farseer: A refined scaling law in large language models. In *Advances in Neural Information Processing Systems (NeurIPS)*, 2025.
- [30] Margaret Li, Sneha Kudugunta, and Luke Zettlemoyer. (Mis)Fitting: A survey of scaling laws. In *International Conference on Learning Representations (ICLR)*, 2025.
- [31] Zongyi Li, Nikola Kovachki, Kamyar Azizzadenesheli, Burigede Liu, Kaushik Bhattacharya, Andrew Stuart, and Anima Anandkumar. Fourier neural operator for parametric partial differential equations. In *International Conference on Learning Representations (ICLR)*, 2021.
- [32] Seng Pei Liew and Takuya Kato. Reusing overtrained language models saturates scaling. *arXiv preprint arXiv:2510.06548*, 2025.

- [33] Haowei Lin, Haotian Ye, Wenzheng Feng, Quzhe Huang, Yujun Li, Hubert Lim, Zhengrui Li, Xiangyu Wang, Jianzhu Ma, Yitao Liang, and James Zou. Can language models discover scaling laws? *arXiv preprint arXiv:2507.21184*, 2025.
- [34] Alexander Maloney, Daniel A. Roberts, and James Sully. A solvable model of neural scaling laws. *arXiv preprint arXiv:2210.16859*, 2022.
- [35] Song Mei and Andrea Montanari. The generalization error of random features regression: Precise asymptotics and the double descent curve. *Communications on Pure and Applied Mathematics*, 75(4):667–766, 2022.
- [36] Niklas Muennighoff, Alexander M. Rush, Boaz Barak, Teven Le Scao, Aleksandra Piktus, Nouamane Tazi, Sampo Pyysalo, Thomas Wolf, and Colin Raffel. Scaling data-constrained language models. In *Advances in Neural Information Processing Systems (NeurIPS)*, 2023.
- [37] Preetum Nakkiran, Gal Kaplun, Yamini Bansal, Tristan Yang, Boaz Barak, and Ilya Sutskever. Deep double descent: Where bigger models and more data hurt. *Journal of Statistical Mechanics: Theory and Experiment*, 2021(12):124003, 2021. doi: 10.1088/1742-5468/ac3a74.
- [38] Tim Pearce and Jinyeop Song. Reconciling Kaplan and Chinchilla scaling laws. *Transactions on Machine Learning Research*, 2024.
- [39] Tim Pearce, Tabish Rashid, Dave Bignell, Raluca Georgescu, Sam Devlin, and Katja Hofmann. Scaling laws for pre-training agents and world models. In *Proceedings of the 42nd International Conference on Machine Learning (ICML)*, 2025.
- [40] Chantal Pellegrini et al. Data scaling laws for radiology foundation models. *arXiv preprint arXiv:2509.12818*, 2025.
- [41] Tomer Porian, Mitchell Wortsman, Jenia Jitsev, Ludwig Schmidt, and Yair Carmon. Resolving discrepancies in compute-optimal scaling of language models. In *Advances in Neural Information Processing Systems (NeurIPS)*, 2024.
- [42] Jonathan S. Rosenfeld, Amir Rosenfeld, Yonatan Belinkov, and Nir Shavit. A constructive prediction of the generalization error across scales. In *International Conference on Learning Representations (ICLR)*, 2020.
- [43] Nikhil Sardana, Jacob Portes, Sasha Doubov, and Jonathan Frankle. Beyond Chinchilla-Optimal: Accounting for inference in language model scaling laws. In *International Conference on Machine Learning (ICML)*, 2024.
- [44] Shashank Subramanian, Peter Harrington, Kurt Keutzer, Wahid Bhimji, Dmitriy Morozov, Michael W. Mahoney, and Amir Gholami. Towards foundation models for scientific machine learning: Characterizing scaling and transfer behavior. In *Advances in Neural Information Processing Systems (NeurIPS)*, 2023.
- [45] Makoto Takamoto, Timothy Praditia, Raphael Leiteritz, Daniel MacKinlay, Francesco Alesiani, Dirk Pflüger, and Mathias Niepert. PDEBench: An extensive benchmark for scientific machine learning. In *Advances in Neural Information Processing Systems (NeurIPS) Datasets and Benchmarks Track*, 2022.
- [46] Kushal Tirumala, Aram H. Markosyan, Luke Zettlemoyer, and Armen Aghajanyan. Memorization without overfitting: Analyzing the training dynamics of large language models. In *Advances in Neural Information Processing Systems (NeurIPS)*, 2022.
- [47] Pablo Villalobos, Anson Ho, Jaime Sevilla, Tamay Besiroglu, Lennart Heim, and Marius Hobbhahn. Position: Will we run out of data? limits of LLM scaling based on human-generated data. In *Proceedings of the 41st International Conference on Machine Learning (ICML)*, 2024.
- [48] Xiaohua Zhai, Alexander Kolesnikov, Neil Houlsby, and Lucas Beyer. Scaling vision transformers. In *Proceedings of the IEEE/CVF Conference on Computer Vision and Pattern Recognition (CVPR)*, 2022.
- [49] Biao Zhang, Zhongtao Liu, Colin Cherry, and Orhan Firat. When scaling meets LLM finetuning: The effect of data, model and finetuning method. In *International Conference on Learning Representations (ICLR)*, 2024.

# Appendix

## Contents

<b>A</b>	<b>The uninformed baseline <math>L_0</math></b>	<b>15</b>
<b>B</b>	<b>Limit verification</b>	<b>15</b>
<b>C</b>	<b>Chinchilla recovery</b>	<b>16</b>
<b>D</b>	<b>Choice of saturating wrapper</b>	<b>17</b>
<b>E</b>	<b>Remarks on capacity and overfitting</b>	<b>17</b>
<b>F</b>	<b>Parameter identification</b>	<b>18</b>
<b>G</b>	<b>Baseline forms</b>	<b>19</b>
<b>H</b>	<b>Our training experiments</b>	<b>20</b>
	H.1 MNIST . . . . .	21
	H.2 CIFAR-100 . . . . .	21
	H.3 Darcy . . . . .	21
	H.4 TinyStories . . . . .	22
<b>I</b>	<b>External refits</b>	<b>22</b>
	I.1 Chinchilla . . . . .	22
	I.2 Muennighoff . . . . .	23
	I.3 Gadre . . . . .	23
	I.4 Porian . . . . .	23
	I.5 Farseer . . . . .	23
<b>J</b>	<b>Compute-optimal model size at fixed unique data</b>	<b>24</b>
<b>K</b>	<b>Cost-optimal allocation</b>	<b>25</b>
<b>L</b>	<b>Far extrapolation: a soft prior on <math>E</math></b>	<b>27</b>
<b>M</b>	<b>MNIST high-<math>D</math>: where the cross term over-extrapolates</b>	<b>30</b>
<b>N</b>	<b>Fitted parameters</b>	<b>31</b>
<b>O</b>	<b>Full experiment results and ablations</b>	<b>32</b>
<b>P</b>	<b>An auto-discovered 12-parameter form</b>	<b>36</b>
<b>Q</b>	<b>Plots</b>	<b>38</b>
	Q.1 Training trajectories . . . . .	38

Q.2 Held-out predictions across datasets . . . . .	41
--	----

## A The uninformed baseline $L_0$

We derive the value  $L_0 = \ln V$  used in Equation (2) as the cross-entropy loss of an *uninformed baseline*: a model that extracts no information from the data and outputs a uniform distribution over the  $V$  possible next tokens (analogously,  $L_0 = \ln K$  for  $K$ -way classification). The derivation makes clear that  $L_0$  is a property of the baseline, not of the data distribution.

**Setup.** Let the data distribution be  $p(x, y)$  over (context, next-token) pairs  $(x, y)$  with  $y \in \{1, \dots, V\}$ . The cross-entropy loss of a model  $q(\cdot | x)$  is

$$L(q) = \mathbb{E}_{(x,y) \sim p} [-\log q(y | x)].$$

**Uninformed baseline.** Define the uninformed baseline  $q_0$  by  $q_0(y | x) = 1/V$  for all  $y$  and all  $x$  (the uniform output is the maximum-entropy distribution given no information about the input). Substituting,

$$L_0 \equiv L(q_0) = \mathbb{E}_{(x,y) \sim p} [-\log(1/V)] = \log V,$$

where the last equality uses that  $-\log(1/V) = \log V$  is a constant and pulls out of the expectation. The result is independent of  $p(x, y)$ : it does not assume tokens are uniformly distributed in the data, nor any structure on the conditional  $p(y | x)$ .

**Classification analog.** For a  $K$ -way classifier with uniform output  $q_0(y | x) = 1/K$ , the same argument gives  $L_0 = \log K$ . Next-token prediction over a vocabulary of size  $V$  is the special case  $K = V$ , with  $L_0 = \log V$ . Per-dataset numerical values are listed in Section 3.1.

**Relative- $L_2$  analog.** For dense regression on  $z$ -normalized targets evaluated under relative- $L_2$  loss ( $L = \|\hat{u} - u\|_2 / \|u\|_2$ , the canonical loss for FNO operator learning [31]), the uninformed baseline is  $\hat{u} \equiv 0$  (the conditional-mean prediction under no information about the input, which is zero on  $z$ -normalized targets), giving  $L_0 = \|0 - u\|_2 / \|u\|_2 = 1$  exactly. This is the value used for the Darcy experiment (Appendix H.3). The same wrapper  $h/(1+h)$  caps the predicted relative- $L_2$  at the uninformed baseline as  $h \rightarrow \infty$ .

**Connection to model initialization.** Row 3 of the limits table (Appendix B) predicts  $L \rightarrow L_0$  as  $T \rightarrow 0$ , the regime where the model has done no training and is at its random initialization. This prediction matches how standard architectures behave at init: a network with logits  $z = (z_1, \dots, z_V)$  outputs softmax probabilities  $q(y | x) = e^{z_y} / \sum_{y'} e^{z_{y'}}$ , and standard initializations (e.g.,  $z_i \sim \mathcal{N}(0, \sigma^2)$  with small  $\sigma$  after the final linear layer) make the components of  $z$  approximately equal in distribution, so  $q(\cdot | x)$  is close to uniform and the empirical first-step loss sits close to  $L_0$ . The same logic generalizes: the wrapper  $h/(1+h)$  enforces  $L \rightarrow L_0$  in every limit where the model fails to extract information from the data ( $N \rightarrow 0$ ,  $D \rightarrow 0$ , or  $T \rightarrow 0$ ), regardless of how the failure is parameterized.

**Scale equivariance.** Because  $L_0$  enters the form as a unit-bearing constant rather than a free parameter, the form is equivariant under uniform rescaling of the loss. If  $L' = kL$  for any constant  $k > 0$ , then  $E' = kE$  and  $L'_0 = kL_0$ , and Equation (2) substitutes consistently:

$$L' = kL = k \left[ E + (L_0 - E) \frac{h}{1+h} \right] = E' + (L'_0 - E') \frac{h}{1+h}.$$

Because  $h$  is dimensionless, the fitted exponents and coefficients ( $a, b, c, \alpha, \beta, \gamma, \delta$ ) are invariant under  $L \rightarrow kL$ . Switching cross-entropy units from nats to bits ( $k = 1/\ln 2$ ), or applying any uniform rescaling to the loss, leaves the calibrated form intact. Loss types without a natural uninformed-baseline ceiling (e.g., MSE on unnormalized targets, where the appropriate  $L_0$  depends on  $\text{Var}(y)$  rather than the loss type alone) need normalization before fitting; the relative- $L_2$  convention above ( $L_0 = 1$ ) is the canonical normalization for dense regression.

## B Limit verification

Restated for convenience, Equation (2) is

$$L(N, D, T) = E + (L_0 - E) \cdot \frac{h(N, D, T)}{1 + h(N, D, T)}, \quad h = \frac{a}{N^\alpha} + \frac{b}{T^\beta} + c \frac{N^\gamma}{D^\delta},$$

with all parameters  $(E, L_0, a, b, c, \alpha, \beta, \gamma, \delta)$  non-negative. The wrapper  $w(h) = h/(1+h)$  maps  $[0, \infty)$  monotonically to  $[0, 1)$ , so  $L$  is automatically bounded in  $[E, L_0]$  for any value of the inputs.

**Rows 1–5** ( $L \rightarrow L_0$ ). The three terms in  $h$  are non-negative, so  $h \rightarrow \infty$  whenever any one term diverges, and the wrapper saturates:  $L \rightarrow L_0$ . Each of the first five rows of Table 1 sends exactly one term to infinity, and the verification reduces to identifying which term:

- Row 1 ( $N \rightarrow 0$ ;  $D, T$  finite):  $a/N^\alpha \rightarrow \infty$ .
- Row 2 ( $D \rightarrow 0$ ;  $N, T$  finite):  $cN^\gamma/D^\delta \rightarrow \infty$  for any  $N > 0$ .
- Row 3 ( $T \rightarrow 0$ ;  $N, D$  finite):  $b/T^\beta \rightarrow \infty$ .
- Row 4 ( $N \rightarrow \infty$ ;  $D, T$  finite):  $cN^\gamma/D^\delta \rightarrow \infty$  since  $D$  is finite.
- Row 5 ( $N, T \rightarrow \infty$ ;  $D$  finite): same as row 4 via the overfitting term, irrespective of  $T$ .

The bound  $L \leq L_0$  is structural (built into the wrapper), so rows 1–5 carry no information beyond confirming that each failure mode is wired into a divergent term in  $h$ .

**Row 6** ( $L \rightarrow E$ ). This is the only row that goes beyond wrapper saturation. It asks for  $h \rightarrow 0$ , which requires *all three* terms in  $h$  to vanish simultaneously. The capacity term  $a/N^\alpha$  vanishes as  $N \rightarrow \infty$  and the undertraining term  $b/T^\beta$  vanishes as  $T \rightarrow \infty$ , but the overfitting term  $cN^\gamma/D^\delta$  vanishes only along paths in which  $D^\delta$  outpaces  $N^\gamma$ . The form therefore satisfies row 6 as a *path-dependent* limit: along any joint path with  $N, T, D \rightarrow \infty$  such that  $N^\gamma/D^\delta \rightarrow 0$ , we have  $h \rightarrow 0$  and  $L \rightarrow E$ . Paths that fail the third condition (e.g.,  $D \propto N$  with  $\gamma > \delta$ ) instead drive  $L \rightarrow L_0$  via the overfitting term. Row 6 thus asserts the existence of a valid path, not pass-anywhere behavior, matching the empirical observation that joint scaling approaches the irreducible loss only when data scales fast enough relative to model size.

## C Chinchilla recovery

**Proposition 1.** *Under three conditions, (i) the single-epoch convention  $T = D$ , (ii) small  $h$  ( $h \leq 0.1$ ), and (iii) negligible overfitting ( $cN^\gamma/D^\delta \ll a/N^\alpha$ ), Equation (2) reduces to Equation (1) up to  $O(h^2)$  corrections, with the same exponents  $(\alpha, \beta)$  and parameter map*

$$A = (L_0 - E)a, \quad B = (L_0 - E)b. \quad (5)$$

**Derivation.** The single-epoch convention  $T = D$  collapses our  $T$  axis onto Chinchilla’s  $D$  axis: the undertraining term reduces to  $b/T^\beta = b/D^\beta$ , and the full  $h$  becomes

$$h = \frac{a}{N^\alpha} + \frac{b}{D^\beta} + c \frac{N^\gamma}{D^\delta}.$$

At Chinchilla-optimal allocations  $N/D \approx 1/20$ . For the overfitting term to be negligible compared to the capacity term, we require

$$c \frac{N^\gamma}{D^\delta} \ll \frac{a}{N^\alpha}, \quad \text{i.e.,} \quad c \ll \frac{a \cdot D^\delta}{N^{\alpha+\gamma}}.$$

With Chinchilla-scale  $N \approx 10^{10}$ ,  $D \approx 2 \times 10^{11}$ ,  $\alpha \approx 0.34$ , and illustrative  $(\gamma, \delta) = (0.5, 1.0)$ , the bound evaluates to  $c \ll \approx 800a$ .

Assuming negligibility and  $h \ll 1$ , Taylor expansion of  $h/(1+h) = h - h^2 + h^3 - \dots$  gives, to leading order,

$$L \approx E + (L_0 - E) \left[ \frac{a}{N^\alpha} + \frac{b}{D^\beta} \right] = E + \frac{(L_0 - E)a}{N^\alpha} + \frac{(L_0 - E)b}{D^\beta}.$$

Comparing to Equation (1) gives the parameter map of Equation (5):  $A = (L_0 - E)a$  and  $B = (L_0 - E)b$ . Because  $T$  enters Equation (2) directly (not via  $C/(kN)$ ), the recovery introduces no architecture-dependent  $k$  factor. The next-order correction is  $-h^2 \cdot (L_0 - E)$ , which at  $h \sim 0.05$  (our illustrative Chinchilla-scale value) is  $\sim 0.02$  nats, smaller than Chinchilla’s reported fitting residuals [26, 41].

**Illustrative constants.** Applying the map with Chinchilla’s fitted constants ( $A \approx 406$ ,  $B \approx 411$ ,  $L_0 - E \approx 9.13$ ) gives  $a \approx 44.5$  and  $b \approx 45.0$ . Existing Chinchilla fits therefore transfer to five of our eight parameters:  $(\alpha, \beta, E)$  are unchanged, and  $(a, b)$  recover from  $(A, B)$  by division by  $(L_0 - E)$ . The remaining  $(c, \gamma, \delta)$  govern the overfitting term, which is empirically small on Chinchilla’s grid: fitting our full 8-parameter form (Appendix I.1) returns  $cN^\gamma/D^\delta \approx 2 \times 10^{-4}$  at  $(N, D) = (10^{10}, 2 \times 10^{11})$ , three orders below the typical  $h \approx 0.25$ . The fit converges and is well-defined, but  $(c, \gamma, \delta)$  come with wide confidence intervals because the overfitting regime is not probed; multi-epoch data is what tightens them (Appendix F). The Chinchilla recovery is a sanity check on the form, not its motivation: any structural form that bounds loss between  $E$  and  $L_0$  and reduces to a useful additive law at small  $h$  would do equally well.

## D Choice of saturating wrapper

The wrapper  $h/(1+h)$  in Equation (2) is one of several monotone bijections from  $[0, \infty)$  to  $[0, 1)$  that satisfy the design constraints in Section 2. The most natural alternative is  $w(h) = 1 - e^{-h}$ , which shares the endpoints  $w(0) = 0$  and  $w(\infty) = 1$ , matches the small- $h$  slope  $w'(0) = 1$  that recovers Chinchilla without rescaling, and introduces no new parameters. Other monotone bijections such as  $\tanh(h)$  or sigmoidal forms either need a free slope or saturation-rate parameter; we exclude them on parsimony grounds.

The two differ in their approach to saturation.  $h/(1+h)$  approaches 1 as  $1 - 1/h + O(1/h^2)$ , while  $1 - e^{-h}$  approaches 1 exponentially. At small  $h$  both expand as  $h - \kappa h^2 + O(h^3)$  with  $\kappa = 1$  for  $h/(1+h)$  and  $\kappa = 1/2$  for  $1 - e^{-h}$ , so the two have essentially the same Chinchilla-scale behavior; the difference becomes visible only in the over-trained or over-overfit corner where  $h \gtrsim 1$ .

We default to  $h/(1+h)$  for closed-form simplicity. Its inverse is rational: writing  $L_{\text{rel}} = (L - E)/(L_0 - E)$ , the inverse wrapper is  $w^{-1}(L_{\text{rel}}) = L_{\text{rel}}/(1 - L_{\text{rel}})$ , used in Equation (12) of Appendix K to map a target loss to the difficulty  $h^*$  that achieves it during cost-allocation analysis. The analogous inverse for  $1 - e^{-h}$  is the transcendental  $-\ln(1 - L_{\text{rel}})$ . The Chinchilla-recovery expansion of Proposition 1 likewise has the clean second-order correction  $-h^2$ , straightforward to bound.

Empirically the two wrappers perform comparably across our four domains and the five published LLM grids: in the “ $1 - e^{-h}$  wrapper” row of the extrapolation tables in Appendix O, the alternative wins some cells (e.g., MNIST high- $D$  RMSE: 0.104 vs. 0.137) and loses others (e.g., CIFAR-100 high- $D$  RMSE: 0.131 vs. 0.069) by comparable margins, with neither wrapper consistently dominant. The default choice is therefore justified on analytical grounds rather than empirical superiority.

## E Remarks on capacity and overfitting

**Population versus sample.** The undercapacity and overfitting terms in  $h$  are not mutually exclusive. They separate two levels of the hypothesis-data hierarchy:  $a/N^\alpha$  measures how well a hypothesis class of size  $N$  can represent the *true population distribution* (a property independent of any particular sample), while  $cN^\gamma/D^\delta$  measures the variance of the empirical-risk minimizer around the population minimizer when only  $D$  samples are available, scaled by the model’s capacity to express deviations. A small model on small data can be both undercapacity (too little capacity to represent the population) and overfit (still enough capacity to memorize the sparse samples, since memorizing  $D$  specific points is an easier hypothesis class than approximating the underlying distribution). In the large- $N/D$  limit the overfitting term grows toward memorization in the strict sense: the model fits the training set exactly while failing to generalize.

**Overfitting at a single epoch.** At  $T = D$  each example has been seen only once, and in classical statistics overfitting requires repeated exposure. In modern deep learning, sufficiently large models memorize even single-epoch training data [13, 46], and the memorization rate scales with model capacity. A plausible mechanism: at large  $N$ , a single gradient step has enough degrees of freedom to encode an example into a subset of weights without perturbing the rest of the model, so excess capacity may flow into example-specific encoding rather than population-level features, with validation loss reflecting the resulting gap. On this reading, the  $cN^\gamma/D^\delta$  term tracks the capacity allocated to training-set-specific encoding. The term itself does not depend on  $T$ , but its contribution to the

predicted loss varies smoothly with  $T$  via the saturating wrapper: at small  $T$  it is masked by the dominant undertraining term  $b/T^\beta$ , and at large  $T$  (where undertraining decays) it becomes the floor that the loss approaches. The transition is gradual and not sharp at  $T = D$ . This same mechanism manifests differently across the training trajectory: Tirumala et al. [46] observe verbatim memorization during the first epoch (well before convergence), while Hernandez et al. [24] and Muennighoff et al. [36] document classical train-val divergence at  $T > D$ . Both observations are consistent with a single capacity-allocation effect, observed under different criteria. Sub-epoch sample-size effects ( $T < D$ ) are dominated by the undertraining term  $b/T^\beta$ , since the relevant cost in that regime is the loss decay with each fresh example seen.

## F Parameter identification

This appendix documents which empirical regimes identify each fitted parameter and the fitting protocol (loss function, optimizer, bootstrap resampling). Term-level interpretability and coefficient-level identifiability are separate questions: the terms of  $h$  have structural meaning regardless of any fit (Section 2), while the individual coefficients within a term are identified only when the fitted grid exercises the relevant regime, and otherwise shift along a coupled manifold with the same total contribution to  $L$ . This appendix concerns the latter. Interpretation of the resulting confidence intervals across our four domains is in Appendix N.

**Free parameters.** Fitting Equation (2) from empirical data requires identifying nine quantities:  $L_0, E, a, b, c, \alpha, \beta, \gamma, \delta$ . Of these,  $L_0$  is fixed by the tokenizer vocabulary (or loss type), reducing the fit to eight free parameters. Each fit is per-(architecture, dataset, recipe) by the scope condition of Section 2; the values are not transferable across fits, and Table 4 accordingly describes which empirical regime within a single fit identifies each parameter.

Table 4: Empirical regime that identifies each parameter of Equation (2) within a single fit.

Parameter	Identifying regime within a fit
$E$	resource-rich asymptote: large $N$ , large $D$ , large $T$ jointly
$a, \alpha$	$N$ -sweep at large $D, T$ (Chinchilla envelope)
$b, \beta$	$T$ -sweep at large $N$ and large $D$ (capacity and overfitting terms suppressed)
$c, \gamma, \delta$	small- $D$ runs at varied $N$ together with multi-epoch runs at varied $T/D$
$L_0$	not fitted: vocabulary size or loss-type ceiling

**Regime decomposition.** The identifying regimes of Table 4 follow from the structure of  $h$ : each of the three terms has a regime where the other two are suppressed, and a sweep in the relevant input traces out the dominant term. The capacity term  $a/N^\alpha$  is the only term that does not vanish as  $D, T \rightarrow \infty$ , so the Chinchilla envelope (large  $D, T$ ) isolates  $a, \alpha$  via an  $N$ -sweep. The undertraining term  $b/T^\beta$  vanishes as  $T \rightarrow \infty$  and is dominated by  $a/N^\alpha$  at small  $N$ ; with  $N$  large (capacity term suppressed) and  $D$  large enough that  $cN^\gamma/D^\delta \ll b/T^\beta$ , a  $T$ -sweep isolates  $b, \beta$ . The overfitting term  $cN^\gamma/D^\delta$  grows as  $D$  shrinks at fixed  $N$  and as  $N$  grows at fixed  $D$ , so small- $D$  runs at varied  $N$  push it into dominance; with  $T$  large enough that  $b/T^\beta$  is small, varying  $D$  at fixed  $N$  pins  $\delta$  and varying  $N$  at fixed  $D$  pins  $\gamma$ , since one slice alone fixes only the linear combination  $c \cdot D^{-\delta}$  or  $c \cdot N^\gamma$ . The asymptote  $L \rightarrow E$  as  $h \rightarrow 0$  pins  $E$  in any resource-rich corner. The saturating wrapper  $h/(1+h)$  does not break this decomposition: it is a strictly monotonic bijection from  $[0, \infty)$  to  $[0, 1)$ , so  $h$  is recoverable from  $L$  as  $h = (L - E)/(L_0 - L)$ , and the in-regime sweeps pin the same parameters they would in the un-wrapped (small- $h$ ) limit. Signal compression near saturation reduces finite-sample signal-to-noise ratio, which bootstrap CIs diagnose as wide marginal intervals.

**Chinchilla-grid sub-regime.** For a fit restricted to a Chinchilla-style grid (single epoch,  $T = D$ , modest  $T/D$ ), the recovery map of Equation (5) identifies  $a, b, \alpha, \beta$  within that fit while  $c, \gamma, \delta$  are unidentified and the form reduces to the small- $h$  Chinchilla limit. Identifying  $c, \gamma, \delta$  requires a grid that additionally exercises the overfitting regime: small- $D$  runs at varied  $N$ , multi-epoch runs at varied  $T/D$ , or both. When the fitted grid lacks these regimes, the marginal CI on  $(c, \gamma, \delta)$  is wide; that width is itself a useful diagnostic: *wide bounds on  $c$  indicate the fit is not yet saturated*, and the practical recommendation is to add runs at higher  $N/D$  or with  $T \gg D$ .

**Loss function.** For each form we minimize Huber loss on log-residuals  $r = \log \hat{L} - \log L$  with transition at  $\tau = 0.05$  nats:  $\ell(r) = \frac{1}{2}r^2$  for  $|r| \leq \tau$  and  $\ell(r) = \tau(|r| - \tau/2)$  otherwise. Huber is robust against the heavy-tailed residuals near saturation cells where small absolute errors translate to large fractional errors in log space, and degenerates to ordinary least-squares in the small-residual limit. The fit recovers the eight free parameters  $(E, a, b, c, \alpha, \beta, \gamma, \delta)$ ;  $L_0$  is fixed by the loss type and not optimized.

**Saturation-cell handling.** Each cell records  $L_{\text{running-min}}$ , the running minimum validation loss across checkpoints, which under softmax-uniform random initialization upper-bounds  $L$  at the step-0 value  $\approx L_0$ . A small number of cells nonetheless sit slightly above  $L_0$ , because the empirical validation-set class distribution is not exactly uniform, so the uniform-class baseline cross-entropy is  $\ln K + \varepsilon$  rather than exactly  $\ln K$ . To prevent such cells from systematically advantaging unbounded forms (which can match  $L > L_0$  exactly) over saturating forms (which are capped at  $L_0$ ), we clip observed  $L$  to  $L_0 - 0.01$  nats before computing the log-residual. Empirically, the clip fires on  $\sim 10\%$  of MNIST cells with max overshoot  $\approx 0.007$  nats and never on CIFAR-100, Darcy, or TinyStories under our checkpoint-tracking protocol; its quantitative effect on fitted parameters is therefore small, but the clip is retained as a safeguard against unbounded-form advantage in saturation regimes.

**Optimizer and restarts.** The Huber objective is minimized with BFGS on a JAX-jitted gradient in a log-reparameterized parameter space (positive parameters in log;  $E$  through softplus to enforce  $E \geq 0$ ). Each fit uses 30 random restarts to mitigate local optima (raised to 200 for forms with non-convex coupled-exponent landscapes such as Farseer) and reports the best-of-restarts solution. For most forms (Chinchilla, Muennighoff, Gadre, BNSL, M4, and ours), each restart independently samples a starting point from a per-parameter distribution:  $E \sim \mathcal{U}(0.5, 3.0)$ , power-law exponents  $\sim \mathcal{U}(0.1, 0.7)$ , multiplicative coefficients log-uniform on  $[0.01, 1000]$  (with break-scale parameters log-uniform on  $[10, 10^6]$  for BNSL). These ranges are heuristic, not derived: they cover the published point estimates of each form with generous margin, but the specific bounds are undocumented authorial choices. Farseer is the exception: its coupled-exponent landscape does not converge reliably from broad random inits, so restarts are centered on the published fitted values from Li et al. [29] Eq. 15 with 30% relative jitter, and the restart count is raised to 200. Restarts that fail to converge are discarded.

**Bootstrap protocol.** Per-parameter marginal CIs come from resampling the training set with replacement 200 times, refitting Equation (2) on each resample (warm-started from the best-of-restarts point estimate to keep the resample fits cheap), and reporting the 2.5% and 97.5% quantiles. The same machinery yields bootstrap CIs on derived quantities: held-out RMSE, mean bias error, and predicted loss at any  $(N, D, T)$  point.

## G Baseline forms

Section 5 surveys prior parametric scaling laws; this appendix gathers them into a single reference. For each form we list its equation (or structural commitment when the equation is implicit), the motivation, and the free parameters. Counts exclude the uninformed baseline  $L_0$  when it is fixed to a known constant (e.g.,  $\ln V$  for next-token prediction); BNSL counts scale with the breakpoint count  $k$ .

**Kaplan Eq. 1.5 [27].**  $L(N, D) = [(N_c/N)^{\alpha_N/\alpha_D} + D_c/D]^{\alpha_D}$ . The first joint  $L(N, D)$  form, derived by combining a power-law fit on each axis. The composite-power structure implies an overfitting ratio of  $N^{0.74}/D$  structurally close to our  $N^\gamma/D^\delta$  term, but bundled inside a non-separable power so the  $N$ - and  $D$ -axis exponents cannot be fit independently. No explicit  $L_0$  ceiling;  $L \rightarrow \infty$  as  $D \rightarrow 0$  or  $N \rightarrow 0$ . 4 free parameters:  $N_c, D_c, \alpha_N, \alpha_D$ .

**Chinchilla [26].**  $L(N, D) = E + A/N^\alpha + B/D^\beta$  (Equation (1)). Replaces Kaplan’s composite power with a strictly additive decomposition and an explicit irreducible-loss floor  $E$ . The canonical compute-optimal reference form, calibrated in the data-rich single-epoch regime; we recover it as the small- $h$  limit of our form (Appendix B). 5 free parameters:  $E, A, B, \alpha, \beta$ .

**Muennighoff [36].**  $L = E + A/(N')^\alpha + B/(D')^\beta$  where  $N'$  and  $D'$  are exponentially-saturating effective quantities: as repetitions  $T/D$  grow,  $D' \rightarrow D \cdot (1 + R_D^*)$  with  $R_D^*$  a fitted saturation scale (and  $N'$  analogously via  $R_N^*$ ). Extends Chinchilla to multi-epoch training by treating each repetition as adding diminishing effective data rather than a fresh example. Multi-epoch behavior in the data axis only; no overfitting term and no independent  $T$  axis. 7 free parameters:  $E, A, B, \alpha, \beta, R_D^*, R_N^*$ .

**M4 [1].** An implicit single-axis form bounding  $L \in [E, L_0]$ , with three free coefficients  $a_{M4}, b_{M4}, c_{M4}$  governing the curvature; recovering  $L$  at a given input scalar  $x \in \{N, D, C\}$  requires a nonlinear solve. The closest structural analog of our wrapper, but single-axis (one scalar  $x$  rather than a joint  $h(N, D, T)$ ), so it cannot decompose loss into separate  $N, D, T$  contributions. 4 free parameters:  $E, a_{M4}, b_{M4}, c_{M4}$ .

**BNSL [12].** A smoothly-broken power law in a composite scalar  $x(N, D, C)$  with  $k$  empirical breakpoints; each breakpoint adds three free parameters (location, slope change, smoothness). The only baseline able to fit non-monotone  $L(N)$ , but the breakpoint locations and shapes are fit, not predicted from  $(N, D)$  structure; bounds  $L$  in  $[E, L_0]$  only approximately. We evaluate  $k = 1$  and  $k = 2$  in our refits.  $4 + 3k$  free parameters: 4 base + 3 per breakpoint.

**Farseer [29].**  $L(N, T) = \exp(a_1 N^{a_2} + a_3) + \exp(b_1 N^{b_2} + b_3) \cdot T^{-\exp(c_1 N^{c_2} + c_3)}$  (Eq. 15 of the paper; their  $D$  axis is total tokens trained on, which corresponds to our  $T$  under their compute-relation convention  $C \approx 6NT$ ). The three exponentials parameterize an  $N$ -dependent irreducible-loss floor, an  $N$ -dependent coefficient on the data term, and an  $N$ -dependent data-axis exponent. Reports state-of-the-art extrapolation on  $\sim 1000$ -model grids. Single-epoch ( $T = D$ ); no overfitting term, no  $L_0$  ceiling. The coupled-exponent structure produces a non-convex landscape that we initialize with paper-anchored restarts (Appendix F). 9 free parameters:  $a_1, a_2, a_3, b_1, b_2, b_3, c_1, c_2, c_3$ .

## H Our training experiments

This appendix documents the four experimental domains we ran ourselves: MNIST, CIFAR-100, Darcy, and TinyStories. Each subsection follows a uniform structure: dataset description, model architecture and grid, and training recipe.

**Conventions shared across domains.** For each run we measure total training FLOPs  $C$  directly with a FLOPs counter; the form takes  $T$  rather than  $C$  and does not depend on the linear approximation  $C \approx kNT$ . The four domains differ in how loss measurements are collected. *MNIST* uses constant LR throughout with no cooldown, so every logged checkpoint is a valid end-state observation: at each checkpoint we record  $(N, D, T_{\text{checkpoint}}, L_{\text{val}}^*)$  with  $L_{\text{val}}^*$  the running minimum validation loss, giving one *trajectory* of points per  $(N, D)$  cell. *CIFAR-100*, *Darcy*, and *TinyStories* use a Warmup-Stable-Decay schedule [17]: each  $(N, D)$  cell consists of one constant-LR stable run that feeds multiple cooldown forks at log-spaced  $T_{\text{total}}$  targets, and we record  $(N, D, T_{\text{total}}, L_{\text{final}})$  once per cooldown. Hägele et al. [17] show that constant LR plus a short late cooldown matches cosine performance and lets a single stable run feed multiple cooldown forks at different total-compute budgets. Stable-phase intermediate checkpoints from these three domains are not used as data points, because the cooldown’s downstream effect makes the intermediate  $L_{\text{val}}^*$  inequivalent to a final-loss observation at the same  $T$ ; MNIST’s no-cooldown protocol makes intermediate-checkpoint and end-of-training observations equivalent by construction, which is why trajectory points are valid there but not elsewhere. We run a single seed per  $(N, D)$  stable run for CIFAR-100, Darcy, and TinyStories, and 10 seeds per cell for MNIST (per-cell losses averaged before fitting), following standard practice in the scaling-law literature [27, 26, 36, 17]; the bootstrap procedure in Appendix F resamples  $(N, D, T; L)$  training-set points to produce confidence intervals on the fitted parameters.

**Effective unique-data exposure.** For trace points or cooldown forks where  $T < D_{\text{budget}}$ , the model has only been exposed to at most  $T$  unique training points regardless of how many were prepared in the corpus. We cap  $D = \min(D_{\text{budget}}, T)$  before fitting so that the form’s overfitting term  $c N^\gamma / D^\delta$  is fed the actually-seen sample count, not the budgeted one; without this cap, the form would treat sub-1-epoch rows as if the model had full access to the prepared corpus, mis-attributing the high observed loss to undertraining alone instead of also to limited data exposure. The cap is engaged on  $\sim 6\%$  of MNIST trace rows (earliest checkpoints on large- $D$  cells, where  $T_{\text{checkpoint}}$  has not yet

reached  $D_{\text{budget}}$ ) and  $\sim 17\%$  of TinyStories cooldown forks (smallest- $T_{\text{total}}$  forks on large- $D$  cells); CIFAR-100 and Darcy have no sub-1-epoch rows by construction, so the cap is a no-op there.

## H.1 MNIST

**Description.** MNIST 10-way digit classification. The grid covers all four probing regimes (undercapacity, compute-optimal, overfitting, and random initialization); with  $L_0 = \ln 10 \approx 2.30$  nats setting an unambiguous saturation ceiling and a cheap constant-LR sweep that produces a continuous  $L(N, D, T)$  trajectory, every limiting behavior of the form is accessible at modest compute.

**Architecture and grid.** 2-hidden-layer ReLU MLP, widths  $w \in \{16, 32, 64, 128, 256, 512, 1024, 2048, 4096, 8192\}$ , giving  $N \in \{13\text{K}, 26\text{K}, 55\text{K}, 118\text{K}, 269\text{K}, 669\text{K}, 1.9\text{M}, 5.8\text{M}, 20\text{M}, 74\text{M}\}$  params (since  $N = 784w + w^2 + 10w$ ). Unique-data sweep  $D \in \{10, 20, 50, 100, 320, 1000, 3160, 10000, 31600, 60000\}$  training images (10 log-spaced values from 10 to 60 000). Validation loss measured on the standard 10,000-image test set.

**Training recipe.** Adam ( $\beta_1 = 0.9, \beta_2 = 0.999$ ) with constant LR  $3 \times 10^{-3}$  from step 0, no warmup, no weight decay, batch size 64. Per-cell  $T_{\text{max}}$  is  $10^5$  samples for  $D \leq 100$  and  $10^6$  samples for  $D > 100$ , giving  $\sim 17$  epochs at the largest cell ( $D = 60,000, T_{\text{max}} = 10^6$ ) up to  $\sim 10,000$  epochs at the smallest ( $D = 10, T_{\text{max}} = 10^5$ ); the trace-point convention then samples  $\sim 100$  log-uniform checkpoints between step 0 and  $T_{\text{max}}$ /batch per cell. No cooldown forks: under the constant-LR protocol every logged checkpoint is a valid end-state observation, and the per- $(N, D)$  trajectory is collected directly. We run 10 independent seeds per  $(N, D)$  cell and average per-cell losses before fitting.

## H.2 CIFAR-100

**Description.** CIFAR-100 100-way image classification. The grid tests whether the form’s exponents and saturating wrapper transfer to vision with a different architecture and a different  $L_0$  ( $\ln 100 \approx 4.61$  nats).

**Architecture and grid.** PreActResNet [20], 5 configurations  $(n, w) \in \{(1, 16), (2, 24), (3, 32), (4, 48), (5, 64)\}$  where  $n$  is PreActBlocks per stage (depths  $6n + 2 \in \{8, 14, 20, 26, 32\}$ ) and  $w$  the base channel width, giving  $N \in \{84\text{K}, 400\text{K}, 1.1\text{M}, 3.3\text{M}, 7.5\text{M}\}$  params. Unique-data sweep  $D \in \{500, 2000, 8000, 25000, 50000\}$  training images. Validation loss measured on the standard 10,000-image test set.

**Training recipe.** SGD with momentum 0.9, weight decay  $5 \times 10^{-4}$ , batch size 128. Peak LR scales with width as  $0.1 \cdot (32/w)^{1/2}$  (anchor-tuned at  $w = 32$ ), held constant after  $W = 200$  linear-warmup steps. SGD+momentum is the canonical CIFAR ResNet optimizer [19]; we use constant LR for the stable phase rather than the conventional cosine decay so that the same stable run can feed multiple cooldown forks. We run 5 cooldown forks per stable run, log-spaced over  $[T_{\text{max}}/10, T_{\text{max}}]$  with  $T_{\text{max}} = 5 \times 10^6$  examples (square-root decay over the final 20% of fork compute), giving  $T_{\text{max}}/D \in \{100, 200, 625, 2500, 10,000\}$  epochs at the largest fork across  $D$  values (smallest fork is  $T_{\text{max}}/10$ , so  $\geq 10$  epochs everywhere). We apply standard CIFAR augmentation (random crop  $32 \times 32$  with 4-pixel padding, random horizontal flip).

## H.3 Darcy

**Description.** PDEBench 2D Darcy flow at  $\beta = 1.0$  [45], the canonical operator-learning benchmark for parametric elliptic PDEs. The task is to map a scalar permeability field  $a(x, y)$  on a  $128 \times 128$  grid to the steady-state pressure field  $u(x, y)$  that satisfies  $-\nabla \cdot (a(x, y)\nabla u(x, y)) = f(x, y)$  with prescribed boundary conditions. Loss is the relative- $L_2$  residual ( $L = \|\hat{u} - u\|_2/\|u\|_2$ , the canonical Li 2021 LpLoss ( $p = 2$ )), which gives  $L_0 = 1$  exactly under zero predictions on  $z$ -normalized targets.

**Architecture and grid.** Fourier neural operator (FNO; 31) with fixed depth ( $n_{\text{layer}} = 4$ ) and Fourier modes ( $n_{\text{modes}} = 12$ ), sweeping the hidden channel width  $w \in \{16, 24, 32, 48, 64, 96\}$

for 6 model configurations spanning  $\sim 90\text{K}$  to  $\sim 3.2\text{M}$  params. Unique-data sweep  $D \in \{10, 30, 100, 320, 1000, 3160, 9000\}$   $(a, u)$  pairs. Validation loss measured on a fixed 1,000-pair holdout.

**Training recipe.** AdamW with  $\beta = (0.9, 0.999)$  and weight decay  $10^{-4}$  (FNO defaults), peak LR  $10^{-3}$  held flat after  $W = 100$  linear-warmup steps, batch size 20  $(a, u)$  pairs per step (Li 2021 default), and 10 cooldown forks per stable run (square-root decay over the final 20% of fork compute, log-spaced over  $[\max(T_{\text{fork}}, T_{\text{max}}/100), T_{\text{max}}]$ ).  $T_{\text{max}}$  scales with  $D$ :  $5 \times 10^4$  at  $D = 30$ ,  $2 \times 10^5$  at  $D = 100$ ,  $5 \times 10^5$  at  $D = 320$ ,  $10^6$  at  $D \in \{1000, 3160\}$ , and  $2 \times 10^6$  at  $D = 9000$ , giving  $\sim 220$ – $2000$  epochs at the largest fork across cells.

## H.4 TinyStories

**Description.** TinyStories [15] next-token language modeling with a 2K BPE tokenizer trained on the TinyStories corpus (not Eldan & Li’s original 10K GPT-Neo vocabulary;  $L_0 = \ln 2000 \approx 7.60$  nats). TinyStories is the natural setting for fitting the multi-epoch behavior of the form: every cell on the grid admits  $T \gg D$ , so the  $b/T^\beta$  undertraining term and the  $cN^\gamma/D^\delta$  overfitting term are jointly identifiable.

**Architecture and grid.** GPT-style decoder-only transformer in the spirit of Eldan and Li [15]. 5 model sizes with  $(d_{\text{model}}, n_{\text{layer}}, n_{\text{head}}, d_{\text{ff}}) \in \{(64, 4, 4, 256), (128, 4, 4, 512), (192, 6, 6, 768), (320, 8, 8, 1280), (480, 10, 8, 1920)\}$ , giving  $N \in \{344\text{K}, 1.1\text{M}, 3.1\text{M}, 10.6\text{M}, 28.8\text{M}\}$  params. Context length 256 tokens, fixed across runs. Unique-data sweep  $D \in \{10^4, 10^5, 10^6, 10^7, 10^8, 5 \times 10^8\}$  unique tokens, giving 30 stable  $(N, D)$  runs and 300 cooldown-fork final-loss measurements. Validation loss measured on a fixed 2,000-document holdout from the TinyStories validation split.

**Training recipe.** AdamW with  $\beta = (0.9, 0.95)$  and weight decay 0.1 (GPT-style defaults), peak LR  $3 \times 10^{-4}$  held flat after  $W = 500$  linear-warmup steps, batch size 64 sequences of 256-token context = 16,384 tokens per step (fixed across configs), and 10 cooldown forks per stable run (square-root decay over the final 20% of fork compute, log-spaced over  $[\max(T_{\text{fork}}, T_{\text{max}}/100), T_{\text{max}}]$  with  $T_{\text{max}}$  scaling per cell from  $5 \times 10^7$  tokens at the smallest  $D$  to  $2.5 \times 10^9$  tokens at the largest, giving  $\sim 5$ – $5000$  epochs at the largest fork; the smallest forks ( $T_{\text{total}} = T_{\text{max}}/100$ ) at large- $D$  cells fall below one epoch and engage the  $D \mapsto \min(D, T)$  cap above). *Note:* a config drift on the later 30M-size submission set  $W = 100$  for those runs instead of 500; recorded loss is the post-cooldown final-loss, dominated by the late-training trajectory rather than the warmup duration, so  $L$  at any shared  $T_{\text{total}}$  is unaffected.

## I External refits

This appendix documents the five published LLM scaling-law grids we refit our form to: Chinchilla, Muennighoff, Gadre, Porian, and Farseer. In each case the grid covers only a subset of the  $(N, D, T)$  space that our form parameterizes; the per-dataset rationale for inclusion is in Section 3, and each subsection here follows a uniform structure: dataset description, model architecture and grid, and training recipe.

### I.1 Chinchilla

**Description.** Hoffmann et al. [26], transcribed by Besiroglu et al. [9] from DeepMind’s published Approach-3 isoFLOP figures (raw isoFLOP sweep was never released). The canonical compute-optimal reference grid for the Chinchilla parametric form. Single-epoch training ( $T = D$  throughout).

**Architecture and grid.** Decoder-only transformers; tokenizer is a 32K SentencePiece vocabulary on MassiveText. 245 rows spanning  $N \in [5.7 \times 10^7, 1.6 \times 10^{10}]$  params and  $D \in [2.4 \times 10^8, 3.2 \times 10^{11}]$  tokens at Chinchilla-optimal and near-optimal compute.

**Training recipe.** As reported by Hoffmann et al. [26]: cosine LR schedule with warmup, AdamW, single epoch over MassiveText. Loss is cross-entropy nats per token.

## I.2 Muennighoff

**Description.** Muennighoff et al. [36], source data is the NAMES\_TO\_VAL\_LOSSES dict in Hugging-Face’s datablations repository (lml-misc/parametric\_fit.ipynb). The only public grid with  $T > D$  (multi-epoch repetition).

**Architecture and grid.** Decoder-only transformers on C4; 50,257-token GPT-NeoX/GPT-2 vocabulary. 296 rows after averaging across 5 seed replicates per  $(N, D, T)$  cell ( $\Delta L \approx 0.005$  nats across seeds, well below fit-meaningful resolution);  $N \in [7.1 \times 10^6, 8.7 \times 10^9]$  params,  $D \in [1.0 \times 10^8, 5.0 \times 10^{11}]$  tokens, with the repetition ratio  $T/D$  varied at fixed  $(N, D)$  for  $D \in \{1.4 \times 10^9, 2.8 \times 10^9, 5.4 \times 10^9, 1.4 \times 10^{10}, 4.2 \times 10^{10}\}$ .

**Training recipe.** As reported by Muennighoff et al. [36]: cosine LR schedule, AdamW, multi-epoch passes over data-constrained subsets of C4. Loss is cross-entropy nats per token.

## I.3 Gadre

**Description.** Gadre et al. [16], published CSV at mlfoundations/scaling. The over-trained-regime grid: single-epoch models sweeping the token multiplier  $M = D/N$  from Chinchilla-optimal  $\sim 20$  up to  $\sim 640$ . The published CSV mixes three corpora at the same  $(N, D)$ ; we filter to rw\_original (RefinedWeb) to match Porian’s corpus and enable direct over-trained-vs-Kaplan comparison. Single epoch ( $T = D$ ).

**Architecture and grid.** Decoder-only transformers on RefinedWeb; 50,432-token tokenizer. 104 rows after corpus filter, spanning  $N \in [8.4 \times 10^7, 7.0 \times 10^9]$  params and  $D \in [5.4 \times 10^8, 8.4 \times 10^{11}]$  tokens.

**Training recipe.** As reported by Gadre et al. [16]: cosine LR schedule with linear warmup, AdamW, single-epoch over RefinedWeb. Loss is cross-entropy nats per token.

## I.4 Porian

**Description.** Porian et al. [41], used as a Kaplan stand-in (Kaplan’s 2020 raw data isn’t public). Porian re-runs Chinchilla-style training under several LR schedules including a Kaplan-style decay-to-fixed- $T_{\max}$ .

**Architecture and grid.** Decoder-only transformers on RefinedWeb; 32K SentencePiece tokenizer. 238 rows after filtering to the rw|base|long\_warmup|kaplan\_decay subset (the closest reproduction of Kaplan-style training; other protocols dropped to avoid mixing schedules in one fit), spanning  $N \in [5.2 \times 10^6, 9.0 \times 10^8]$  params and  $D \in [3.6 \times 10^7, 1.9 \times 10^{10}]$  tokens, with a denser experimental grid near the compute-optimal frontier. Single epoch ( $T = D$ ).

**Training recipe.** As reported by Porian et al. [41]: long-warmup cosine schedule with optional Kaplan-style decay-to-fixed- $T_{\max}$ , AdamW with carefully tuned batch size and LR, single epoch over RefinedWeb. Loss is cross-entropy nats per token.

## I.5 Farseer

**Description.** Li et al. [29]: the largest open single-recipe scaling-law dataset publicly available (>400 dense-LM runs, single-epoch, cosine-to-zero LR schedule). Source: the Farseer/\_sc cohort of the billzid/Farseer public W&B project (cosine-to-zero dense, 460 raw runs), reduced to 456 cells after dropping divergent runs (running-min lm\_loss > 6) and taking MIN over LR/batch-size replicates per  $(N, D, T)$  cell. The companion billzid/predictable-scale project (separate \_mlr1e-5 cohorts for dense and MoE) is not used in our fits.

**Architecture and grid.** Dense decoder-only transformers; 65,536-token tokenizer on a web + math + code mixture. 456 rows after filtering, spanning  $N \in [9.6 \times 10^8, 6.4 \times 10^9]$  params and  $D \in [9.0 \times 10^{10}, 4.3 \times 10^{11}]$  tokens. Single-epoch ( $T = D$ ).

**Training recipe.** As reported by Li et al. [29]: cosine-to-zero LR schedule with warmup, AdamW, single-epoch over the web/math/code mixture. Loss is cross-entropy nats per token. Per-run  $L$  is the server-side running-min via W&B’s `summaryMetrics.lm_loss.min`.

## J Compute-optimal model size at fixed unique data

This appendix derives the optimal model size  $N^*$  at fixed unique data  $D$  under our form, in two regimes: the asymptotic limit  $T \rightarrow \infty$ , and the finite-compute case using the planning approximation  $C \approx kNT$ . We then verify that no other parametric scaling law referenced in this paper admits an analogous interior minimum in  $N$  at fixed  $D$ .

**Asymptotic optimum** ( $T \rightarrow \infty$ ). At fixed  $D$  as  $T \rightarrow \infty$ , the undertraining term  $b/T^\beta$  vanishes and

$$h_\infty(N, D) = \frac{a}{N^\alpha} + \frac{cN^\gamma}{D^\delta}.$$

The stationarity condition  $\partial h_\infty / \partial N = 0$  gives

$$-\frac{\alpha a}{N^{\alpha+1}} + \frac{\gamma c N^{\gamma-1}}{D^\delta} = 0 \implies N_\infty^*(D) = \left( \frac{\alpha a D^\delta}{\gamma c} \right)^{1/(\alpha+\gamma)}. \quad (6)$$

This is an interior minimum:  $\partial^2 h_\infty / \partial N^2 = \alpha(\alpha+1)a/N^{\alpha+2} + \gamma(\gamma-1)cN^{\gamma-2}/D^\delta$ , which is positive at  $N_\infty^*$  for  $\alpha, \gamma > 0$  and  $a, c > 0$  (each term contributes a positive curvature near the optimum). Below  $N_\infty^*$  the undercapacity term dominates and increasing  $N$  helps; above  $N_\infty^*$  the overfitting term dominates and increasing  $N$  raises the asymptotic loss. Because the wrapper  $h/(1+h)$  is monotone, the same  $N_\infty^*$  minimizes  $L$  itself.

**Finite-compute optimum.** Using  $T = C/(kN)$ , at fixed  $C, D$  we minimize

$$h(N, D, C) = \frac{a}{N^\alpha} + \frac{b k^\beta N^\beta}{C^\beta} + \frac{c N^\gamma}{D^\delta}.$$

Setting  $\partial h / \partial N = 0$  gives the implicit relation

$$\alpha a = \frac{\beta b k^\beta N^{*\alpha+\beta}}{C^\beta} + \frac{\gamma c N^{*\alpha+\gamma}}{D^\delta}, \quad (7)$$

which has a unique solution since the right-hand side is monotone increasing in  $N$  from 0 at  $N = 0$  to  $\infty$ . Two limits recover the boundary behavior:

*Limit  $D \rightarrow \infty$  (data-rich, Chinchilla regime).* The third term in Equation (7) vanishes, giving

$$N^*(C) = \left( \frac{\alpha a C^\beta}{\beta b k^\beta} \right)^{1/(\alpha+\beta)} \propto C^{\beta/(\alpha+\beta)}. \quad (8)$$

With Chinchilla-like exponents  $\alpha \approx \beta$ ,  $N^*(C) \propto C^{1/2}$ , recovering Hoffmann et al. [26]’s compute-optimal scaling.

*Limit  $C \rightarrow \infty$  at fixed  $D$ .* The second term in Equation (7) vanishes, recovering  $N_\infty^*(D)$  from Equation (6). The compute-optimal model size therefore saturates at a finite value as compute grows past the point at which adding capacity costs more in overfitting than it gains in undercapacity reduction. This is the data-constrained shift qualitatively documented by Muennighoff et al. [36]: spending more compute on a fixed unique-data pool eventually requires shrinking the model rather than enlarging it.

**Other parametric forms.** Among the parametric scaling laws of Section 5, none admits a non-trivial  $N^*$  at fixed  $D$  as  $T \rightarrow \infty$ :

- *Chinchilla.*  $L = E + A/N^\alpha + B/D^\beta$  is monotone non-increasing in  $N$ .
- *Kaplan Eq. 1.5.*  $L = [(N_c/N)^{\alpha N/\alpha_D} + D_c/D]^{\alpha_D}$ . As  $N \rightarrow \infty$  the first bracket term vanishes and  $L \rightarrow (D_c/D)^{\alpha_D}$ ; monotone non-increasing in  $N$ .

- *Muennighoff*.  $L = E + A/(N')^\alpha + B/(D')^\beta$  with effective  $N'$  saturating at  $N(1 + R_N^*)$  as  $N \rightarrow \infty$ . Both terms are monotone non-increasing in  $N$ .
- *M4*. Single-axis form, monotone by construction.
- *Farseer*.  $N$ -dependent exponents but no overfitting term; inherits Chinchilla’s monotonicity in  $N$ .
- *BNSL*. Can express non-monotone behavior via empirical breakpoints, but the breakpoint locations and shapes are fit, not predicted from  $(N, D)$  structure.

The U-shape in  $L(N)$  at fixed  $D$  is therefore a structural feature unique to our form among the reference set, and matches the empirical observation of Hernandez et al. [24] that validation loss is non-monotone in capacity under heavy data repetition.

## K Cost-optimal allocation

A calibrated scaling law lets us answer two reciprocal practitioner questions: (P1) given a target validation loss  $L^*$ , what is the minimum dollar cost  $\mathcal{B}^*$  to reach it, and how should that budget split across model size  $N$ , unique data  $D$ , and training duration  $T$ ? (P2) given a fixed dollar budget  $\mathcal{B}_{\max}$ , what is the lowest validation loss achievable, and what allocation achieves it? When training compute is the sole cost (the Chinchilla setup), (P1) and (P2) collapse to dual readouts of the compute-optimal frontier. When unique data must be generated, labeled, or licensed at non-trivial per-example cost, both require joint optimization over  $(N, D, T)$  with two independent cost terms.

**Setup.** Let  $\rho_D$  be the dollar cost per unique training example (label, simulation run, scraped token, etc.) and  $\rho_C$  the dollar cost per FLOP. Using the standard approximation  $C \approx kNT$ , the dollar cost is

$$\mathcal{B}(N, D, T) = \rho_D \cdot D + \rho_C \cdot kNT. \quad (9)$$

Both (P1) and (P2) are smooth constrained optimizations on  $\mathbb{R}_{>0}^3$  under our form  $L = E + (L_0 - E)h/(1+h)$  with  $h = a/N^\alpha + b/T^\beta + cN^\gamma/D^\delta$ . They are duals: the same Lagrangian governs both, and the optimal allocation  $(N^*, D^*, T^*)$  that solves (P1) at target  $L^*$  also solves (P2) at budget  $\mathcal{B}^*(L^*)$ .

**(P1) Target-loss optimum.** Form the Lagrangian  $\mathcal{L}_1 = \mathcal{B} + \mu(L - L^*)$  with  $\mu \geq 0$ . Setting  $\partial\mathcal{L}_1/\partial X = 0$  for  $X \in \{N, D, T\}$  gives the stationarity conditions

$$-\frac{\rho_C kT}{\partial L/\partial N} = -\frac{\rho_D}{\partial L/\partial D} = -\frac{\rho_C kN}{\partial L/\partial T} = \mu, \quad (10)$$

i.e., *equate the marginal dollar cost per unit of loss reduction across all three axes* (the minus signs render  $\mu \geq 0$  since  $\partial L/\partial X < 0$  at any interior optimum). Combined with the loss constraint  $L(N, D, T) = L^*$ , Equation (10) pins down a unique  $(N^*, D^*, T^*)$ . Substituting into Equation (9) gives  $\mathcal{B}^*(L^*) = \rho_D D^* + \rho_C kN^* T^*$ , the minimum dollar spend to reach  $L^*$ .

**(P2) Budget-constrained optimum.** Form  $\mathcal{L}_2 = L + \lambda(\mathcal{B} - \mathcal{B}_{\max})$  with  $\lambda \geq 0$ . The stationarity conditions are

$$\frac{\partial L/\partial N}{\rho_C kT} = \frac{\partial L/\partial D}{\rho_D} = \frac{\partial L/\partial T}{\rho_C kN} = -\lambda, \quad (11)$$

i.e., *equate the marginal loss reduction per dollar across all three axes*. Together with  $\mathcal{B}(N, D, T) = \mathcal{B}_{\max}$  this pins down  $(N^*, D^*, T^*)$  and yields  $L^* = L(N^*, D^*, T^*)$ . The two sets of stationarity conditions are reciprocals (Equation (10) divides what Equation (11) multiplies), so the two optima trace out the same Pareto frontier  $\{(\mathcal{B}^*, L^*)\}$  and either problem can be read off the other.

**Feasibility and boundary behavior.** The form’s  $[E, L_0]$  ceiling makes infeasibility of (P1) detectable in closed form. Inverting the wrapper, the difficulty  $h$  required to hit a target  $L^*$  is

$$h^* = \frac{L^* - E}{L_0 - L^*}, \quad (12)$$

which is positive and finite iff  $L^* \in (E, L_0)$ . Outside this open interval the constraint manifold  $\{(N, D, T) : L(N, D, T) = L^*\}$  is empty:

- $L^* < E$ : asks for a model below the irreducible loss; (P1) has no solution. The Lagrangian’s stationarity conditions become inconsistent and the Newton iteration diverges or stalls. The diagnostic is direct: compute  $h^*$ , check the sign.
- $L^* \geq L_0$ : trivially achievable by an untrained model. The optimizer pushes one of  $a/N^\alpha$ ,  $b/T^\beta$ , or  $cN^\gamma/D^\delta$  toward infinity (e.g.,  $T \rightarrow 0$ ), so  $\mathcal{B}^* \rightarrow 0$ . (P1) at this target is well-defined but uninformative.
- $L^* \rightarrow E^+$ :  $h^* \rightarrow 0$ , which requires  $a/N^\alpha + b/T^\beta + cN^\gamma/D^\delta \rightarrow 0$  jointly. This forces  $N \rightarrow \infty$  and  $T \rightarrow \infty$ , with  $D \rightarrow \infty$  along a path where  $D^\delta$  outpaces  $N^\gamma$  in the overfitting term (see Appendix B, Row 6). The cost  $\mathcal{B}^* \rightarrow \infty$ . So  $L^* = E$  is a limit point of the feasible region rather than an achievable target: a finite-capacity model cannot represent the data’s true entropy.

Within the feasible interior  $L^* \in (E, L_0)$ , the optimum is attained at *finite*  $(N^*, D^*, T^*)$ . At any fixed  $D$ , the form admits a finite interior minimum  $N^*(D)$  from the U-shape competition between the capacity term and the overfitting term (Appendix J derives  $N_\infty^*(D) = (\alpha a D^\delta / \gamma c)^{1/(\alpha+\gamma)}$  in the asymptotic  $T \rightarrow \infty$  limit), achieving  $L^*(D) > E$  at that finite  $N^*(D)$ . The family  $\{L^*(D) : D > 0\}$  traces out an achievable frontier that approaches  $E$  only as  $D \rightarrow \infty$ . (P1) at any target above this frontier has a finite-allocation solution; only  $L^* = E$  requires the joint  $\infty$  limit. The numerical solver should compute  $h^*$  first via Equation (12) and reject targets outside  $(E, L_0)$  before iterating.

**Recipe.** The general system has no closed form, so we solve numerically. The procedure for either (P1) or (P2):

1. Calibrate the form on a domain-specific training grid to obtain  $(E, a, b, c, \alpha, \beta, \gamma, \delta)$  and  $L_0$  (Section 3).
2. Specify the price pair  $(\rho_D, \rho_C)$  for the deployment setting and an architecture-dependent FLOP-per-step constant  $k$ .
3. Solve Equation (10) (for P1) or (11) (for P2) jointly with the active constraint over  $(N, D, T)$  until the stationarity conditions hold to tolerance.
4. Read off the dual quantities:  $\mathcal{B}^*$  and  $(N^*, D^*, T^*, T^*/D^*)$  for P1, or  $L^*$  and the same allocation for P2.

**Cost ratios and the data-constrained regime.** A useful summary statistic is the dollar-cost ratio  $\eta = \rho_D / \rho_C$ . For LLM pretraining on web-scraped data  $\eta$  is small (data is cheap, compute dominates) and the Chinchilla-style optimum approximates both (P1) and (P2). For physical-simulation surrogates, RL data generation, and expert label acquisition,  $\eta$  is large (each example is expensive). As  $\eta$  grows, the optimum shifts toward smaller  $D$  (fewer expensive examples), more epochs, and more compute spent revisiting the same data.

**Compute is not exactly proportional to dollars.** Equation (9) treats compute as linear in dollars via a constant  $\rho_C$ , but in practice users pay for GPU-hours, not FLOPs. Small models cannot fully utilize a multi-GPU node (low effective batch size, low arithmetic intensity), large models incur communication overhead, and memory bandwidth often bottlenecks before compute. The apparent  $\rho_C$  therefore depends on  $N$  and on the cluster topology. The recipe is correct under a constant- $\rho_C$  idealization and useful as a first-cut allocation; accurate cost-aware fits should treat  $\rho_C(N)$  as a function calibrated to the actual hardware.

**Stationarity conditions in terms of  $\partial h$ .** The partial derivatives of  $h = a/N^\alpha + b/T^\beta + cN^\gamma/D^\delta$  are

$$\frac{\partial h}{\partial N} = -\frac{\alpha a}{N^{\alpha+1}} + \frac{\gamma c N^{\gamma-1}}{D^\delta}, \quad \frac{\partial h}{\partial D} = -\frac{\delta c N^\gamma}{D^{\delta+1}}, \quad \frac{\partial h}{\partial T} = -\frac{\beta b}{T^{\beta+1}},$$

and  $\partial L / \partial X = (L_0 - E)(\partial h / \partial X) / (1 + h)^2$  for  $X \in \{N, D, T\}$ . Substituting into Equations (10) and (11) gives the stationarity conditions in terms of  $\partial h$ :

$$(P2) : \frac{1}{\rho_C k T} \frac{\partial h}{\partial N} = \frac{1}{\rho_D} \frac{\partial h}{\partial D} = \frac{1}{\rho_C k N} \frac{\partial h}{\partial T} = -\frac{\lambda(1+h)^2}{(L_0 - E)}, \quad (13)$$

$$(P1) : \rho_C k T \cdot \left(\frac{\partial h}{\partial N}\right)^{-1} = \rho_D \cdot \left(\frac{\partial h}{\partial D}\right)^{-1} = \rho_C k N \cdot \left(\frac{\partial h}{\partial T}\right)^{-1} = -\frac{\mu(L_0 - E)}{(1+h)^2}, \quad (14)$$

each system four equations in four unknowns ( $\{N^*, D^*, T^*, \lambda\}$  for P2, replacing  $\lambda$  with  $\mu$  for P1, with  $\mu = 1/\lambda$  at the dual optimum).

**Asymptotic regimes (both problems).** (i) When  $\rho_D \gg \rho_C$  (data dominates cost):  $D^*$  is small, multi-epoch training is preferred,  $T^*$  scales freely until the overfitting term  $cN^\gamma/D^\delta$  saturates the wrapper. (ii) When  $\rho_D \ll \rho_C$  (compute dominates cost): the FOC for  $D$  pushes  $D^* \rightarrow \infty$ , the overfitting term vanishes, and  $(N^*, T^*)$  approach the Chinchilla compute-optimal allocation in  $(N, D=T)$  variables; the Chinchilla single-epoch convention  $T = D$  is recovered by selecting  $D$  at the smallest value already killing the overfitting term, since once  $cN^\gamma/D^\delta$  is negligible the loss is invariant under further  $D$  increases. (iii) Balanced  $\rho_D \sim \rho_C$ : numerical solution of the joint conditions.

**Log-convexity and uniqueness.** Minimizing  $L$  is equivalent to minimizing  $h(N, D, T) = a/N^\alpha + b/T^\beta + cN^\gamma/D^\delta$ , since  $L$  is monotone in  $h$  (the wrapper  $h/(1+h)$  is monotone non-decreasing). Substituting  $u = \log N$ ,  $v = \log D$ ,  $w = \log T$ ,  $h = ae^{-\alpha u} + be^{-\beta w} + ce^{\gamma u - \delta v}$ , a sum of exponentials of linear functions of  $(u, v, w)$ , which is convex (each  $e^{\text{affine}}$  term is convex; sum of convex is convex). In fact  $h$  is *strictly* convex in  $(u, v, w)$  when  $a, b, c, \alpha, \beta, \gamma, \delta > 0$ : its Hessian is block-diagonal in  $\{(u, v), w\}$ , with the  $(w, w)$  entry  $b\beta^2 e^{-\beta w} > 0$  and the  $(u, v)$  block having determinant  $ac\alpha^2\delta^2 e^{(\gamma-\alpha)u - \delta v} > 0$  and positive trace, so both blocks are positive definite. The dollar cost  $\mathcal{B} = \rho_D e^v + \rho_C k e^{u+w}$  is convex in  $(u, v, w)$ , so the feasible set  $\{\mathcal{B} \leq \mathcal{B}_{\max}\}$  is convex. Minimizing a strictly convex function on a convex feasible set yields a unique optimum, so (P1) and (P2) each have a unique solution  $(N^*, D^*, T^*)$ , and standard convex-optimization tools converge to it from any feasible starting point. (At the boundary  $c = 0$  or  $b = 0$  the strict convexity fails and the optimum on the  $D$  or  $T$  axis becomes degenerate.)

**Numerical recipe.** For (P2): grid-search  $(N, D, T)$  on the constraint manifold  $\rho_D D + \rho_C k N T = \mathcal{B}_{\max}$ , locate the minimum- $L$  cell, refine via Newton iterations on Equations (13). For (P1): grid-search on the isoloss manifold  $L(N, D, T) = L^*$ , locate the minimum- $\mathcal{B}$  cell, refine via Newton iterations on Equations (14). In both cases the convex parameterization  $(\log N, \log D, \log T)$  keeps the optimization well-conditioned across the many orders of magnitude that  $(N, D, T)$  may span.

## L Far extrapolation: a soft prior on $E$

The Section 3.2 and Appendix O extrapolation tables use the high- $C$  and high- $D$  holdouts from within the general distribution of training runs. *Far extrapolation* is the more aggressive question: predict loss at held-out high-compute runs far beyond the regime in which the fit was calibrated. The Farseer dataset provides several training runs that meet this criterion. Run as-is, our form does notably worse here than at near-extrapolation; the diagnosis below identifies the cause as a wrapper-induced identifiability collapse on the fitted asymptote  $E$ , and we propose a one-line fitting-protocol fix (a one-sided log-space prior on  $E$ ) that recovers state-of-the-art performance at far compute.

**Setup.** We adopt Farseer’s own published compute-extrapolation benchmark: 7 large-model held-out runs distributed in the file `val_big_d_full.csv` alongside the main W&B dump, with widths  $w \in \{2304, 2432, 2752, 3072, 3328, 5120\}$ ,  $N \in [2.27\text{B}, 25.1\text{B}]$ , and held-out compute  $C \in [6.8 \times 10^{21}, 2.0 \times 10^{22}]$  FLOPs (2 to  $6\times$  beyond the cohort’s  $C \leq 3.5 \times 10^{21}$ ). We fit each form on the full 456-cell cohort and predict on the 7 targets’ `smooth_loss` column (training cross-entropy, same units as the cohort’s  $L$ ). The held-out targets sit at  $L \in [1.78, 1.88]$  nats, well above the fitted asymptote of either form. Errors are reported in log-loss space.

**Naive far-extrapolation results.** As fit, the comparison places ours last among the three baselines (**best** and second best highlighted per column; error bars: bootstrap  $\pm$  std over 200 resamples):

Form	Mean  err	Median  err	Max  err	MBE
Chinchilla (5 params)	0.0204 $\pm$ 0.0048	0.0165 $\pm$ 0.0045	0.0383 $\pm$ 0.0058	+0.0204 $\pm$ 0.0054
Farseer (9 params)	<b>0.0115 <math>\pm</math> 0.0024</b>	<b>0.0101 <math>\pm</math> 0.0040</b>	<b>0.0317 <math>\pm</math> 0.0041</b>	<b>-0.0102 <math>\pm</math> 0.0051</b>
Ours, vanilla (8 params)	0.0382 $\pm$ 0.0026	0.0355 $\pm$ 0.0020	0.0567 $\pm$ 0.0066	-0.0382 $\pm$ 0.0026

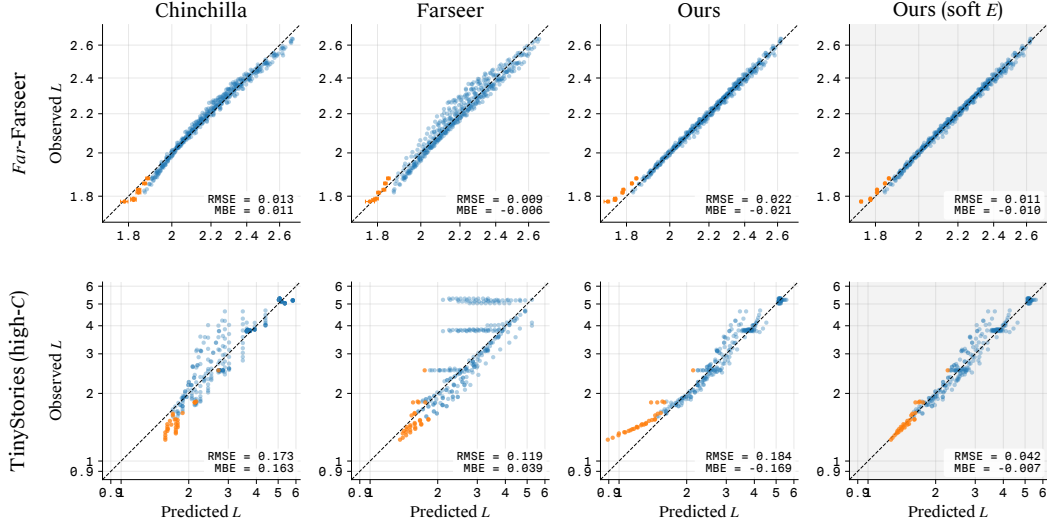


Figure 4: Observed vs. predicted loss on the *Far-Farseer* and *TinyStories* datasets across four forms (Chinchilla, Farseer, our vanilla form, and our corrected form), on benchmarks where vanilla  $E$ -collapse is measurable. *Top row* (“*Far-Farseer*”): Farseer’s published compute-extrapolation benchmark (held-out targets in orange, in-cohort cells in blue). *Bottom row*: *TinyStories* high- $C$  holdout (orange = held-out cells). Columns sweep four forms: Chinchilla, Farseer, our vanilla 8-parameter form, and our form with the one-sided log-space prior on  $E$  (Equation (15); highlighted). Each panel reports per-protocol RMSE and mean bias error (MBE). The vanilla “*Ours*” column shows the issue: orange held-out points sit consistently above the diagonal (underpredicting), the signature of an  $E$  placed below the data’s true asymptote. The “*Ours (soft  $E$ )*” column shows the recipe: held-out predictions move onto the diagonal, with RMSE matching Chinchilla on *Far-Farseer* (0.011 vs. 0.013) and dominating every baseline on *TinyStories* high- $C$  (0.042 vs. 0.119–0.184).

Two diagnostic features stand out. First, the sign of our form’s bias is consistently *negative*: it under-predicts loss at far compute, by  $1.9\times$  the magnitude of Chinchilla’s (over-predicting) bias and  $3.7\times$  the magnitude of Farseer’s (also under-predicting, but barely). Second, our form’s fitted  $E = 0.315$  on the Farseer training cohort, while Chinchilla’s fitted  $E = 1.471$ ; the held-out targets sit at  $L \approx 1.83$ , roughly 1.16 nats above our floor and 0.36 nats above Chinchilla’s. Our form has placed its asymptote far below where the data actually flatten. Farseer’s own form leads on every column, as expected for the form whose grid this is and which carries an extra parameter ( $N$ -dependent exponents) tuned for exactly this regime; it serves as a fair-comparison ceiling against which to evaluate any fix to ours.

**Diagnosis: wrapper-induced  $E$ -collapse.** The under-prediction is structural, not a fitting accident. Three mechanisms compound:

- *The asymptote is extrapolated, not measured.* Within the fit range,  $E$  is identifiable only as “wherever the form needs to land for the curvature to match.” Any slow tail that the form cannot represent (irreducible label noise, expressivity floor, distribution-shift residual) is invisible at observed  $C$ , so the fit absorbs the visible decay into the power-law terms  $a/N^\alpha + b/T^\beta + cN^\gamma/D^\delta$  and projects  $E$  to wherever those terms extrapolate to. Power-law terms never quite reach zero, so the projected  $E$  ends up below the true floor.
- *Wrapper identifiability collapse.* Our saturating wrapper  $L = E + (L_0 - E) \cdot h/(1 + h)$  makes  $E$  and the swing coefficient  $(L_0 - E)$  quasi-collinear inside the fit window: any pair satisfying the local equation matches the bulk equally well, so  $E$  is identified only when observations approach the asymptote (which is precisely what far extrapolation withholds). Lower  $E$  also enlarges  $(L_0 - E)$ , pushing the wrapper’s high-curvature inflection ( $h=1$ ) into the loss range the data occupies, and the optimizer rewards this with a marginally lower bulk Huber loss. This is a wrapper effect, not a cross-term effect: even the  $c=0$  sibling of our form (same wrapper, no overfitting term) collapses  $E$  to the numerical floor on *TinyStories*

high- $C$ . Chinchilla’s additive form has no wrapper, so its  $E$  is identified by the asymptotic envelope alone, which is also where the truth’s asymptote sits on average.

- *Log-space fitting is generous to the asymptote.* The fit minimizes  $(\log \hat{L} - \log L)^2$ . Near the floor, residuals are large fractionally even when small absolutely, so the fit pulls hard to match the lowest-loss points. With few low-loss anchors in the fit window (the definition of “far extrapolation”), this pull is poorly constrained and tends to drag  $E$  low. The softplus reparameterization  $E = \text{softplus}(x_E)$  used to enforce  $E \geq 0$  adds a mechanical sticking point: once  $x_E$  drifts negative,  $\partial E / \partial x_E \rightarrow 0$  and there is no restoring force.

The bias has a guaranteed sign: the form is monotone-decreasing in  $C$  and approaches  $E$  from above, so  $E_{\text{fit}} < E_{\text{true}}$  implies  $\hat{L} < L_{\text{true}}$  at any  $C$  far enough out. This is not specific to our form; it is the price every parametric form pays for having a finite parameter count and a fitted asymptote, with the wrapper amplifying the failure mode for our family. The reason Chinchilla’s far extrapolation is more honest here is precisely that its rigidity (additive structure, no wrapper, no cross term) acts as a regularizer on  $E$ .

**Recipe: a one-sided log-space prior on  $E$ .** The fix follows directly from the diagnosis: when  $E$  is unidentified by bulk fit (no observations near the asymptote), supply a weak external constraint that intervenes only when the optimizer drives  $E$  below an empirical floor. Augment the Huber objective with a one-sided L2 hinge on  $\log E$ :

$$\mathcal{L}^*(\theta) = \mathcal{L}(\theta) + \lambda \cdot [\max(0, \log(m/\kappa) - \log E)]^2, \quad (15)$$

where  $m = \min L_{\text{obs}}$  on the training cohort,  $\kappa = 1.5$  is a fixed offset (so the floor sits 33% below the lowest observed loss), and  $\lambda = N_{\text{train}}/4$  scales linearly with cohort size to keep the prior’s relative strength constant against the Huber sum. The penalty is silent when  $E \geq m/\kappa$  and smoothly active below it, so on grids where the unconstrained fit already places  $E$  above the floor the prior is a strict no-op. The form’s mathematical structure is unchanged; predictions at any  $(N, D, T)$  are still computed by  $L = E + (L_0 - E) \cdot h / (1 + h)$ , and only the parameter-selection objective gains the hinge.

Form	Mean  err	Median  err	Max  err	MBE
Chinchilla (5 params)	0.0204 ± 0.0048	0.0165 ± 0.0045	0.0383 ± 0.0058	+0.0204 ± 0.0054
Farseer (9 params)	<b>0.0115 ± 0.0024</b>	<b>0.0101 ± 0.0040</b>	<b>0.0317 ± 0.0041</b>	<b>-0.0102 ± 0.0051</b>
Ours, vanilla (8 params)	0.0382 ± 0.0026	0.0355 ± 0.0020	0.0567 ± 0.0066	-0.0382 ± 0.0026
Ours, $E$ -hinge prior (8 params)	<u>0.0174 ± 0.0017</u>	<u>0.0148 ± 0.0020</u>	0.0385 ± 0.0025	<u>-0.0174 ± 0.0017</u>

The prior moves our form from *worst* to second on the same grid, ahead of Chinchilla on every column and trailing only Farseer’s home-turf form. At the prior fit,  $E$  rises from 0.315 to 1.211 (versus Chinchilla’s 1.471 and the held-out targets’  $L \approx 1.83$ ), and per-target absolute errors drop on all 7 targets relative to the vanilla fit. The MBE collapses from  $-0.0382$  to  $-0.0174$ , smaller in magnitude than Chinchilla’s  $+0.0204$ , so the prior closes most of the asymptote gap. The held-out RMSE in  $L$ -space drops from 0.0391 (vanilla) to 0.0201 (prior), a  $1.95\times$  reduction. We do not apply the same prior to the Farseer form: the hinge is a targeted fix for saturating-wrapper forms (see below), and Farseer is an additive  $L(N, D)$  form whose vanilla MBE of  $-0.0102$  is consistent with a near-correctly-placed asymptote.

**Same recipe on TinyStories high- $C$ .** We applied the same recipe to the TinyStories high- $C$  holdout from Section 3.2, where vanilla fitting also collapses  $E$  to the numerical floor. The recipe cuts held-out log-RMSE from 0.184 to 0.042, a  $4.4\times$  reduction that moves our form from 4th out of 6 to first on this protocol (best baseline: Muennighoff at 0.095). Figure 4 (bottom row) shows the same diagnosis as on Farseer: vanilla held-out points sit consistently below the diagonal, and the recipe pushes them onto it. Both demonstrations use the same fixed  $(\kappa, \lambda)$  pair without per-dataset tuning, so the recipe is reproducible from data alone.

**No harm where the prior isn’t needed.** On the other three TinyStories protocols (high- $D$ , low- $C$ , low- $D$ , where vanilla  $E$  does not collapse), the prior changes log-RMSE by less than the optimizer noise floor. The prior is therefore safe to deploy by default on saturating-wrapper forms (ours and

ablations) without adversely affecting fits where  $E$  is already well-identified. It should *not* be applied to additive baselines (Chinchilla, Muennighoff, Gadre, BNSL, M4, Farseer): forced upward on a form with no wrapper, the prior distorts the additive decay terms instead. We treat the prior as a property of the wrapper family, not a universal tweak.

## M MNIST high- $D$ : where the cross term over-extrapolates

On MNIST, our form’s high- $D$  holdout RMSE is  $0.137 \pm 0.004$ , behind Muennighoff at  $0.122 \pm 0.005$  and only marginally ahead of Chinchilla at  $0.123 \pm 0.001$  (Table 2). The gap survives several plausible data interventions (collision aggregation, dropping sub-1-epoch rows) and form perturbations, so it is neither a data-extraction nor an optimization artifact. This appendix isolates the cause via two  $D$ -axis sweeps and uses them to characterize the regime in which the form’s overfitting term is a structural asset versus a structural liability. *Note*: for clarity of analysis, we remove all sub-1-epoch rows from the training set before fitting.

**Hypothesis.** The cross term  $cN^\gamma/D^\delta$  in our form earns its keep by fitting multi-epoch overfitting at small  $D$ . On MNIST, the smallest- $D$  cells ( $D \in \{10, 20, 50, 100\}$ ) exhibit heavy overfitting; with no other knob in the form able to express that, the optimizer is forced to pick  $(c, \gamma, \delta)$  values large enough for the cross term to dominate  $h$  at those cells. The same coefficients then govern the cross term’s value at every  $D$  in the prediction grid, including the held-out  $D = 60,000$  where overfitting has reduced substantially. The result: a residual cross-term contribution at the asymptote that the wrapper translates into a small but persistent over-prediction. Chinchilla and Muennighoff lack a cross term, so they have nothing to misextrapolate. The cross term that earns the form its small- $D$  fit overshoots when extrapolated to larger  $D$  where overfitting has vanished.

**Sweep design.** The hypothesis makes two separable claims: (i) small- $D$  contamination of the training set is what drives the cross term’s high- $D$  over-extrapolation, and (ii) the resulting over-prediction manifests across a wide range of held-out  $D$ , not only at the asymptote. We test each with one  $D$ -axis sweep, varying a single training-set choice at a time. *Sweep A* fixes the held-out target at the asymptote  $D = 60,000$  and progressively pulls smaller- $D$  cells into training, asking: how much small- $D$  contamination does it take to break the form’s high- $D$  extrapolation? *Sweep B* fixes the training set to always include the smallest- $D$  cells (contamination held maximal) and slides the held-out  $D$  from 320 up through 60,000, asking: across what range of held-out  $D$  does the over-extrapolation persist? In each table the parameter  $k$  indexes the size of the working subset (training  $\cup$  held-out); training contains  $k - 1$  cells.

**Sweep A: contamination grows; target fixed at the asymptote.** The working subset always contains the held-out  $D = 60,000$  and the  $k - 1$  next-largest cells, so the smallest- $D$  cell in training descends from 1,000 ( $k = 5$ ) down to 10 ( $k = 10$ ).

$k$	smallest $D$ in train	Ours	Chinchilla	Muennighoff
5	1000	$0.087 \pm 0.002$	$0.107 \pm 0.001$	$0.086 \pm 0.002$
6	320	$0.084 \pm 0.001$	$0.109 \pm 0.001$	$0.094 \pm 0.003$
7	100	$0.096 \pm 0.002$	$0.111 \pm 0.001$	$0.093 \pm 0.002$
8	50	$0.098 \pm 0.002$	$0.112 \pm 0.001$	$0.096 \pm 0.003$
9	20	$0.108 \pm 0.003$	$0.110 \pm 0.001$	$0.098 \pm 0.003$
10	10	$0.126 \pm 0.004$	$0.159 \pm 0.000$	$0.109 \pm 0.001$

At  $k = 6$  ours wins cleanly with non-overlapping CIs (RMSE 0.084 vs Muennighoff 0.094, Chinchilla 0.109). Each step adds a smaller- $D$  cell, our form’s RMSE rises monotonically, and the bias flips from negative (under-prediction) at  $k = 5-7$  to  $+0.085$  at  $k = 10$ . Adding  $D = 10$  to training (the  $k = 9 \rightarrow 10$  step) produces the biggest single-step jump for ours ( $0.108 \rightarrow 0.126$ ), confirming that the small- $D$  corner is what poisons the cross term’s behavior.

**Sweep B: contamination held maximal; target slides up.** The working subset always contains the smallest- $D$  cells, plus  $k - 5$  larger- $D$  cells; the held-out target is the largest cell in the subset, sliding from  $D = 320$  ( $k = 5$ ) up to  $D = 60,000$  ( $k = 10$ ). If the cross term over-predicts at every

$D$  where overfitting has ebbed, ours should over-predict on every held-out target, while Chinchilla and Muennighoff (no cross term) should not.

$k$	held-out $D$	Ours	Chinchilla	Muennighoff
5	320	$0.253 \pm 0.007$	$0.244 \pm 0.001$	$0.239 \pm 0.001$
6	1000	$0.256 \pm 0.008$	$0.158 \pm 0.001$	$0.160 \pm 0.003$
7	3160	$0.226 \pm 0.005$	$0.146 \pm 0.002$	$0.156 \pm 0.003$
8	10000	$0.235 \pm 0.005$	$0.151 \pm 0.001$	$0.165 \pm 0.004$
9	31600	$0.195 \pm 0.006$	$0.133 \pm 0.002$	$0.145 \pm 0.006$
10	60000	$0.126 \pm 0.004$	$0.159 \pm 0.000$	$0.109 \pm 0.001$

The over-prediction is dramatic. At  $k = 6..9$  our form’s mean bias on the held-out cell sits in  $[+0.17, +0.21]$  (predictions  $\sim 20\%$  too high in log space across every held-out target from  $D = 1,000$  to  $D = 31,600$ ). Over the same range, Chinchilla’s MBE stays in  $[+0.02, +0.04]$  and Muennighoff’s in  $[+0.03, +0.07]$ . The over-prediction is consistent with the cross term doing exactly what the hypothesis predicts: extrapolating the small- $D$  overfitting penalty out to  $D$  values where overfitting is absent. The  $k = 10$  row is the bookend: when training also contains  $D = 60,000$ ’s neighbors (the  $D = 31,600$  cell etc.), the cross term has enough constraints to behave near the asymptote, our form’s RMSE drops to 0.126, and the bias collapses from +0.20 to +0.085.

**What the sweeps show.** Both questions admit clean answers from the data.

1. *Sweep A (contamination threshold).* Restricting training to  $D \geq 50$  keeps ours competitive with Muennighoff on the  $D = 60,000$  holdout (RMSE inside bootstrap CIs through  $k = 5-8$ , with ours winning cleanly at  $k = 6$ ). Adding  $D = 20$  lets Muennighoff edge ahead, and adding  $D = 10$  flips the comparison cleanly (ours  $0.126 \pm 0.004$  vs. Muennighoff  $0.109 \pm 0.001$ ). The contamination threshold sits between  $D = 20$  and  $D = 50$ .
2. *Sweep B (range of over-extrapolation).* With the smallest- $D$  cells fixed in training, ours’ held-out MBE is +0.17 to +0.21 on every held-out target from  $D = 1,000$  to  $D = 31,600$  (four orders of magnitude); Chinchilla and Muennighoff hold at  $[+0.02, +0.04]$  and  $[+0.03, +0.07]$  respectively. The over-prediction collapses only when training contains neighbors of the held-out cell ( $k = 10$ , where the bias drops to +0.085). The over-extrapolation is therefore wide, not asymptote-specific.

**Scope of validity.** Sweeps A and B together localize when our form’s cross term is a structural asset versus a structural liability: the cross-term parameters required to absorb in-sample overfitting at extreme small  $D$  do not decay sufficiently with  $D$  and contribute a positive residual at every other  $D$ . The form’s added expressiveness therefore translates into improved extrapolation only when fit on training subsets that exclude the extreme small- $D$  cells. We accordingly recommend excluding extreme small- $D$  cells from the training set when fitting our form to a grid that includes them; extending the form to remain well-behaved across the full  $D$  range (regularization on the cross-term coefficients, or a parametrization that decouples in-sample fit from extrapolation) is left to future work.

## N Fitted parameters

Point estimates of the eight free parameters ( $E, a, b, c, \alpha, \beta, \gamma, \delta$ ) for each domain, with bootstrap-CI half-widths from the protocol in Appendix F.

The coefficients ( $a, b, c$ ) span many orders of magnitude across rows because they are tightly coupled to the fitted exponents through the form  $a/N^\alpha + b/T^\beta + c N^\gamma/D^\delta$ : a small change in  $\alpha$  at  $N \sim 10^{10}$  is compensated by a  $10\times$  shift in  $a$ , and similarly for  $b, c$ . Marginal CIs on individual parameters are therefore misleading without joint contours; we report the point estimates as the fitter’s solution and rely on gray-cell shading to flag entries whose marginal CI half-width exceeds the value. Mapping the full bootstrap correlation matrix per dataset is left to future work; doing so would clarify how the form’s identifiability structure shifts between data-constrained grids (where the overfitting cross-term  $c N^\gamma/D^\delta$  is identified) and data-rich single-epoch grids (where it is degenerate along the manifold pinned only by  $\log c + \gamma \log N_0 - \delta \log D_0$  at any anchor  $(N_0, D_0)$ ), and would let downstream

Table 5: **Fitted parameters of Ours (Eq. (2)) on each dataset’s full-data fit.** One row per domain; one column per fitted parameter. Values are point estimates;  $\pm$  is the half-width of the 95% bootstrap CI over 200 resamples (robust to the skewed / multi-modal bootstrap distributions that show up around weakly-identified parameters in scaling-law forms). Gray cells are weakly identified – bootstrap CI half-width is at least as wide as the value, or the bootstrap degenerated to a single point; cross-dataset comparison of these cells is unsafe. Predictions remain reliable (see Tables 6 and 8); only the individual parameter values shuffle inside an equivalence class. Parameters  $a, b, c$  render in scientific notation;  $E, \alpha, \beta, \gamma, \delta$  are fixed-point.

Domain $\downarrow$	$E$	$a$	$\alpha$	$b$	$\beta$	$c$	$\gamma$	$\delta$
MNIST	0.070 $\pm$ 0.002	5.41e4 $\pm$ 2.60e4	1.448 $\pm$ 0.049	1.86e3 $\pm$ 1.93e4	1.226 $\pm$ 0.300	3.41e0 $\pm$ 1.04e-1	0.109 $\pm$ 0.002	0.584 $\pm$ 0.004
CIFAR-100	0.563 $\pm$ 0.107	5.85e2 $\pm$ 2.33e3	0.668 $\pm$ 0.136	3.45e6 $\pm$ 3.66e8	1.312 $\pm$ 0.376	6.33e3 $\pm$ 2.88e4	0.107 $\pm$ 0.061	1.223 $\pm$ 0.134
Darcy	0.005 $\pm$ 0.007	3.26e0 $\pm$ 3.55e1	0.384 $\pm$ 0.186	3.50e1 $\pm$ 4.59e1	0.667 $\pm$ 0.110	2.93e0 $\pm$ 2.12e-1	0.000 $\pm$ 0.000	0.679 $\pm$ 0.018
TinyStories	0.873 $\pm$ 0.122	1.31e2 $\pm$ 4.14e2	0.483 $\pm$ 0.111	2.95e3 $\pm$ 1.29e4	0.578 $\pm$ 0.094	7.75e1 $\pm$ 3.16e1	0.032 $\pm$ 0.022	0.480 $\pm$ 0.023
Chinchilla	0.038 $\pm$ 0.025	3.09e2 $\pm$ 1.72e2	0.422 $\pm$ 0.028	1.17e0 $\pm$ 3.86e-1	0.063 $\pm$ 0.011	4.76e9 $\pm$ 2.22e18	0.002 $\pm$ 0.013	1.184 $\pm$ 0.602
Muennighoff	2.114 $\pm$ 0.194	2.19e2 $\pm$ 2.27e2	0.391 $\pm$ 0.068	3.72e7 $\pm$ 5.34e8	0.929 $\pm$ 0.136	1.71e-1 $\pm$ 3.18e0	0.793 $\pm$ 0.531	0.852 $\pm$ 0.433
Gadre	2.064 $\pm$ 0.149	7.64e1 $\pm$ 4.27e1	0.334 $\pm$ 0.039	8.62e2 $\pm$ 2.26e3	0.420 $\pm$ 0.069	6.92e2 $\pm$ 3.89e7	2.679 $\pm$ 4.799	2.934 $\pm$ 4.415
Porian	0.001 $\pm$ 0.000	3.79e0 $\pm$ 0.00e0	0.115 $\pm$ 0.000	5.15e6 $\pm$ 0.00e0	0.832 $\pm$ 0.000	1.10e0 $\pm$ 0.00e0	34.357 $\pm$ 0.000	45.630 $\pm$ 0.000
Farseer	0.315 $\pm$ 0.157	2.59e0 $\pm$ 2.61e-1	0.135 $\pm$ 0.009	4.54e2 $\pm$ 3.98e4	0.464 $\pm$ 0.115	6.42e-2 $\pm$ 8.50e-2	0.199 $\pm$ 0.015	0.202 $\pm$ 0.021

uses such as the cost-allocation analysis of Appendix K propagate joint uncertainty through derived quantities like  $(N^*, D^*, T^*)$  rather than relying on marginal CIs.

**Boundary fits.** On Darcy, the cross-term exponent identifies  $\gamma = 0$  robustly across bootstrap resamples (a stable boundary value, not a wide marginal interval), so the term reduces to a pure  $D$ -axis correction  $c/D^\delta$  with no  $N$  dependence;  $\delta = 0.679$  remains identified and continues to contribute to the fit. We read this as the absence of capacity-driven overfitting in the regime sampled, consistent with Darcy’s smooth elliptic-PDE structure and FNO’s strong Fourier inductive bias against memorizing individual training pairs.

## O Full experiment results and ablations

The three tables below report each form’s RMSE on each dataset under four protocols: high- $C$  and high- $D$  holdouts (Table 6, both defined in §3.2); 5-fold cross-validation (Table 7); and in-sample, the full-dataset fit with no holdout (Table 8). Forms above the horizontal rule are external baselines fit to the loss surface; below the rule, our form (Eq. (2)) and four ablations of it. Datasets to the left of the vertical rule are from our experiments (Section 3); to the right are published grids on which we refit each form. The “extended” variant (12-parameter exploratory form, Appendix P) is shown in gray and excluded from the per-column rankings. All three tables include Darcy and Farseer columns; the per-experiment unit ‘ $\pm$  std’ on each cell denotes either bootstrap CI (Tables 6, 8) or cross-fold std over 5 folds (Table 7).

**In-sample fit.** Our form (or one of its wrapper-choice and single-exponent siblings) attains the lowest in-sample RMSE on every column of Table 8. We report this metric for completeness because it is the headline metric in much of the scaling-law literature, but it is deliberately not the headline of this paper: a form with three additional free parameters mechanically fits its training set better than a strictly-additive baseline, and the practical use of a fitted scaling law (cost allocation, recipe transfer to a larger budget, predictions at unobserved  $(N, D)$  design points) is always an extrapolation, never an interpolation. The held-out columns of Tables 6 and 7 are the metric we ask the form to be judged on.

**Random 5-fold cross validation.** Random 5-fold tests near-interpolation: each held-out cell is bracketed by training cells on every axis. The family wins eight of nine columns (Table 7); the only loss is Chinchilla, where the native Chinchilla form is best by 0.012 log-RMSE. Random 5-fold and in-sample rankings agree closely for every form, while axis-holdout rankings open up much larger gaps. Our form’s advantage under axis holdouts is therefore a genuine extrapolation gain, not a fit-flexibility artifact that contracts once a stricter holdout is imposed.

**Per-component ablations.** The single most consequential component of the form is the overfitting cross term  $cN^\gamma/D^\delta$ : removing it inflates held-out RMSE by 5–13 $\times$  on MNIST and CIFAR-100

Table 6: **high- $C$  / high- $D$  holdout**. Held-out RMSE and MBE (log space) under the high- $C$  and high- $D$  holdout protocols (defined in §3.2). RMSE: lower is better. MBE: closer to zero is better – ranked by |value|. Per column, within each metric pane, **best** and **second best** are highlighted, excluding the grayed “extended” row. Error bars: bootstrap  $\pm$  std over 200 resamples.

high- $C$ holdout									
Form $\downarrow$	MNIST	CIFAR-100	Darcy	TinyStories	Chinchilla	Muennighoff	Gadre	Porian	Farseeer
<i>RMSE (log space)</i>									
Chinchilla [26]	0.332 $\pm$ 0.001	0.156 $\pm$ 0.011	0.322 $\pm$ 0.027	0.173 $\pm$ 0.023	0.024 $\pm$ 0.003	0.092 $\pm$ 0.013	0.038 $\pm$ 0.012	0.100 $\pm$ 0.014	0.028 $\pm$ 0.002
Muennighoff [36]	0.333 $\pm$ 0.001	0.151 $\pm$ 0.008	0.181 $\pm$ 0.009	<b>0.095 <math>\pm</math> 0.012</b>	0.024 $\pm$ 0.003	0.087 $\pm$ 0.008	0.038 $\pm$ 0.012	0.100 $\pm$ 0.015	0.028 $\pm$ 0.001
M4 ( $N$ -axis) [1]	1.115 $\pm$ 0.014	0.607 $\pm$ 0.026	1.311 $\pm$ 0.103	0.626 $\pm$ 0.067	0.070 $\pm$ 0.008	0.177 $\pm$ 0.027	0.066 $\pm$ 0.032	0.376 $\pm$ 0.035	0.100 $\pm$ 0.005
M4 ( $D$ -axis) [1]	0.295 $\pm$ 0.003	0.126 $\pm$ 0.022	0.404 $\pm$ 0.026	0.337 $\pm$ 0.030	0.067 $\pm$ 0.006	0.094 $\pm$ 0.013	0.119 $\pm$ 0.032	0.114 $\pm$ 0.014	0.111 $\pm$ 0.006
BNSL $k=1$ [12]	0.309 $\pm$ 0.002	0.116 $\pm$ 0.000	0.399 $\pm$ 0.000	0.322 $\pm$ 0.000	0.062 $\pm$ 0.004	0.094 $\pm$ 0.013	0.105 $\pm$ 0.030	37.261 $\pm$ 1.580	0.111 $\pm$ 0.006
BNSL $k=2$ [12]	0.309 $\pm$ 0.002	0.117 $\pm$ 0.000	0.404 $\pm$ 0.000	0.324 $\pm$ 0.034	0.067 $\pm$ 0.006	0.094 $\pm$ 0.012	0.105 $\pm$ 0.029	37.261 $\pm$ 1.265	0.111 $\pm$ 0.006
Farseeer [29]	1.389 $\pm$ 0.010	0.607 $\pm$ 0.025	0.375 $\pm$ 0.071	<b>0.119 <math>\pm</math> 0.009</b>	0.030 $\pm$ 0.002	0.108 $\pm$ 0.013	0.053 $\pm$ 0.009	0.069 $\pm$ 0.012	0.020 $\pm$ 0.002
Ours (Eq. (2))	0.127 $\pm$ 0.001	0.081 $\pm$ 0.010	0.168 $\pm$ 0.016	0.184 $\pm$ 0.021	0.007 $\pm$ 0.004	0.059 $\pm$ 0.011	<b>0.014 <math>\pm</math> 0.011</b>	<b>0.063 <math>\pm</math> 0.012</b>	0.008 $\pm$ 0.001
Ours, no wrapper	0.173 $\pm$ 0.001	0.154 $\pm$ 0.011	<b>0.148 <math>\pm</math> 0.011</b>	0.121 $\pm$ 0.016	0.008 $\pm$ 0.004	0.057 $\pm$ 0.009	0.037 $\pm$ 0.016	0.100 $\pm$ 0.014	0.010 $\pm$ 0.001
Ours, no overfitting term	0.868 $\pm$ 0.008	0.607 $\pm$ 0.075	0.375 $\pm$ 0.048	0.251 $\pm$ 0.035	0.022 $\pm$ 0.004	0.114 $\pm$ 0.015	0.016 $\pm$ 0.012	<b>0.063 <math>\pm</math> 0.012</b>	0.024 $\pm$ 0.001
Ours, $1-e^{-h}$ wrapper	<b>0.123 <math>\pm</math> 0.001</b>	<b>0.080 <math>\pm</math> 0.011</b>	0.161 $\pm$ 0.014	0.160 $\pm$ 0.018	0.007 $\pm$ 0.003	0.059 $\pm$ 0.012	0.025 $\pm$ 0.016	0.075 $\pm$ 0.013	0.010 $\pm$ 0.001
Ours, single-exp ( $N/D$ ) $^\gamma$	1.137 $\pm$ 0.006	0.366 $\pm$ 0.112	0.304 $\pm$ 0.027	0.204 $\pm$ 0.027	<b>0.004 <math>\pm</math> 0.002</b>	<b>0.050 <math>\pm</math> 0.006</b>	<b>0.014 <math>\pm</math> 0.014</b>	<b>0.063 <math>\pm</math> 0.013</b>	<b>0.006 <math>\pm</math> 0.001</b>
Ours, extended (12-param)	0.070 $\pm$ 0.003	0.055 $\pm$ 0.007	0.131 $\pm$ 0.009	0.035 $\pm$ 0.006	0.005 $\pm$ 0.002	0.055 $\pm$ 0.005	0.023 $\pm$ 0.012	0.034 $\pm$ 0.007	0.009 $\pm$ 0.001
<i>MBE (log space)</i>									
Chinchilla [26]	-0.278 $\pm$ 0.002	<b>0.003 <math>\pm</math> 0.024</b>	0.302 $\pm$ 0.030	0.163 $\pm$ 0.024	0.013 $\pm$ 0.004	0.069 $\pm$ 0.015	-0.032 $\pm$ 0.015	-0.087 $\pm$ 0.013	0.026 $\pm$ 0.002
Muennighoff [36]	-0.280 $\pm$ 0.002	-0.052 $\pm$ 0.028	<b>-0.061 <math>\pm</math> 0.016</b>	<b>-0.024 <math>\pm</math> 0.030</b>	0.013 $\pm$ 0.004	0.037 $\pm$ 0.012	-0.032 $\pm$ 0.014	-0.087 $\pm$ 0.015	0.026 $\pm$ 0.001
M4 ( $N$ -axis) [1]	0.647 $\pm$ 0.025	0.011 $\pm$ 0.093	1.265 $\pm$ 0.109	0.609 $\pm$ 0.069	0.056 $\pm$ 0.013	0.148 $\pm$ 0.031	0.064 $\pm$ 0.037	0.374 $\pm$ 0.035	0.099 $\pm$ 0.005
M4 ( $D$ -axis) [1]	-0.251 $\pm$ 0.003	0.058 $\pm$ 0.018	0.392 $\pm$ 0.027	0.327 $\pm$ 0.030	0.063 $\pm$ 0.007	0.069 $\pm$ 0.014	0.100 $\pm$ 0.050	0.109 $\pm$ 0.015	0.107 $\pm$ 0.006
BNSL $k=1$ [12]	-0.261 $\pm$ 0.002	0.057 $\pm$ 0.000	0.381 $\pm$ 0.000	0.313 $\pm$ 0.000	0.053 $\pm$ 0.007	0.069 $\pm$ 0.014	0.080 $\pm$ 0.054	-19.677 $\pm$ 1.628	0.107 $\pm$ 0.006
BNSL $k=2$ [12]	-0.261 $\pm$ 0.002	0.058 $\pm$ 0.000	0.386 $\pm$ 0.000	0.315 $\pm$ 0.034	0.063 $\pm$ 0.007	0.069 $\pm$ 0.013	0.080 $\pm$ 0.055	-19.676 $\pm$ 1.360	0.107 $\pm$ 0.006
Farseeer [29]	1.064 $\pm$ 0.015	0.012 $\pm$ 0.083	-0.197 $\pm$ 0.161	<b>0.039 <math>\pm</math> 0.024</b>	-0.026 $\pm$ 0.002	0.050 $\pm$ 0.024	-0.046 $\pm$ 0.011	<b>-0.056 <math>\pm</math> 0.013</b>	0.015 $\pm$ 0.004
Ours (Eq. (2))	-0.033 $\pm$ 0.004	-0.036 $\pm$ 0.010	-0.107 $\pm$ 0.019	-0.169 $\pm$ 0.021	-0.004 $\pm$ 0.005	0.029 $\pm$ 0.008	-0.010 $\pm$ 0.011	-0.060 $\pm$ 0.011	0.007 $\pm$ 0.001
Ours, no wrapper	-0.062 $\pm$ 0.003	-0.065 $\pm$ 0.045	-0.071 $\pm$ 0.021	-0.109 $\pm$ 0.016	<b>-0.001 <math>\pm</math> 0.005</b>	<b>0.021 <math>\pm</math> 0.010</b>	-0.029 $\pm$ 0.014	-0.087 $\pm$ 0.013	0.008 $\pm$ 0.001
Ours, no overfitting term	-0.308 $\pm$ 0.023	-0.018 $\pm$ 0.171	-0.192 $\pm$ 0.116	-0.202 $\pm$ 0.044	0.012 $\pm$ 0.004	0.059 $\pm$ 0.027	-0.013 $\pm$ 0.014	-0.060 $\pm$ 0.012	0.023 $\pm$ 0.001
Ours, $1-e^{-h}$ wrapper	<b>-0.030 <math>\pm</math> 0.003</b>	-0.036 $\pm$ 0.014	-0.094 $\pm$ 0.019	-0.147 $\pm$ 0.018	-0.003 $\pm$ 0.004	0.026 $\pm$ 0.009	-0.019 $\pm$ 0.015	-0.071 $\pm$ 0.012	0.008 $\pm$ 0.001
Ours, single-exp ( $N/D$ ) $^\gamma$	1.005 $\pm$ 0.005	0.293 $\pm$ 0.096	0.197 $\pm$ 0.034	-0.174 $\pm$ 0.027	<b>0.001 <math>\pm</math> 0.002</b>	<b>0.026 <math>\pm</math> 0.007</b>	<b>-0.009 <math>\pm</math> 0.012</b>	-0.060 $\pm$ 0.012	<b>0.004 <math>\pm</math> 0.001</b>
Ours, extended (12-param)	-0.012 $\pm$ 0.004	-0.002 $\pm$ 0.011	0.080 $\pm$ 0.020	0.011 $\pm$ 0.013	-0.001 $\pm$ 0.002	0.023 $\pm$ 0.012	-0.017 $\pm$ 0.011	-0.033 $\pm$ 0.007	0.008 $\pm$ 0.001
high- $D$ holdout									
Form $\downarrow$	MNIST	CIFAR-100	Darcy	TinyStories	Chinchilla	Muennighoff	Gadre	Porian	Farseeer
<i>RMSE (log space)</i>									
Chinchilla [26]	0.123 $\pm$ 0.001	0.182 $\pm$ 0.019	0.388 $\pm$ 0.034	0.057 $\pm$ 0.015	0.028 $\pm$ 0.004	0.112 $\pm$ 0.015	0.038 $\pm$ 0.012	0.115 $\pm$ 0.017	0.017 $\pm$ 0.001
Muennighoff [36]	0.122 $\pm$ 0.005	0.171 $\pm$ 0.031	0.187 $\pm$ 0.013	0.095 $\pm$ 0.008	0.028 $\pm$ 0.004	0.079 $\pm$ 0.010	0.038 $\pm$ 0.012	0.115 $\pm$ 0.017	0.017 $\pm$ 0.001
M4 ( $N$ -axis) [1]	1.914 $\pm$ 0.016	0.886 $\pm$ 0.145	1.234 $\pm$ 0.076	0.546 $\pm$ 0.042	0.085 $\pm$ 0.005	0.189 $\pm$ 0.026	0.066 $\pm$ 0.032	0.321 $\pm$ 0.039	0.080 $\pm$ 0.004
M4 ( $D$ -axis) [1]	0.192 $\pm$ 0.003	0.265 $\pm$ 0.014	0.361 $\pm$ 0.019	0.223 $\pm$ 0.016	0.036 $\pm$ 0.005	0.101 $\pm$ 0.009	0.119 $\pm$ 0.032	0.079 $\pm$ 0.006	0.070 $\pm$ 0.005
BNSL $k=1$ [12]	0.171 $\pm$ 0.001	0.322 $\pm$ 0.022	66.018 $\pm$ 0.000	69.620 $\pm$ 0.000	0.042 $\pm$ 0.005	0.122 $\pm$ 0.012	0.105 $\pm$ 0.030	0.139 $\pm$ 31.292	0.070 $\pm$ 0.005
BNSL $k=2$ [12]	0.169 $\pm$ 20.568	0.332 $\pm$ 25.942	66.018 $\pm$ 0.000	69.620 $\pm$ 0.000	0.036 $\pm$ 0.005	0.103 $\pm$ 0.009	0.105 $\pm$ 0.029	0.139 $\pm$ 32.354	0.070 $\pm$ 0.005
Farseeer [29]	1.490 $\pm$ 0.016	0.899 $\pm$ 0.152	0.462 $\pm$ 0.054	0.060 $\pm$ 0.026	0.012 $\pm$ 0.002	0.113 $\pm$ 0.023	0.053 $\pm$ 0.009	0.100 $\pm$ 0.011	0.041 $\pm$ 0.002
Ours (Eq. (2))	0.137 $\pm$ 0.004	<b>0.069 <math>\pm</math> 0.016</b>	<b>0.170 <math>\pm</math> 0.014</b>	<b>0.053 <math>\pm</math> 0.014</b>	0.010 $\pm$ 0.005	0.044 $\pm$ 0.012	<b>0.014 <math>\pm</math> 0.011</b>	<b>0.033 <math>\pm</math> 0.003</b>	<b>0.005 <math>\pm</math> 0.000</b>
Ours, no wrapper	<b>0.097 <math>\pm</math> 0.001</b>	0.150 $\pm$ 0.026	0.184 $\pm$ 0.011	0.070 $\pm$ 0.011	<b>0.004 <math>\pm</math> 0.003</b>	0.041 $\pm$ 0.008	0.037 $\pm$ 0.016	0.115 $\pm$ 0.017	0.006 $\pm$ 0.000
Ours, no overfitting term	1.270 $\pm$ 0.014	0.874 $\pm$ 0.152	0.464 $\pm$ 0.048	0.061 $\pm$ 0.017	0.027 $\pm$ 0.006	0.120 $\pm$ 0.025	0.016 $\pm$ 0.012	<b>0.033 <math>\pm</math> 0.003</b>	0.014 $\pm$ 0.001
Ours, $1-e^{-h}$ wrapper	0.104 $\pm$ 0.002	0.131 $\pm$ 0.026	0.180 $\pm$ 0.013	0.056 $\pm$ 0.013	0.007 $\pm$ 0.003	0.042 $\pm$ 0.011	0.025 $\pm$ 0.016	0.057 $\pm$ 0.009	0.006 $\pm$ 0.000
Ours, single-exp ( $N/D$ ) $^\gamma$	0.755 $\pm$ 0.012	0.381 $\pm$ 0.113	0.278 $\pm$ 0.049	0.142 $\pm$ 0.025	0.013 $\pm$ 0.003	<b>0.040 <math>\pm</math> 0.007</b>	<b>0.014 <math>\pm</math> 0.014</b>	<b>0.033 <math>\pm</math> 0.003</b>	<b>0.005 <math>\pm</math> 0.000</b>
Ours, extended (12-param)	0.096 $\pm$ 0.002	0.140 $\pm$ 0.019	0.133 $\pm$ 0.014	0.085 $\pm$ 0.009	0.006 $\pm$ 0.001	0.037 $\pm$ 0.006	0.023 $\pm$ 0.012	0.048 $\pm$ 0.005	0.005 $\pm$ 0.000
<i>MBE (log space)</i>									
Chinchilla [26]	<b>0.003 <math>\pm</math> 0.004</b>	0.036 $\pm$ 0.031	-0.249 $\pm$ 0.054	-0.006 $\pm$ 0.026	0.025 $\pm$ 0.004	-0.059 $\pm$ 0.042	-0.032 $\pm$ 0.015	-0.108 $\pm$ 0.017	-0.008 $\pm$ 0.002
Muennighoff [36]	0.069 $\pm$ 0.005	0.047 $\pm$ 0.032	<b>-0.033 <math>\pm</math> 0.012</b>	-0.045 $\pm$ 0.011	0.025 $\pm$ 0.004	0.029 $\pm$ 0.019	-0.032 $\pm$ 0.014	-0.108 $\pm$ 0.017	-0.008 $\pm$ 0.002
M4 ( $N$ -axis) [1]	1.906 $\pm$ 0.016	0.859 $\pm$ 0.152	1.192 $\pm$ 0.076	0.540 $\pm$ 0.041	0.084 $\pm$ 0.005	0.182 $\pm$ 0.025	0.064 $\pm$ 0.037	0.311 $\pm$ 0.038	0.078 $\pm$ 0.004
M4 ( $D$ -axis) [1]	0.087 $\pm$ 0.007	-0.103 $\pm$ 0.046	-0.093 $\pm$ 0.063	0.072 $\pm$ 0.050	<b>-0.001 <math>\pm</math> 0.019</b>	-0.032 $\pm$ 0.036	0.100 $\pm$ 0.050	<b>-0.005 <math>\pm</math> 0.028</b>	-0.023 $\pm$ 0.014
BNSL $k=1$ [12]	-0.035 $\pm$ 0.005	-0.211 $\pm$ 0.035	-66.017 $\pm$ 0.000	-69.620 $\pm$ 0.000	-0.023 $\pm$ 0.010	-0.074 $\pm$ 0.026	0.080 $\pm$ 0.054	-0.115 $\pm$ 31.182	-0.024 $\pm$ 0.014
BNSL $k=2$ [12]	-0.025 $\pm$ 20.608	-0.226 $\pm$ 25.981	-66.017 $\pm$ 0.000	-69.620 $\pm$ 0.000	<b>-0.001 <math>\pm</math> 0.018</b>	-0.038 $\pm$ 0.035	0.080 $\pm$ 0.055	-0.115 $\pm$ 32.167	-0.024 $\pm$ 0.013
Farseeer [29]	1.467 $\pm$ 0.016	0.878 $\pm$ 0.160	0.403 $\pm$ 0.043	0.008 $\pm$ 0.014	-0.004 $\pm$ 0.004	0.107 $\pm$ 0.022	-0.046 $\pm$ 0.011	-0.093 $\pm$ 0.012	-0.036 $\pm$ 0.002
Ours (Eq. (2))	0.083 $\pm$ 0.006	<b>-0.009 <math>\pm</math> 0.025</b>	-0.096 $\pm$ 0.018	<b>-0.004 <math>\pm</math> 0.013</b>	-0.008 $\pm$ 0.006	0.014 $\pm$ 0.020	-0.010 $\pm$ 0.011	-0.014 $\pm$ 0.008	<b>-0.001 <math>\pm</math> 0.001</b>
Ours, no wrapper	0.042 $\pm$ 0.002	0.028 $\pm$ 0.032	-0.133 $\pm$ 0.017	-0.049 $\pm$ 0.010	<b>-0.001 <math>\pm</math> 0.003</b>	<b>0.003 <math>\pm</math> 0.019</b>	-0.029 $\pm$ 0.014	-0.108 $\pm$ 0.017	<b>-0.001 <math>\pm</math> 0.001</b>
Ours, no overfitting term	1.223 $\pm$ 0.015	0.857 $\pm$ 0.160	0.411 $\pm$ 0.039	0.023 $\pm$ 0.018	0.024 $\pm$ 0.006	0.112			

Table 7: **Random 5-fold Cross Validation.** Held-out RMSE and MBE (log space) under 5-fold random cross-validation. Each fold holds out a uniform-random 20% of cells; the reported value is the cross-fold mean. RMSE: lower is better. MBE: closer to zero is better – ranked by  $|\text{value}|$ . Per column, within each metric pane, **best** and **second best** are highlighted, excluding the grayed “extended” row. Error bars:  $\pm$  std across the 5 folds.

Random 5-fold Cross Validation									
Form ↓	MNIST	CIFAR-100	Darcy	TinyStories	Chinchilla	Muennighoff	Gadre	Porian	Farseer
<i>RMSE (log space)</i>									
Chinchilla [26]	0.230 ± 0.005	0.129 ± 0.012	0.273 ± 0.030	0.138 ± 0.019	<b>0.017 ± 0.009</b>	0.204 ± 0.055	0.027 ± 0.015	0.064 ± 0.011	0.011 ± 0.001
Muennighoff [36]	0.204 ± 0.004	0.120 ± 0.017	0.129 ± 0.019	0.092 ± 0.004	<b>0.017 ± 0.009</b>	0.177 ± 0.052	0.027 ± 0.015	0.064 ± 0.011	0.011 ± 0.001
M4 (N-axis) [1]	0.971 ± 0.016	0.538 ± 0.019	0.826 ± 0.034	0.398 ± 0.025	0.100 ± 0.035	0.278 ± 0.058	0.093 ± 0.030	0.315 ± 0.029	0.060 ± 0.002
M4 (D-axis) [1]	0.224 ± 0.003	0.144 ± 0.045	0.302 ± 0.031	0.200 ± 0.025	0.064 ± 0.004	0.215 ± 0.040	0.094 ± 0.042	0.099 ± 0.018	0.064 ± 0.002
BNSL $k=1$ [12]	0.224 ± 0.004	0.149 ± 0.048	0.304 ± 0.029	0.198 ± 0.014	4.051 ± 8.893	0.214 ± 0.040	0.093 ± 0.041	2.954 ± 6.367	0.064 ± 0.002
BNSL $k=2$ [12]	0.223 ± 0.003	0.149 ± 0.048	0.304 ± 0.028	0.197 ± 0.014	0.064 ± 0.004	0.214 ± 0.040	0.093 ± 0.041	0.105 ± 0.014	0.064 ± 0.002
Farseer [29]	0.781 ± 0.008	0.541 ± 0.024	0.484 ± 0.030	0.262 ± 0.023	0.022 ± 0.014	0.242 ± 0.060	0.028 ± 0.018	0.058 ± 0.009	0.018 ± 0.002
<b>Ours (Eq. (2))</b>	0.130 ± 0.002	<b>0.062 ± 0.008</b>	<b>0.118 ± 0.011</b>	0.076 ± 0.016	0.029 ± 0.037	<b>0.130 ± 0.031</b>	0.021 ± 0.019	0.048 ± 0.007	<b>0.006 ± 0.001</b>
Ours, no wrapper	0.137 ± 0.020	0.118 ± 0.011	0.129 ± 0.009	0.078 ± 0.011	0.062 ± 0.110	0.151 ± 0.027	0.025 ± 0.018	0.064 ± 0.011	<b>0.006 ± 0.001</b>
Ours, no overfitting term	0.751 ± 0.014	0.539 ± 0.019	0.485 ± 0.019	0.249 ± 0.008	0.018 ± 0.010	0.242 ± 0.062	0.020 ± 0.011	0.048 ± 0.007	0.010 ± 0.001
Ours, $1-e^{-h}$ wrapper	<b>0.110 ± 0.002</b>	0.069 ± 0.009	0.123 ± 0.010	<b>0.075 ± 0.015</b>	0.031 ± 0.042	0.137 ± 0.029	0.024 ± 0.021	<b>0.047 ± 0.005</b>	<b>0.006 ± 0.001</b>
Ours, single-exp ( $N/D$ ) <sup>γ</sup>	0.482 ± 0.016	0.279 ± 0.030	0.280 ± 0.018	0.125 ± 0.013	0.029 ± 0.037	<b>0.130 ± 0.030</b>	<b>0.015 ± 0.010</b>	0.048 ± 0.007	<b>0.006 ± 0.001</b>
Ours, extended (12-param)	0.080 ± 0.004	0.061 ± 0.016	0.073 ± 0.009	0.039 ± 0.001	0.031 ± 0.042	0.137 ± 0.037	0.017 ± 0.011	0.036 ± 0.006	0.005 ± 0.001
<i>MBE (log space)</i>									
Chinchilla [26]	-0.063 ± 0.006	-0.018 ± 0.020	-0.058 ± 0.040	-0.018 ± 0.025	<b>-0.001 ± 0.002</b>	-0.069 ± 0.041	-0.005 ± 0.013	0.003 ± 0.007	<b>0.000 ± 0.001</b>
Muennighoff [36]	-0.047 ± 0.006	-0.021 ± 0.008	<b>-0.003 ± 0.019</b>	<b>-0.002 ± 0.015</b>	<b>-0.001 ± 0.002</b>	-0.048 ± 0.038	-0.005 ± 0.013	0.003 ± 0.007	<b>0.000 ± 0.001</b>
M4 (N-axis) [1]	0.137 ± 0.033	-0.057 ± 0.108	-0.083 ± 0.073	-0.023 ± 0.044	-0.019 ± 0.015	-0.084 ± 0.047	-0.015 ± 0.051	-0.089 ± 0.040	-0.007 ± 0.008
M4 (D-axis) [1]	-0.056 ± 0.005	-0.022 ± 0.036	-0.062 ± 0.059	-0.034 ± 0.011	-0.010 ± 0.009	-0.072 ± 0.039	-0.008 ± 0.065	-0.015 ± 0.023	-0.005 ± 0.007
BNSL $k=1$ [12]	-0.055 ± 0.005	-0.025 ± 0.037	-0.062 ± 0.058	-0.031 ± 0.011	-1.147 ± 2.546	-0.071 ± 0.040	-0.008 ± 0.058	-0.587 ± 1.316	-0.005 ± 0.007
BNSL $k=2$ [12]	-0.053 ± 0.006	-0.026 ± 0.037	-0.062 ± 0.058	-0.030 ± 0.011	-0.010 ± 0.009	-0.071 ± 0.039	-0.008 ± 0.058	-0.003 ± 0.026	-0.005 ± 0.007
Farseer [29]	0.138 ± 0.014	-0.044 ± 0.103	-0.109 ± 0.058	-0.088 ± 0.036	-0.002 ± 0.003	-0.067 ± 0.041	-0.004 ± 0.013	<b>-0.002 ± 0.010</b>	<b>-0.000 ± 0.001</b>
<b>Ours (Eq. (2))</b>	-0.027 ± 0.004	-0.001 ± 0.009	-0.013 ± 0.018	-0.010 ± 0.018	0.002 ± 0.007	<b>-0.010 ± 0.038</b>	0.002 ± 0.012	-0.005 ± 0.006	<b>0.000 ± 0.000</b>
Ours, no wrapper	<b>-0.016 ± 0.008</b>	-0.027 ± 0.006	-0.017 ± 0.021	-0.006 ± 0.016	0.006 ± 0.017	-0.022 ± 0.036	0.002 ± 0.014	0.003 ± 0.007	<b>0.000 ± 0.001</b>
Ours, no overfitting term	0.154 ± 0.013	-0.057 ± 0.108	-0.088 ± 0.047	-0.032 ± 0.039	<b>-0.001 ± 0.002</b>	-0.072 ± 0.040	-0.003 ± 0.009	-0.005 ± 0.006	<b>0.000 ± 0.001</b>
Ours, $1-e^{-h}$ wrapper	-0.019 ± 0.003	<b>0.000 ± 0.009</b>	-0.015 ± 0.019	-0.008 ± 0.017	0.002 ± 0.007	-0.011 ± 0.041	0.002 ± 0.013	-0.003 ± 0.005	<b>0.000 ± 0.001</b>
Ours, single-exp ( $N/D$ ) <sup>γ</sup>	0.060 ± 0.014	-0.081 ± 0.043	0.005 ± 0.031	<b>0.001 ± 0.026</b>	0.002 ± 0.006	<b>-0.010 ± 0.038</b>	<b>-0.001 ± 0.006</b>	-0.005 ± 0.006	<b>0.000 ± 0.000</b>
Ours, extended (12-param)	-0.009 ± 0.002	0.005 ± 0.015	0.003 ± 0.013	0.001 ± 0.003	0.002 ± 0.007	-0.001 ± 0.033	0.001 ± 0.008	-0.002 ± 0.007	0.000 ± 0.001

**Decomposing the LLM-grid wins.** On the five LLM grids under high- $C$ , the wins partition cleanly between the two structural extensions. *Removing the cross term hurts* on Chinchilla, Muennighoff, and Farseer (RMSE inflates by 2–7 $\times$ , recovering Chinchilla-comparable performance), while the wrapper effect is small or zero on these grids. *Removing the wrapper hurts* on Gadre and Porian (the cross term contributes essentially nothing here; wrapper removal recovers the Chinchilla baseline within rounding). The partition is stable across protocols on the cleanest cases: Porian’s cross-term effect is negligible on every protocol (high- $C$ , high- $D$ , 5-fold all show 0.063, 0.033, 0.048 for both ours and no-overfit), and Muennighoff’s wrapper effect stays under  $0.6\sigma$  on every protocol while its cross-term effect spans 0.055 to 0.112. Chinchilla and Farseer track Muennighoff under high- $C$  and high- $D$  but get noisier under 5-fold. Either structural extension individually beats Chinchilla on a subset of these grids; both together yield the 5/5 sweep. Functionally, the cross term picks up joint  $(N, D)$  residual structure that an additive  $a/N^\alpha + b/T^\beta$  form cannot represent, while the wrapper picks up the saturating approach to the irreducible loss that an additive form bounds linearly; on each grid, whichever of these is the dominant unmodeled component in additive baselines is the load-bearing piece of our form.

Table 8: **In-Sample**. In-sample training RMSE and MBE (log space) under the full-data fit. Each form is fit on every observed cell. RMSE: lower is better. MBE: closer to zero is better – ranked by |value|. Per column, within each metric pane, **best** and **second best** are highlighted, excluding the grayed “extended” row. Error bars: bootstrap  $\pm$  std over 200 resamples of the training set.

In-Sample									
Form $\downarrow$	MNIST	CIFAR-100	Darcy	TinyStories	Chinchilla	Muennighoff	Gadre	Porian	Farseer
<i>Training RMSE (log space)</i>									
Chinchilla [26]	0.230 $\pm$ 0.000	0.122 $\pm$ 0.003	0.271 $\pm$ 0.005	0.136 $\pm$ 0.002	0.018 $\pm$ 0.002	0.208 $\pm$ 0.003	0.023 $\pm$ 0.006	0.061 $\pm$ 0.003	0.011 $\pm$ 0.000
Muennighoff [36]	0.202 $\pm$ 0.000	0.116 $\pm$ 0.005	0.128 $\pm$ 0.002	0.090 $\pm$ 0.002	0.018 $\pm$ 0.002	0.179 $\pm$ 0.004	0.023 $\pm$ 0.006	0.061 $\pm$ 0.004	0.011 $\pm$ 0.000
M4 ( <i>N</i> -axis) [1]	0.971 $\pm$ 0.004	0.533 $\pm$ 0.021	0.821 $\pm$ 0.008	0.394 $\pm$ 0.009	0.104 $\pm$ 0.001	0.280 $\pm$ 0.005	0.091 $\pm$ 0.004	0.313 $\pm$ 0.011	0.060 $\pm$ 0.000
M4 ( <i>D</i> -axis) [1]	0.224 $\pm$ 0.001	0.144 $\pm$ 0.006	0.301 $\pm$ 0.004	0.200 $\pm$ 0.004	0.064 $\pm$ 0.001	0.217 $\pm$ 0.006	0.087 $\pm$ 0.004	0.099 $\pm$ 0.001	0.064 $\pm$ 0.000
BNSL <i>k</i> =1 [12]	0.224 $\pm$ 0.000	0.149 $\pm$ 0.000	0.304 $\pm$ 0.003	0.194 $\pm$ 0.000	0.061 $\pm$ 2.766	0.216 $\pm$ 0.006	0.087 $\pm$ 0.007	0.104 $\pm$ 0.002	0.064 $\pm$ 0.000
BNSL <i>k</i> =2 [12]	0.224 $\pm$ 0.000	0.149 $\pm$ 0.000	0.303 $\pm$ 0.000	0.194 $\pm$ 0.000	0.063 $\pm$ 0.003	0.216 $\pm$ 0.006	0.087 $\pm$ 0.005	0.103 $\pm$ 2.317	0.064 $\pm$ 0.000
Farseer [29]	0.779 $\pm$ 0.002	0.533 $\pm$ 0.000	0.481 $\pm$ 0.012	0.261 $\pm$ 0.011	0.015 $\pm$ 0.001	0.246 $\pm$ 0.002	0.029 $\pm$ 0.002	0.055 $\pm$ 0.003	0.018 $\pm$ 0.000
<b>Ours (Eq. (2))</b>	0.129 $\pm$ 0.001	<b>0.060 <math>\pm</math> 0.002</b>	<b>0.116 <math>\pm</math> 0.003</b>	0.076 $\pm$ 0.002	<b>0.013 <math>\pm</math> 0.004</b>	<b>0.124 <math>\pm</math> 0.008</b>	<b>0.012 <math>\pm</math> 0.011</b>	0.047 $\pm$ 0.000	<b>0.006 <math>\pm</math> 0.000</b>
Ours, no wrapper	0.128 $\pm$ 0.000	0.112 $\pm$ 0.005	0.127 $\pm$ 0.002	0.077 $\pm$ 0.001	0.014 $\pm$ 0.012	0.141 $\pm$ 0.011	0.015 $\pm$ 0.021	0.061 $\pm$ 0.003	<b>0.006 <math>\pm</math> 0.000</b>
Ours, no overfitting term	0.750 $\pm$ 0.002	0.532 $\pm$ 0.022	0.483 $\pm$ 0.010	0.246 $\pm$ 0.005	0.019 $\pm$ 0.002	0.247 $\pm$ 0.003	0.017 $\pm$ 0.003	0.047 $\pm$ 0.001	0.010 $\pm$ 0.000
Ours, $1-e^{-h}$ wrapper	<b>0.110 <math>\pm</math> 0.000</b>	0.065 $\pm$ 0.002	0.121 $\pm$ 0.003	<b>0.074 <math>\pm</math> 0.001</b>	<b>0.013 <math>\pm</math> 0.006</b>	0.129 $\pm$ 0.008	0.013 $\pm$ 0.011	<b>0.046 <math>\pm</math> 0.001</b>	<b>0.006 <math>\pm</math> 0.000</b>
Ours, single-exp ( $N/D$ ) <sup>†</sup>	0.481 $\pm$ 0.003	0.274 $\pm$ 0.012	0.277 $\pm$ 0.003	0.121 $\pm$ 0.004	<b>0.013 <math>\pm</math> 0.002</b>	<b>0.124 <math>\pm</math> 0.008</b>	0.013 $\pm$ 0.003	0.047 $\pm$ 0.001	<b>0.006 <math>\pm</math> 0.000</b>
Ours, extended (12-param)	0.085 $\pm$ 0.001	0.056 $\pm$ 0.002	0.071 $\pm$ 0.001	0.035 $\pm$ 0.000	0.013 $\pm$ 0.003	0.131 $\pm$ 0.005	0.013 $\pm$ 0.004	0.035 $\pm$ 0.001	0.005 $\pm$ 0.000
<i>Training MBE (log space)</i>									
Chinchilla [26]	-0.063 $\pm$ 0.002	-0.017 $\pm$ 0.017	-0.059 $\pm$ 0.015	-0.017 $\pm$ 0.010	-0.001 $\pm$ 0.001	-0.069 $\pm$ 0.008	-0.001 $\pm$ 0.005	0.003 $\pm$ 0.005	<b>0.000 <math>\pm</math> 0.001</b>
Muennighoff [36]	-0.047 $\pm$ 0.001	-0.023 $\pm$ 0.022	<b>-0.003 <math>\pm</math> 0.008</b>	<b>-0.002 <math>\pm</math> 0.007</b>	-0.001 $\pm$ 0.001	-0.046 $\pm$ 0.006	-0.001 $\pm$ 0.005	0.003 $\pm$ 0.005	<b>-0.000 <math>\pm</math> 0.000</b>
M4 ( <i>N</i> -axis) [1]	0.137 $\pm$ 0.025	-0.050 $\pm$ 0.080	-0.084 $\pm$ 0.082	-0.022 $\pm$ 0.042	-0.019 $\pm$ 0.004	-0.085 $\pm$ 0.015	-0.020 $\pm$ 0.015	-0.089 $\pm$ 0.036	-0.007 $\pm$ 0.003
M4 ( <i>D</i> -axis) [1]	-0.056 $\pm$ 0.002	-0.022 $\pm$ 0.016	-0.061 $\pm$ 0.013	-0.034 $\pm$ 0.015	-0.010 $\pm$ 0.005	-0.073 $\pm$ 0.012	-0.012 $\pm$ 0.017	-0.015 $\pm$ 0.008	-0.005 $\pm$ 0.004
BNSL <i>k</i> =1 [12]	-0.055 $\pm$ 0.000	-0.023 $\pm$ 0.000	-0.059 $\pm$ 0.012	-0.029 $\pm$ 0.000	-0.009 $\pm$ 0.285	-0.072 $\pm$ 0.012	-0.011 $\pm$ 0.017	-0.003 $\pm$ 0.008	-0.005 $\pm$ 0.004
BNSL <i>k</i> =2 [12]	-0.055 $\pm$ 0.000	-0.024 $\pm$ 0.000	-0.062 $\pm$ 0.000	-0.030 $\pm$ 0.000	-0.011 $\pm$ 0.004	-0.072 $\pm$ 0.012	-0.011 $\pm$ 0.017	-0.003 $\pm$ 0.217	-0.005 $\pm$ 0.004
Farseer [29]	0.137 $\pm$ 0.012	-0.048 $\pm$ 0.000	-0.112 $\pm$ 0.046	-0.092 $\pm$ 0.023	-0.001 $\pm$ 0.001	-0.067 $\pm$ 0.006	-0.002 $\pm$ 0.004	<b>0.001 <math>\pm</math> 0.004</b>	<b>-0.000 <math>\pm</math> 0.001</b>
<b>Ours (Eq. (2))</b>	-0.027 $\pm$ 0.002	<b>-0.001 <math>\pm</math> 0.008</b>	-0.012 $\pm$ 0.008	-0.010 $\pm$ 0.005	<b>-0.000 <math>\pm</math> 0.001</b>	-0.015 $\pm$ 0.015	<b>0.000 <math>\pm</math> 0.004</b>	-0.006 $\pm$ 0.000	<b>0.000 <math>\pm</math> 0.000</b>
Ours, no wrapper	<b>-0.012 <math>\pm</math> 0.002</b>	-0.032 $\pm$ 0.023	-0.017 $\pm$ 0.007	-0.006 $\pm$ 0.005	-0.001 $\pm$ 0.002	-0.025 $\pm$ 0.019	<b>-0.000 <math>\pm</math> 0.006</b>	0.003 $\pm$ 0.005	<b>-0.000 <math>\pm</math> 0.000</b>
Ours, no overfitting term	0.155 $\pm$ 0.013	-0.054 $\pm$ 0.077	-0.086 $\pm$ 0.043	-0.033 $\pm$ 0.021	-0.001 $\pm$ 0.001	-0.072 $\pm$ 0.008	-0.001 $\pm$ 0.004	-0.006 $\pm$ 0.004	<b>0.000 <math>\pm</math> 0.000</b>
Ours, $1-e^{-h}$ wrapper	-0.019 $\pm$ 0.001	<b>0.001 <math>\pm</math> 0.010</b>	-0.015 $\pm$ 0.007	-0.008 $\pm$ 0.005	-0.001 $\pm$ 0.001	-0.017 $\pm$ 0.018	<b>0.000 <math>\pm</math> 0.004</b>	-0.003 $\pm$ 0.004	<b>-0.000 <math>\pm</math> 0.000</b>
Ours, single-exp ( $N/D$ ) <sup>†</sup>	0.059 $\pm$ 0.009	-0.082 $\pm$ 0.054	<b>0.003 <math>\pm</math> 0.019</b>	<b>0.001 <math>\pm</math> 0.014</b>	<b>-0.000 <math>\pm</math> 0.001</b>	<b>-0.014 <math>\pm</math> 0.015</b>	<b>-0.000 <math>\pm</math> 0.003</b>	-0.006 $\pm$ 0.004	<b>-0.000 <math>\pm</math> 0.000</b>
Ours, extended (12-param)	-0.010 $\pm$ 0.001	0.002 $\pm$ 0.007	0.003 $\pm$ 0.004	0.001 $\pm$ 0.002	-0.000 $\pm$ 0.001	-0.003 $\pm$ 0.008	-0.000 $\pm$ 0.003	-0.001 $\pm$ 0.002	0.000 $\pm$ 0.000

## P An auto-discovered 12-parameter form

The ‘‘Ours, extended (12-param)’’ row in the per-protocol tables of Appendix O is reported in gray and excluded from the per-column rankings because it was not derived from a structural argument like the headline form (Equation (2)), but discovered by automated form search. We describe its provenance, write out the form, summarize its empirical performance across all nine datasets, and offer post-hoc intuition for why it works.

**Provenance: automated form search.** In an attempt to identify a parametric form with strictly better in-sample fit than the 8-parameter headline form on our densest grid, we tasked an autonomous Claude Code agent [2] running Claude Opus-4.7 [3] with iteratively proposing and evaluating modifications. Each round of the loop: (i) the agent inspected per-cell residual diagnostics from the current leader; (ii) it proposed a small set of structural modifications (cell-coupled exponents, additional cross terms, alternative wrappers); (iii) each candidate was fit in parallel under the same multi-start BFGS protocol used elsewhere in this paper, with metrics recorded against the MNIST grid; (iv) the leaderboard was updated and a new round began. Fourteen rounds and dozens of candidate forms produced a winner on held-out RMSE, a 12-parameter form we refer to as the *extended* form. We treat this as a form of automated form search: the agent autonomously proposes, fits, and selects parametric structures based on residual evidence and an explicit objective. A similar LLM-driven scaling-law discovery paradigm was proposed concurrently by Lin et al. [33], who introduce SLDAgent, an evolution-based agent that co-optimizes scaling-law form and parameters across thousands of experiments alongside a benchmark for the task; we view our 14-round single-grid loop as a much narrower instance of the same idea, used here only as an empirical upper bound on what closed-form structures can fit our densest grid.

**Functional form.** Let  $\beta_{\text{eff}}(N, D) = \beta_0 + \beta_N \ln N + \beta_D \ln D$  (clamped to  $[0.01, 5]$ ). The extended form is

$$h(N, D, T) = \frac{a}{N^\alpha} + \frac{b}{T^{\beta_{\text{eff}}(N, D)}} + \frac{cN^\gamma}{D^\delta} + e \left( \frac{N}{D} \right)^\phi, \quad L = E + (L_0 - E)(1 - e^{-h}). \quad (16)$$

The twelve free parameters are  $(E, a, \alpha, b, \beta_0, c, \gamma, \delta, e, \phi, \beta_N, \beta_D)$ . Three changes relative to the headline form: the undertraining exponent  $\beta$  becomes log-linear in  $N$  and  $D$  (adding  $\beta_N, \beta_D$ ); a second overfitting-style cross term  $e(N/D)^\phi$  is added (adding  $e, \phi$ ); and the saturating wrapper is the exponential variant  $1 - e^{-h}$  rather than the rational  $h/(1 + h)$  (no additional parameter; cf. Appendix D).

**Empirical performance.** Across all nine datasets and all four protocols of Appendix O, the extended form’s held-out RMSE is the lowest (or tied lowest) on nearly every column, beating both the headline form and every external baseline. The improvement margin is largest on the data-constrained MNIST and TinyStories cells where the headline form’s largest residuals concentrate, and smallest on the LLM grids where every form already fits well. We exclude the extended form from the per-column rankings to keep the comparison fair: it carries 4 extra parameters relative to the headline form and was discovered by an agent optimizing against the very fit metric we are now evaluating, so it has an oracle-like advantage that the structural baselines lack.

**Intuition for the extra terms.** We can offer post-hoc readings, not derivations. The cell-coupled  $\beta_{\text{eff}}(N, D)$  relaxes the assumption that one global undertraining exponent fits all  $(N, D)$  regimes; in practice, larger models trained on more data appear to descend the loss curve at a different effective rate than smaller models trained on less, and a global  $\beta$  is a compromise between the two regimes. The extra  $e(N/D)^\phi$  term is a second knob in the memorization regime; with the original  $cN^\gamma/D^\delta$  term covering one  $(N, D)$  shape, the additional term lets the form represent a soft transition between two memorization regimes (e.g., undermemorization at small  $N/D$  and saturated memorization at large  $N/D$ ) rather than a single power-law shape. Both readings are speculative; the form was selected by predictive performance alone.

**Caveats and why the headline form remains 8-parameter.** The extended form has no theoretical grounding:  $\beta_{\text{eff}}(N, D)$  is not derived from a learning-rate schedule or capacity argument, and the  $e(N/D)^\phi$  term does not correspond to a separable underperformance mechanism. Its parameter

identifiability is also weak:  $(\beta_0, \beta_N, \beta_D)$  are jointly poorly constrained, and several parameters show  $> 50\%$  multistart disagreement on individual datasets, so bootstrap intervals on derived quantities (e.g.,  $N^*$ ) would be wide. We retain the 8-parameter headline form as the paper’s recommended form because (i) every term has a structural justification (Section 2), (ii) the parameter-identification table (Appendix F) gives a clear empirical regime for each parameter, and (iii) the cost-allocation analysis (Appendix K) admits closed-form stationarity conditions that the extended form does not. The extended form is included as an empirical upper bound: it bounds the predictive performance achievable by a parametric form on this data, providing context for the question of whether the headline form’s parsimony costs material accuracy. The empirical answer is that it does, modestly, but not by enough to displace structural justifiability as the headline criterion.

## Q Plots

### Q.1 Training trajectories

The figures below show the empirical running-min validation-loss trajectories across  $(N, D, C)$  cells for each of our four training experiments, decomposed into per- $D$  and per- $N$  slices. Figure 2 in the main paper showed a six-cell selection of the MNIST surface; Figure 5 below shows all cells. For CIFAR-100, Darcy, and TinyStories, which use the Warmup-Stable-Decay schedule of §3.1, each cell decomposes into three components: solid lines are the running-min along the stable run, dashed branches are cooldown forks departing from the stable run at log-spaced compute targets, and points mark the final running-min loss at the end of each fork. MNIST uses no LR schedule, so each cell shows a single solid trajectory.

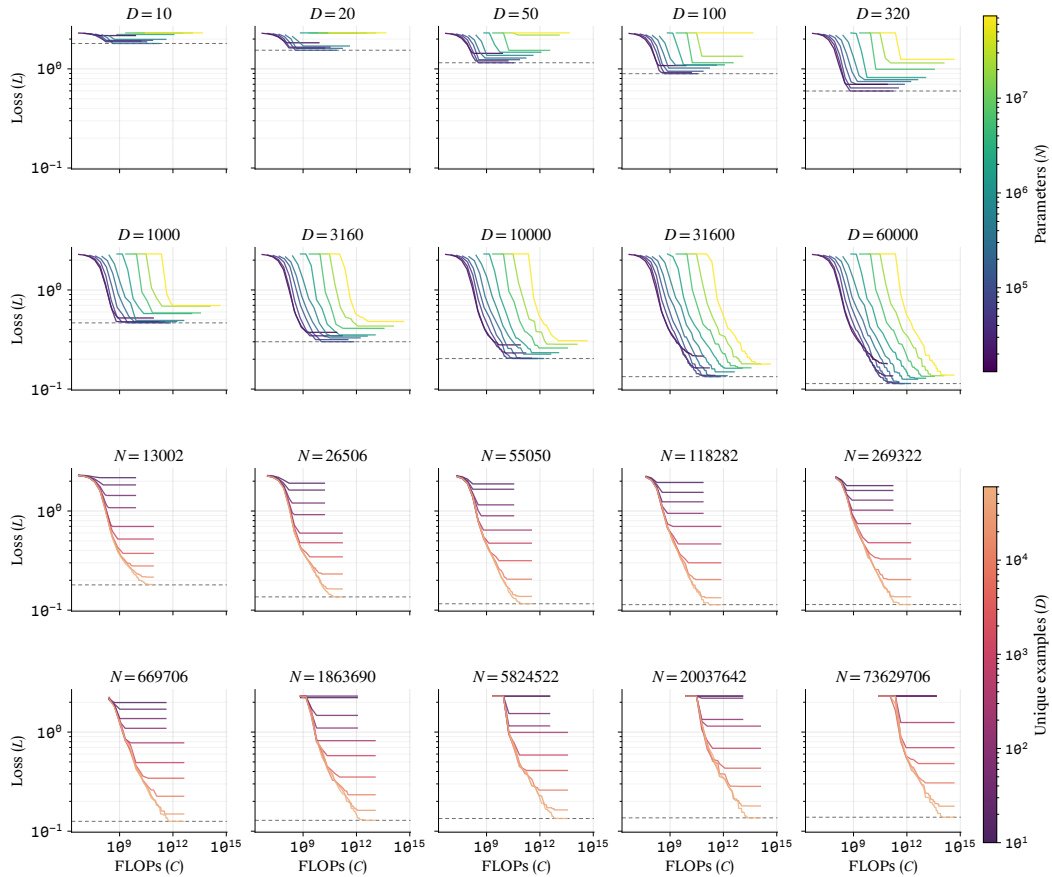


Figure 5: MNIST empirical running-min validation-loss surface across all  $(N, D)$  cells. *Top*: loss vs FLOPs at fixed  $D$ , colored by  $N$ . *Bottom*: same surface at fixed  $N$ , colored by  $D$ .

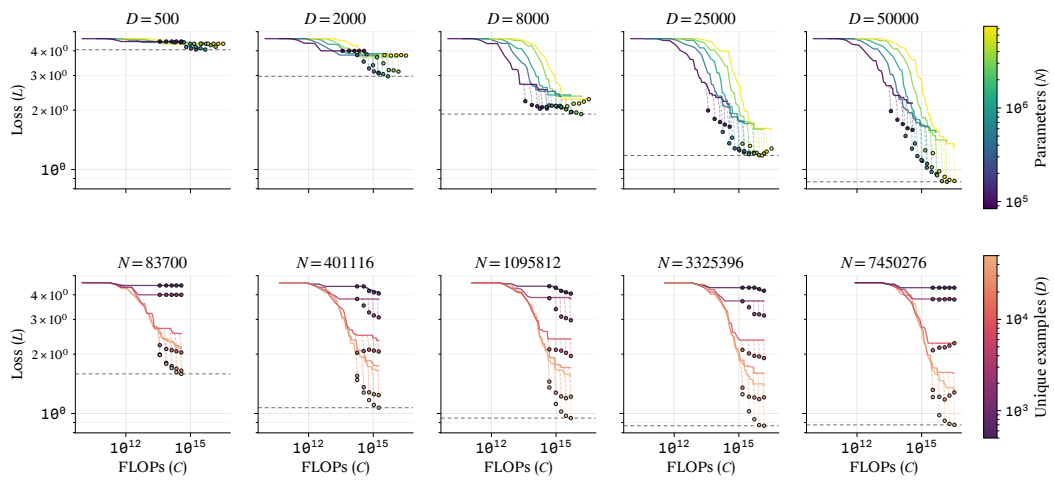


Figure 6: CIFAR-100 empirical running-min validation-loss surface. *Top*: loss vs FLOPs at fixed  $D$ , colored by  $N$ . *Bottom*: same surface at fixed  $N$ , colored by  $D$ .

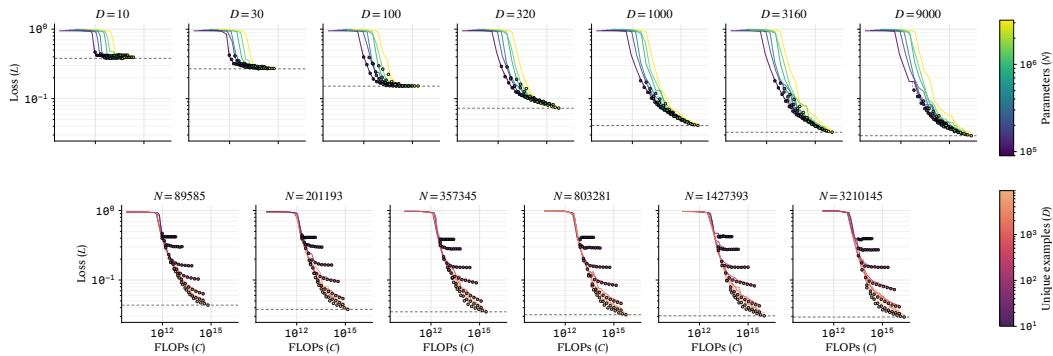


Figure 7: Darcy empirical running-min validation-loss surface. *Top*: loss vs FLOPs at fixed  $D$ , colored by  $N$ . *Bottom*: same surface at fixed  $N$ , colored by  $D$ .

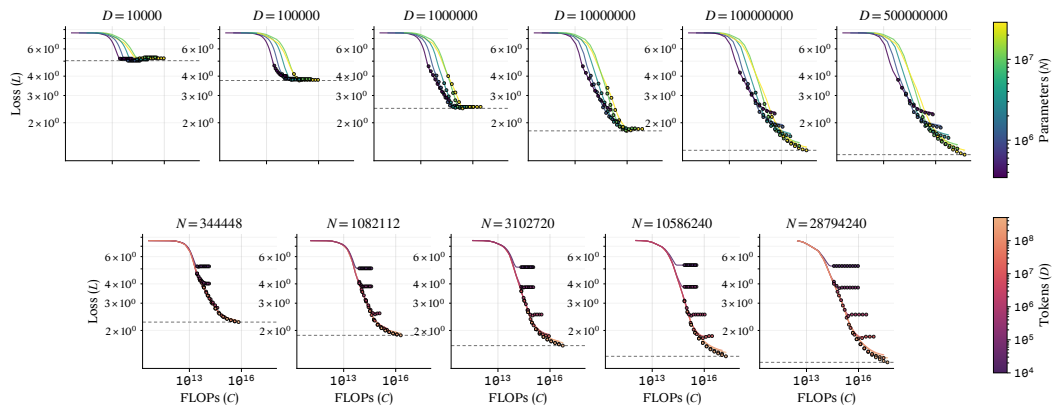


Figure 8: TinyStories empirical running-min validation-loss surface. *Top*: loss vs FLOPs at fixed  $D$ , colored by  $N$ . *Bottom*: same surface at fixed  $N$ , colored by  $D$ .

## Q.2 Held-out predictions across datasets

Figure 3 in the main paper showed observed-versus-predicted holdout scatter on two representative datasets (Chinchilla and MNIST) under the high- $C$  holdout. The figures below show the full grid: each of our four training experiments (internal) and each of the five published LLM grids (external), under both the high- $C$  and high- $D$  holdouts of §3.1. Rows are datasets, columns are forms; blue points are training cells, orange points are held-out cells, and a perfectly-calibrated form would place all points on the  $y = x$  diagonal.

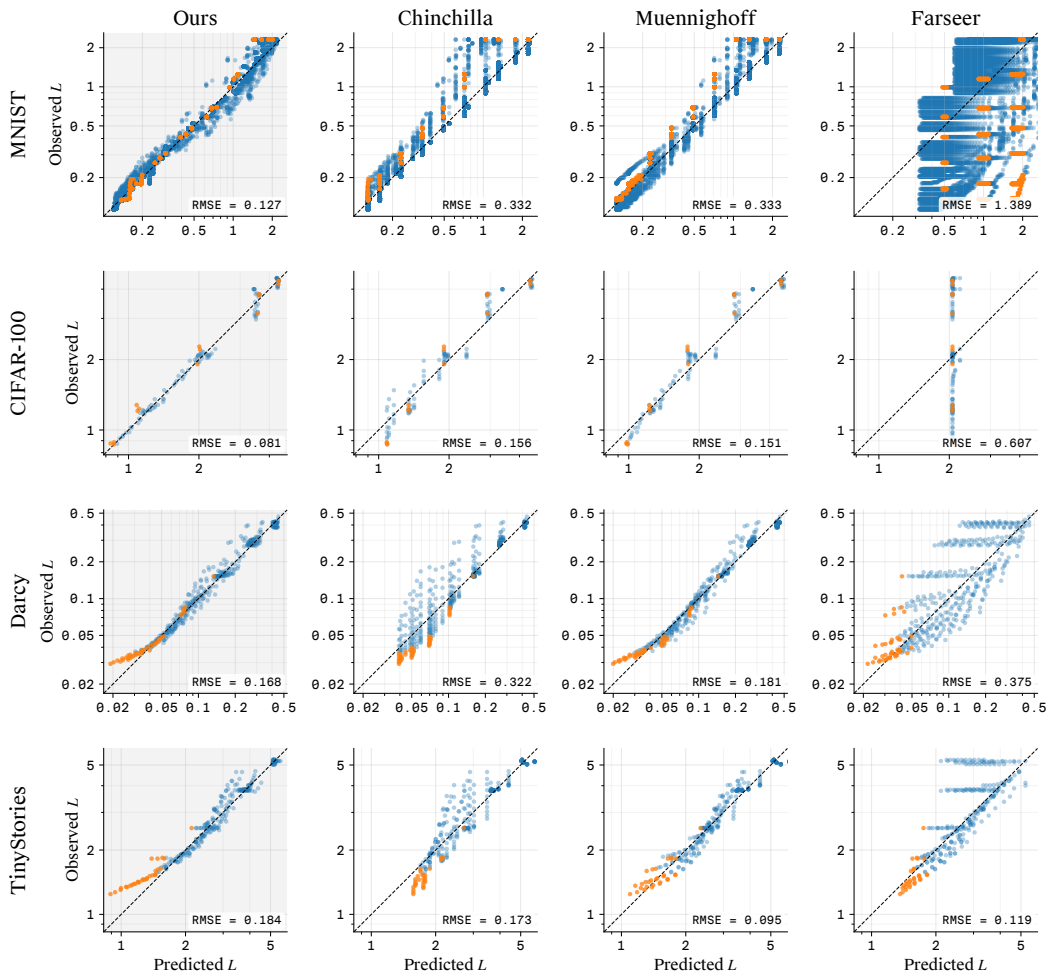


Figure 9: **High- $C$** . Observed vs. predicted loss on the four training experiments (MNIST, CIFAR-100, Darcy, TinyStories) under the high- $C$  holdout.

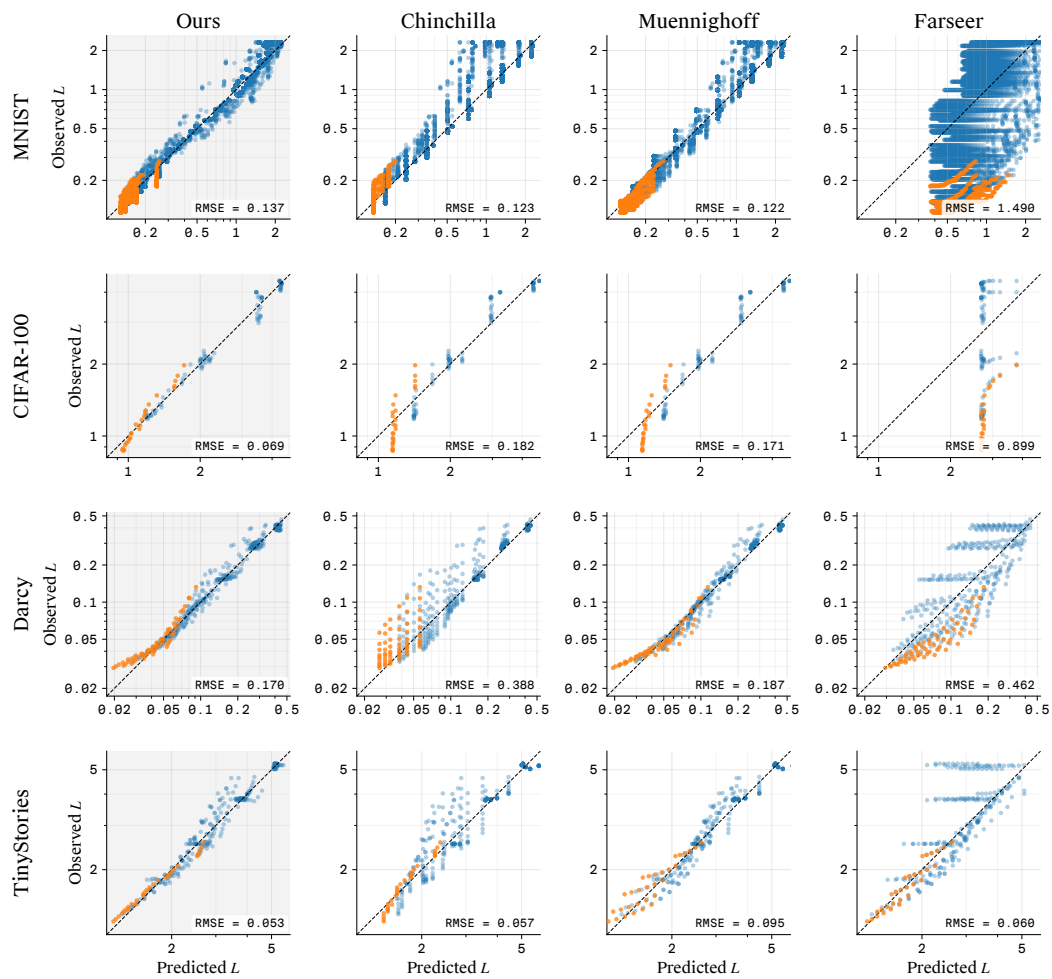


Figure 10: **High- $D$** . Observed vs. predicted loss on the four training experiments under the high- $D$  holdout.

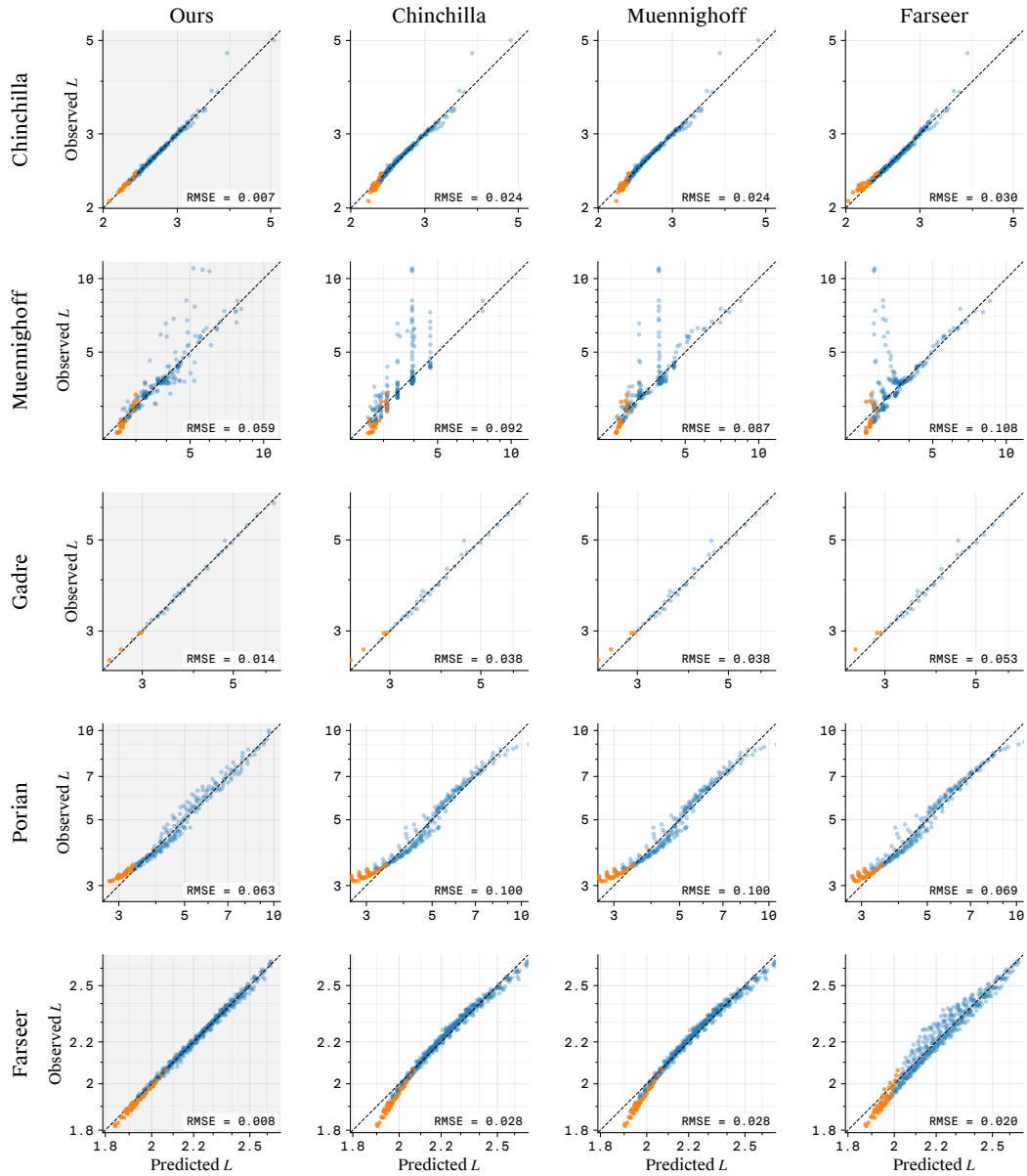


Figure 11: **High-C**. Observed vs. predicted loss on the five published LLM grids (Chinchilla, Muennighoff, Gadre, Porian, Farseer) under the high-C holdout.

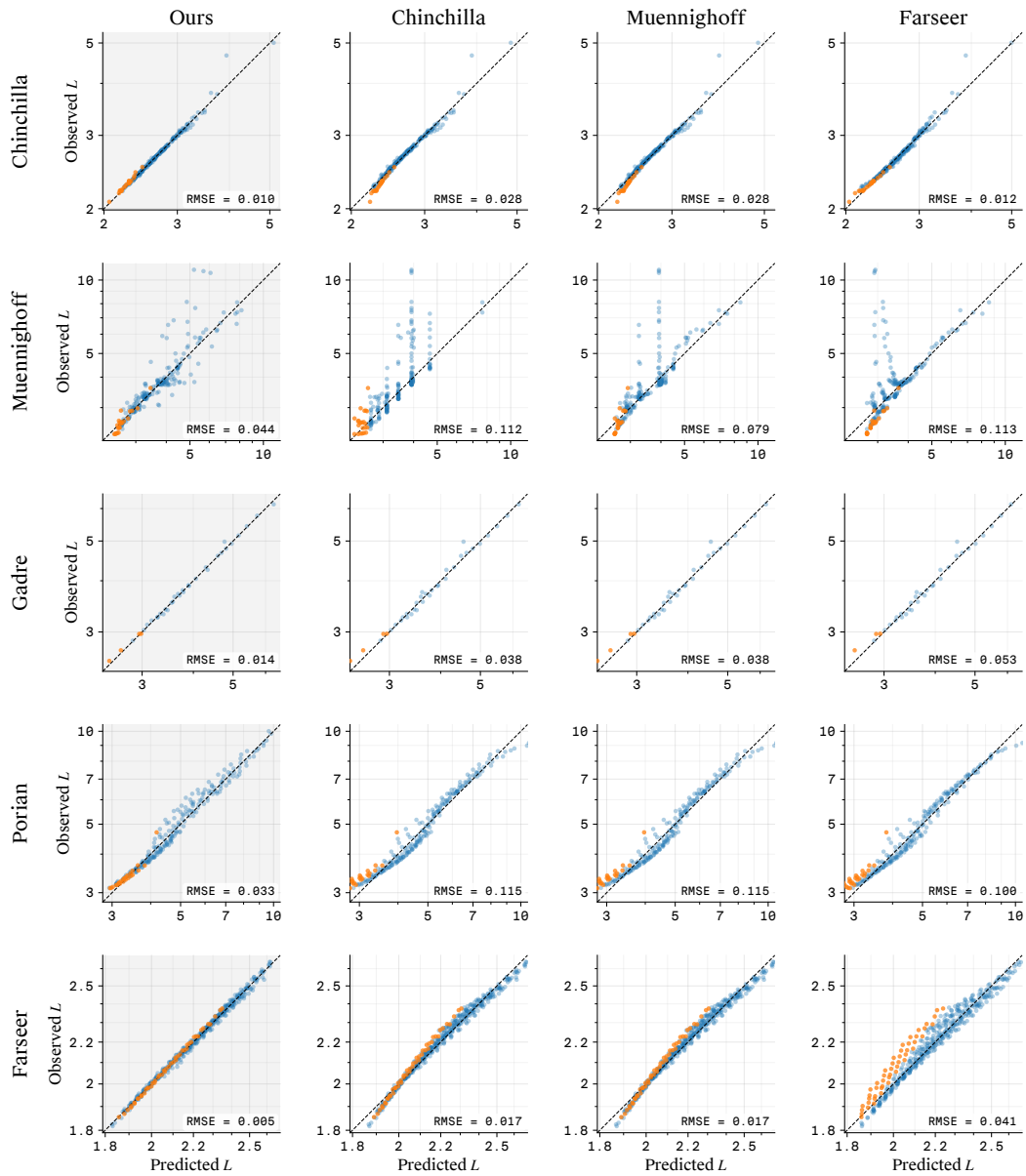


Figure 12: **High- $D$** . Observed vs. predicted loss on the five published LLM grids under the high- $D$  holdout.